Characterization of Amorphous Materials using the Three Particle Structure Factor

Semir Vrana

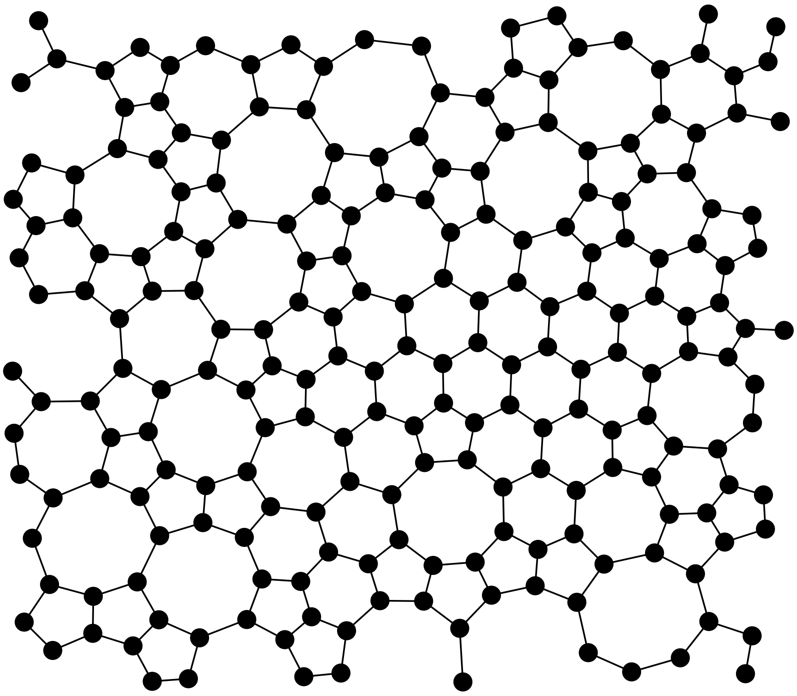

2020

Physikalisches Institut

Characterization of Amorphous Materials using the Three Particle Structure Factor

Inaugural-Dissertation
zur Erlangung des Doktorgrades
der Naturwissenschaften im Fachbereich Physik
der Mathematisch-Naturwissenschaftlichen Fakultät
der Westfälischen Wilhelms-Universität Münster

vorgelegt von
Semir Vrana
aus *Foča / Bosnien und Herzegowina*
-2020-

Dekan:	Prof. Dr. Gerhard Wilde
Erster Gutachter:	Prof. Dr. Helmut Kohl
Zweiter Gutachter:	Prof. Dr. Gerhard Wilde
Tag der mündlichen Prüfung:	19.02.2021
Tag der Promotion:	19.02.2021

Abstract

Amorphous substances are increasingly gaining importance in various industries. However, apart from scattering experiments, there are still few quantitative methods available to obtain information about the structure, apart from particle spacing. In this thesis, the three particle structure factor is determined from transmission electron microscopy images to obtain information about the bond angle distribution in amorphous solids. Furthermore, the influence of different structural models on the three particle structure factor was investigated by means of various simulations and the limits of the method were determined.

Kurzzusammenfassung

Amorphe Stoffe erfahren eine wachsende Bedeutung in verschiedenen Industriezweigen. Abgesehen von Streuexperimenten existieren nur wenige quantitative Methoden, um Aufschluss über die Struktur, insbesondere über die Teilchenabstände hinaus, zu bekommen. In dieser Arbeit wird der Dreiteilchenstrukturfaktor aus Transmissionelektronenmikroskopie-Aufnahmen ermittelt, um Informationen über die Bindungswinkel in amorphen Festkörpern zu erhalten. Weiter wurde mittels verschiedener Simulationen der Einfluss einiger Strukturmodelle auf den Dreiteilchenstrukturfaktor untersucht und die Grenzen der Methode ermittelt.

Contents

Chapter 1

Introduction

The characterization of the properties of materials is one of the major interests in the material sciences. The usual approach is to use diffraction where an incoming beam of particles like photons, electron or neutrons are scattered off a specimen and then detected by a spatially resolving detector. Two common diffraction patterns (DPs) are shown in figure 1.1. The diffraction pattern on the right hand side stems from a crystalline specimen where the atoms or molecules are distributed in a periodic way. The diffraction patterns for crystalline solids consist of well-defined spots. From the positions of the spots one can already conclude that this specimen has a 6-fold symmetry. It is also possible to determine the atom spacings inside the specimen. Due to the periodicity of crystals every particle position inside the crystal can be described by an equation of the form

$$\vec{r} = \vec{r}_0 + n_1 \cdot \vec{a}_1 + n_2 \cdot \vec{a}_2 + n_3 \cdot \vec{a}_3, \tag{1.1}$$

where $\vec{r}_0$ is the starting point, $\vec{a}_1$, $\vec{a}_2$ and $\vec{a}_3$ are lattice basis vectors and n_1, n_2 and n_3 are some arbitrary integers [Zim79].
On the left side of figure 1.1 an amorphous specimen is shown. Amorphous specimens do not have the long range order that crystals have. In this DP, instead of spots there are smeared out rings since there are no long-range structures. However, due to electromagnetic forces, neighbouring particles cannot come arbitrary close. This leads to some *short-range order* (*SRO*). In particular, the next neighbour distance are distributed around this minimal distance.
Amorphous solids cannot be described by an equation like (1.1). Probably the most simple model of an amorphous solid is that of an assembly of hard spheres, i.e. impenetrable spherical atoms [Zim79]. An example is shown in figure 1.2. Such a *Random Close Packing* (RCP) cannot be described by a small set of lattice vectors. For a complete description of such a system one would need all particle positions, which is infeasible. Amorphous solids

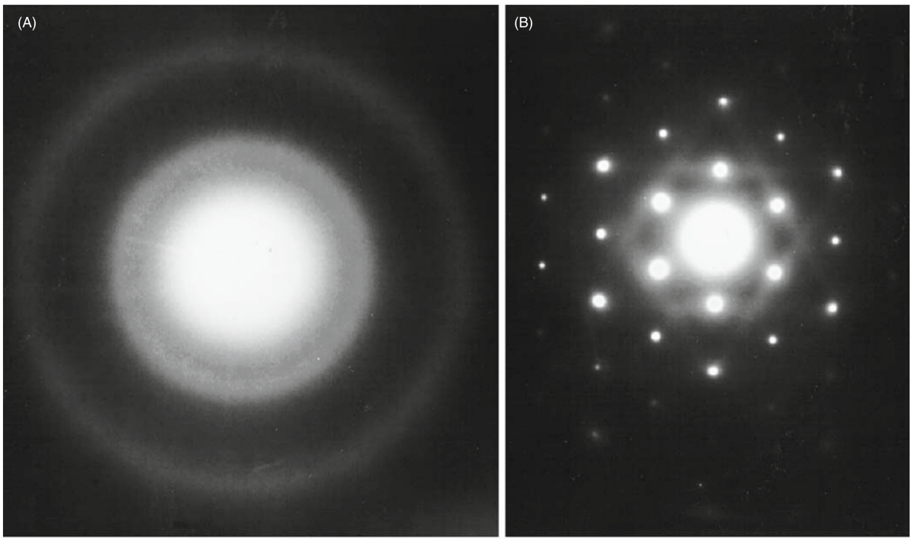

Figure 1.1: Two diffraction patterns obtained with a conventional TEM. On the left, the pattern for amorphous carbon is shown while the right specimen is an Al single crystal. The image was taken from [WC09].

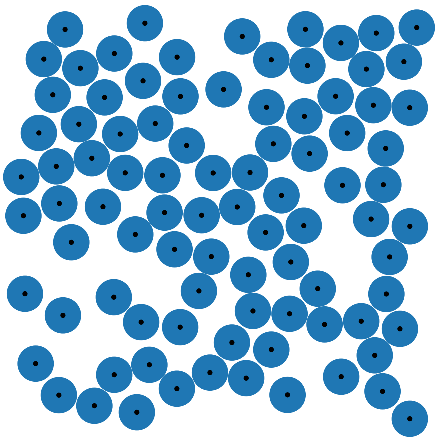

Figure 1.2: Example of a Random Close Packing (RCP). The Black dots represent the atoms while the blue circles represent their impenetrable atom potentials.

are instead described by distribution functions.

A special kind of amorphous solids are glasses, which are amorphous solids that were produced by rapidly cooling a melt below its glass temperature [Gup96]. The transition has to be fast enough that the preferred phase transition toward the crystalline state is avoided [BB11]. In [Zac32] it was proposed to model silica glass as a random network with well defined bonding rules [Zim79]. Each silicon atom is surrounded by four oxygen atoms and each oxygen atom connects two silicon atoms. Since the structure of amorphous silica resembles that of crystalline SiO_2 one may expect that some of the structural properties are preserved.

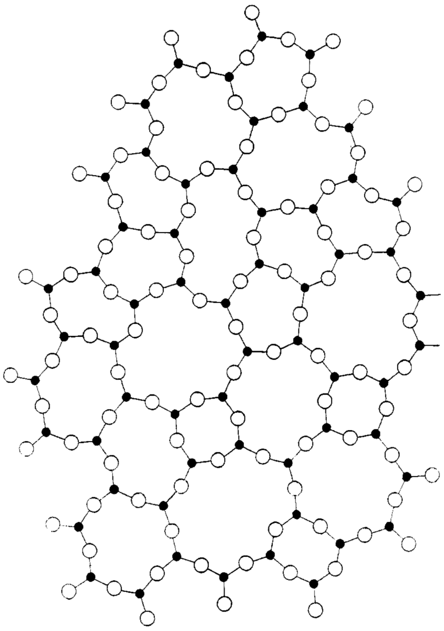

Figure 1.3: Zachariasens model for silica glass. Taken from [Zac32].

Apart from the well established uses of glasses as glass containers, windows, lenses or optical fibers new applications have emerged in the last years [Var13]. Glasses play a key role in solar energy generators by improving the solar energy conversion efficiency and new glassy materials are being developed for efficient energy storage such as glass-based solid-state batteries that improve storage density, reduce the charging time and increase the number of recharging cycles [Var13].

Electron microscopy takes an important role in the investigation of any kind of material and also in that of amorphous solids. Since its development in the early thirties of the last century [WC09], electron microscopy gained increasing relevance while also improving its resolution. Figure 1.4 shows an image of an amorphous silica monolayer that was placed on top of a graphene substrate. One can clearly see the silicon atoms that form patterns similar to those predicted by Zachariasen.

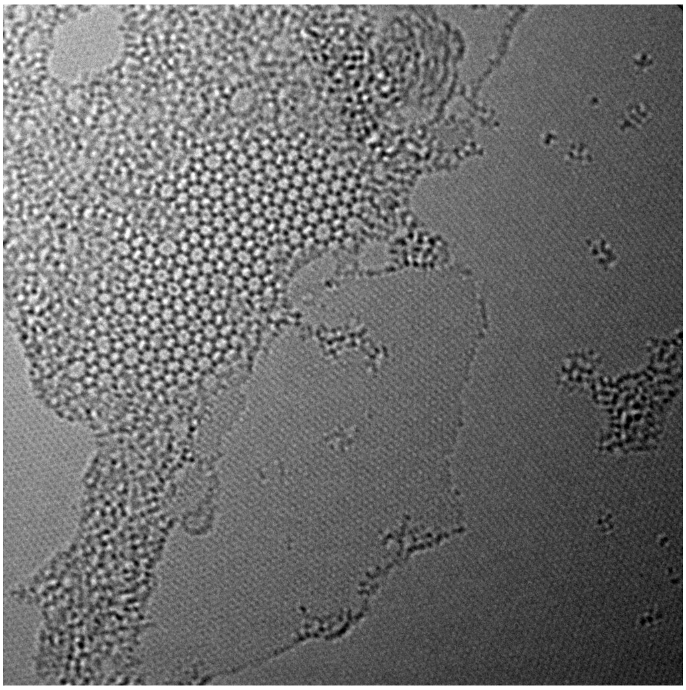

Figure 1.4: Image of amorphous silica on top of a graphene substrate. Taken from [Hua+12].

Diffraction experiments only provide information about the pair distribution in the specimen. While it is possible to obtain some structural information this way, a more detailed description of the structure can only be achieved by obtaining higher order correlation functions.

Previous attempts at determining the three particle structure factor from transmission electron microscope images have failed [Ham88; Hak95], so the following questions arise. Firstly, is it possible to obtain the three particle structure factor from TEM images of amorphous specimens. If so, what are the required conditions? And secondly, what information can be obtained about the underlying structure of an amorphous solid from the three particle structure factor.

Section 2 motivates the introduction of a structure factor to describe structure by discussing diffraction off periodic lattices. Afterwards, higher order structure factors are discussed in depth and the relationship to distribution functions is shown. In section 3 the basics of transmission electron microscopy are introduced and the fundamental relation between the image contrast and the structure factor is derived. In the following section different structural models for amorphous solids are introduced and their implementation as computer programs is explained. Section 5 collects numerical and experimental results obtained in this thesis and discusses them. The last section gives a short summary and possible future directions.

Chapter 2

Solid State Theory Basics

Amorphous solids are not entirely random. Instead they have some kind of defective order that deviates from a completely ordered system [Zim79]. This chapter starts by describing ordered crystals before discussing the description of amorphous systems. It will also introduce the structure factor as a connecting factor from lattice structures to diffraction probabilities.

2.1 Crystalline Solids

A crystal is a set of (in principle) infinitely many identical atoms or molecules for which every lattice site can be reached with a discrete shift by an integral linear combination of some base vectors

$$\vec{r} = \vec{r_0} + \sum_{i=1}^{3} n_i \vec{a}_i$$

where $(\vec{a}_i)_{i\in\{1,2,3\}}$ is a set of 3 linearly independent base vectors and $(n_i)_{i\in\{1,2,3\}} \in \mathbb{Z}$ are some arbitrary integers. Hence the system is invariant under discrete translations by multiples of the basis vectors.

2.1.1 The reciprocal lattice and diffraction

Most of the relevant physical quantities are invariant under translations by a lattice vector $\vec{R}$ [Czy13]

$$f(\vec{r}) = f(\vec{r} + \vec{R}). \tag{2.1}$$

Therefore such quantities can be expressed by a Fourier series

$$f(\vec{r}) = \sum_{\vec{G}} f_{\vec{G}} \mathrm{e}^{-2\pi \mathrm{i} \vec{G}\cdot\vec{r}}$$

with Fourier coefficients

$$f_{\vec{G}} = \frac{1}{V_{\text{UC}}} \int_{\text{UC}} \mathrm{d}^3 r\, f(\vec{r}) \mathrm{e}^{2\pi \mathrm{i} \vec{G}\cdot\vec{r}}$$

where V_{UC} is the volume of one unit cell. By combining the condition (2.1) with the definition of the Fourier transform it follows that

$$f(\vec{r}+\vec{R}) = \sum_{\vec{G}} f_{\vec{G}} \mathrm{e}^{-2\pi \mathrm{i} \vec{G}\cdot(\vec{r}+\vec{R})} = \sum_{\vec{G}} f_{\vec{G}} \mathrm{e}^{-2\pi \mathrm{i} \vec{G}\cdot\vec{r}} \mathrm{e}^{-2\pi \mathrm{i} \vec{G}\cdot\vec{R}} \overset{!}{=} f(\vec{r}), \tag{2.2}$$

$$\Rightarrow \mathrm{e}^{-2\pi \mathrm{i} \vec{G}\cdot\vec{R}} = 1, \tag{2.3}$$

$$\Rightarrow \vec{G}\cdot\vec{R} = n, \tag{2.4}$$

where n is some arbitrary integer. The vector $\vec{G}$ can be expanded as

$$\vec{G} = \sum_{i=1}^{3} k_i \vec{b}_i$$

with $(k_i)_{i\in\{1,2,3\}} \in \mathbb{Z}$. In order to obey the condition (2.4), the basis vectors $\vec{b}_i$ must fulfil the orthogonality relation

$$\vec{a}_i \cdot \vec{b}_j = \delta_{ij}.$$

The vectors $\vec{b}_i$ form the *reciprocal* lattice [Czy13].

2.1.2 Diffraction Condition

When an incoming particle, described as a plane wave $|\vec{k}\rangle = \mathrm{e}^{\mathrm{i}k\cdot\vec{r}}$, interacts with a crystal it is diffracted from the periodic potential $V(\vec{r}) = V(\vec{r}+\vec{R})$ of the crystal and is altered into a state $|\vec{k'}\rangle$. The transition amplitude is proportional to the matrix element [Czy13]

$$\langle\vec{k}|V(\vec{r})|\vec{k'}\rangle = \frac{1}{V}\int \mathrm{d}^3 r \mathrm{e}^{2\pi \mathrm{i}\vec{k'}\cdot\vec{r}} V(\vec{r}) \mathrm{e}^{-2\pi \mathrm{i}\vec{k}\cdot\vec{r}} = \frac{1}{V}\int \mathrm{d}^3 r \sum_{\vec{G}} V_{\vec{G}} \mathrm{e}^{-2\pi \mathrm{i}(\vec{k}+\vec{G}-\vec{k'})\cdot\vec{r}} = \sum_{\vec{G}} V_{\vec{G}} \delta_{\vec{k'}-\vec{k},\vec{G}}.$$

This is only non-zero if $\vec{k'} = \vec{k} + \vec{G}$ or equivalently $\Delta\vec{k} = \vec{G}$. For elastic scattering with $k^2 = k'^2$ this leads to the condition

$$2\vec{k}\cdot\vec{G} + G^2 = 0.$$

2.1.3 Structure factor and atomic form factor

When the diffraction condition is satisfied the matrix element can be written as [AM11]

$$
\begin{aligned}
\langle\vec{k}|V(\vec{r})|\vec{k}'\rangle &= \int \mathrm{d}^3\, V(\vec{r})\mathrm{e}^{-2\pi\mathrm{i}\vec{G}\cdot\vec{r}}, && (2.5)\\
&= \sum_j \int \mathrm{d}^3 r\, V_j(\vec{r}-\vec{r}_j)\mathrm{e}^{-2\pi\mathrm{i}\vec{G}\cdot\vec{r}}, && (2.6)\\
&= \sum_j \mathrm{e}^{-2\pi\mathrm{i}\vec{G}\cdot\vec{r}_j} \int \mathrm{d}^3 r\, V_j(\vec{\rho})\mathrm{e}^{-2\pi\mathrm{i}\vec{G}\cdot\vec{\rho}}, && (2.7)\\
&= \sum_j f_j \mathrm{e}^{-2\pi\mathrm{i}\vec{G}\cdot\vec{r}_j}, && (2.8)\\
&= \sum_{n,l} f_l \mathrm{e}^{-2\pi\mathrm{i}\vec{G}\cdot(\vec{R}_n+\vec{x}_l)}, && (2.9)\\
&= \sum_n \mathrm{e}^{-2\pi\mathrm{i}\vec{G}\cdot\vec{R}_n} \sum_l f_l \mathrm{e}^{-2\pi\mathrm{i}\vec{G}\cdot\vec{x}_l}. && (2.10)
\end{aligned}
$$

This is the *structure factor*[1] [Kit05]. In (2.6), the lattice potential V was split into atomic potentials V_j. In (2.8), the atomic form factor f_j were introduced as the Fourier transform of the atomic potentials. Following that, the atom position $\vec{r}_j$ was split into the position of the lattice site $\vec{R}_n$ and the position of the atom relative to the lattice site $\vec{x}_l$. In the last line (2.10), the sum was split into one sum over the lattice and one over the primitive cell. For lattices with one-atomic basis this simplifies to

$$
S(\vec{G}) = \sum_n \mathrm{e}^{-2\pi\mathrm{i}\vec{G}\cdot\vec{R}_n}. \tag{2.11}
$$

In the following only this case will be considered.

2.2 Higher Order Structure Factors

For an ideal crystal one can write the scattering amplitudes as a product of the structure factor and the atomic form factor [AM11, p. 14]. In the following this will be generalized for amorphous matter and multi-particle structure factors will be discussed.

2.2.1 Two Particle Structure Factor

From the definition of the structure factor (eq. (2.11)) one can find that the following properties hold,

$$
S(-\vec{q}) = S^*(\vec{q}), \tag{2.12a}
$$

---

[1] This is sometimes also denoted as the static structure factor.

$$S(\vec{0}) = N. \tag{2.12b}$$

The asterisk denotes complex conjugation.
The *two particle structure factor* then is defined as [Ham88]

$$S^{(2)}(\vec{q}) = \frac{1}{N} S(\vec{q}) S(-\vec{q}) = \frac{1}{N} |S(\vec{q})|^2 = \frac{1}{N} \sum_{j,k=1}^{N} \mathrm{e}^{-2\pi \mathrm{i} \vec{q}\cdot(\vec{R}_j - \vec{R}_k)}. \tag{2.13}$$

It has the properties

$$S^{(2)}(\vec{q}) \geq 0, \tag{2.14a}$$

$$S^{(2)}(-\vec{q}) = S^{(2)}(\vec{q}), \tag{2.14b}$$

$$S^{(2)}(\vec{0}) = N. \tag{2.14c}$$

This implies that $S^{(2)}$ only has real values. The two particle structure factor can be interpreted as the Fourier transformation of an autocorrelation. Let $s(\vec{r})$ be the Fourier transform of $S(\vec{q})$, then autocorrelation is defined as

$$s_2(\vec{r}) = \int s(\vec{\xi}) s(\vec{r} + \vec{\xi}) \, \mathrm{d}^3\xi. \tag{2.15}$$

Its Fourier transform can then be rewritten as

$$\mathcal{F}[s_2(\vec{r})] = \int s_2(\vec{r}) \mathrm{e}^{2\pi \mathrm{i} \vec{q}\cdot\vec{r}} \, \mathrm{d}^3 r, \tag{2.16}$$

$$= \int \int s(\vec{\xi}) s(\vec{r} + \vec{\xi}) \mathrm{e}^{2\pi \mathrm{i} \vec{q}\cdot\vec{r}} \, \mathrm{d}^3\xi \, \mathrm{d}^3 r, \tag{2.17}$$

$$= \int \int s(\vec{\xi}) s(\vec{\eta}) \mathrm{e}^{2\pi \mathrm{i} \vec{q}\cdot(\vec{\eta} - \vec{\xi})} \, \mathrm{d}^3\eta \, \mathrm{d}^3\xi, \tag{2.18}$$

$$= \int s(\vec{\eta}) \mathrm{e}^{2\pi \mathrm{i} \vec{q}\cdot\vec{\eta}} \, \mathrm{d}^3\eta \int s(\vec{\xi}) \mathrm{e}^{-2\pi \mathrm{i} \vec{q}\cdot\vec{\xi}} \, \mathrm{d}^3\xi, \tag{2.19}$$

$$= S(\vec{q}) S(-\vec{q}). \tag{2.20}$$

In (2.18), $\vec{r}$ is substituted by $\vec{\eta} = \vec{r} + \vec{\xi}$ which permits the factorization into two Fourier transforms in equation (2.19). By transforming $\vec{\xi} \to -\vec{\xi}$, one arrives at the result in (2.20).

2.2.1.1 Two Examples in one Dimension

In the following the two extreme cases of no structure and perfect structure in *one dimension* will be discussed.

Ideal Crystal

For an ideal crystal, one has $R_j - R_k = na$, where $n \in \mathbb{Z}$ in an arbitrary integer and a is a lattice vector. It follows that

$$
\begin{aligned}
S^{(2)}_{\text{id. crystal}}(q) &= \sum_{j,k=0}^{\infty} \mathrm{e}^{-2\pi \mathrm{i} q(R_j - R_k)} && (2.21)\\
&= \sum_{j=0}^{\infty} \left(\sum_{k=0}^{\infty} \mathrm{e}^{-2\pi \mathrm{i} q(R_j - R_k)} \right) && (2.22)\\
&= \sum_{j=0}^{\infty} \left(\sum_{n=-\infty}^{\infty} \mathrm{e}^{-2\pi \mathrm{i} qna} \underbrace{\mathrm{e}^{-2\pi \mathrm{i} jn}}_{=1} \right) && (2.23)\\
&= \sum_{j=0}^{\infty} \left(\sum_{n=-\infty}^{\infty} \mathrm{e}^{-2\pi \mathrm{i} n(qa-j)} \right) && (2.24)\\
&= 2\pi \sum_{j=0}^{\infty} \delta(2\pi(qa - j)) && (2.25)\\
&= \frac{2\pi}{a} \sum_{j=0}^{\infty} \delta(2\pi q - 2\pi j/a)). && (2.26)
\end{aligned}
$$

The structure factor is zero unless $2\pi q$ equals a reciprocal lattice vector $2\pi j/a$.

Ideally Amorphous Matter

For an ideally amorphous specimen the structure factor can be rewritten as

$$
\begin{aligned}
S^{(2)}_{\text{id. amorphous}}(q) &= \frac{1}{N} \sum_{j,k=1}^{N} \mathrm{e}^{-2\pi \mathrm{i} q(R_j - R_k)} = 1 + \frac{1}{N} \sum_{\substack{j,k=1\\ j\neq k}}^{N} \mathrm{e}^{-2\pi \mathrm{i} q(R_j - R_k)} && (2.27)\\
&= 1 + \left\langle \mathrm{e}^{-2\pi \mathrm{i} q(R_j - R_k)} \right\rangle . && (2.28)
\end{aligned}
$$

Since for an ideally amorphous object the atoms are randomly distributed, the averaging will give zero and hence

$$S^{(2)}_{\text{id. amorphous}}(\vec{q}) = 1. \qquad (2.29)$$

2.2.2 Ideal 2d crystal

For an ideal crystal the distance of two atoms can be written as $\vec{R}_j - \vec{R}_k = n\vec{a}_1 + m\vec{a}_2$, where $n, m \in \mathbb{Z}$ and $\vec{a}_i$ are lattice vectors. The structure factor for a $N \times M$-lattice can then be written as

$$S(\vec{q}) = \sum_{n=0}^{N-1}\sum_{m=0}^{M-1} \mathrm{e}^{2\pi \mathrm{i}\vec{q}\cdot(n\vec{a}_1 + m\vec{a}_2)} = \sum_{n=0}^{N-1} \mathrm{e}^{2\pi \mathrm{i} n\vec{q}\cdot\vec{a}_1} \sum_{m=0}^{M-1} \mathrm{e}^{2\pi \mathrm{i} m\vec{q}\cdot\vec{a}_2} \tag{2.30}$$

The sums can be rewritten using the geometric series

$$\sum_{k=0}^{N-1} \mathrm{e}^{\mathrm{i}k\xi} = \frac{1-\mathrm{e}^{i\xi N}}{1-\mathrm{e}^{i\xi}} = \frac{\mathrm{e}^{\mathrm{i}\xi N/2}}{\mathrm{e}^{\mathrm{i}\xi/2}} \cdot \frac{\mathrm{e}^{-\mathrm{i}\xi N/2} - \mathrm{e}^{\mathrm{i}\xi N/2}}{\mathrm{e}^{-\mathrm{i}\xi/2} - \mathrm{e}^{\mathrm{i}\xi/2}} = \mathrm{e}^{\mathrm{i}\xi(N-1)/2} \frac{\sin(\xi N/2)}{\sin(\xi/2)}. \tag{2.31}$$

Hence the structure factor becomes

$$S(\vec{q}) = \exp\left(\mathrm{i}\pi\vec{q}\cdot[(N-1)\vec{a}_1 + (M-1)\vec{a}_2]\right) \frac{\sin(\pi N\vec{q}\cdot\vec{a}_1)\sin(\pi M\vec{q}\cdot\vec{a}_2)}{\sin(\pi\vec{q}\cdot\vec{a}_1)\sin(\pi\vec{q}\cdot\vec{a}_2)} \tag{2.32}$$

Therefore, the two particle structure factor is

$$S^{(2)}(\vec{q}) = \frac{1}{NM} \frac{\sin^2(\pi N\vec{q}\cdot\vec{a}_1)\sin^2(\pi M\vec{q}\cdot\vec{a}_2)}{\sin^2(\pi\vec{q}\cdot\vec{a}_1)\sin^2(\pi\vec{q}\cdot\vec{a}_2)} \tag{2.33}$$

2.2.3 Three Particle Structure Factor

In analogy to (2.13), one can define the *three particle structure* as [Ham88]

$$\begin{aligned} S^{(3)}(\vec{q}_1, \vec{q}_2) &= \frac{1}{N} S(\vec{q}_1) S(\vec{q}_2) S(-\vec{q}_1 - \vec{q}_2) \\ &= \frac{1}{N} \sum_{j,k,l=1}^{N} \left(\mathrm{e}^{2\pi \mathrm{i}\vec{q}_1\cdot(\vec{R}_j - \vec{R}_l)} \mathrm{e}^{2\pi \mathrm{i}\vec{q}_2\cdot(\vec{R}_k - \vec{R}_l)} \right) \end{aligned} \tag{2.34}$$

The three particle structure factor has the following properties that follow directly from the definition

$$S^{(3)}(\vec{q}_1, \vec{q}_2) = S^{(3)}(\vec{q}_2, \vec{q}_1) = S^{(3)}(\vec{q}_1, -\vec{q}_1 - \vec{q}_2) = \left(S^{(3)}\right)^* (-\vec{q}_1, -\vec{q}_2), \tag{2.35a}$$

$$S^{(3)}(\vec{q}, \vec{0}) = N S^{(2)}(\vec{q}), \tag{2.35b}$$

$$S^{(3)}(\vec{0}, \vec{0}) = N^2. \tag{2.35c}$$

The three particle structure factor can be interpreted as the Fourier transform of a triple correlation [Loh88]

$$s_3(\vec{r}_1, \vec{r}_2) = \int s(\vec{\xi})s(\vec{\xi} + \vec{r}_1)s(\vec{\xi} + \vec{r}_2)\,\mathrm{d}^3\xi, \tag{2.36}$$

since

$$\begin{aligned}
\mathcal{F}[s_3(\vec{r}_1, \vec{r}_2)] &= \int\int s_3(\vec{r}_1, \vec{r}_2)\mathrm{e}^{2\pi\mathrm{i}(\vec{q}_1\cdot\vec{r}_1+\vec{q}_2\cdot\vec{r}_2)}\,\mathrm{d}^3r_1\,\mathrm{d}^3r_2, &(2.37)\\
&= \int\int\int s(\vec{\xi})s(\vec{\xi} + \vec{r}_1)s(\vec{\xi} + \vec{r}_2)\mathrm{e}^{2\pi\mathrm{i}\vec{q}_1\cdot\vec{r}_1}\mathrm{e}^{2\pi\mathrm{i}\vec{q}_2\cdot\vec{r}_2}\,\mathrm{d}^3\xi\,\mathrm{d}^3r_1\,\mathrm{d}^3r_2, &(2.38)\\
&= \int\int\int s(\vec{\xi})s(\vec{\eta})s(\vec{\zeta})\mathrm{e}^{2\pi\mathrm{i}\vec{q}_1\cdot(\vec{\eta}-\vec{\xi})}\mathrm{e}^{2\pi\mathrm{i}\vec{q}_2\cdot(\vec{\zeta}-\vec{\xi})}\,\mathrm{d}^3\xi\,\mathrm{d}^3\eta\,\mathrm{d}^3\zeta, &(2.39)\\
&= \int s(\vec{\xi})\mathrm{e}^{-2\pi\mathrm{i}(\vec{q}_1+\vec{q}_2)\cdot\vec{\xi}}\,\mathrm{d}^3\xi\int s(\vec{\eta})\mathrm{e}^{2\pi\mathrm{i}\vec{q}_1\cdot\vec{\eta}}\,\mathrm{d}^3\eta\int s(\vec{\zeta})\mathrm{e}^{2\pi\mathrm{i}\vec{q}_2\cdot\vec{\zeta}}\,\mathrm{d}^3\zeta, &(2.40)\\
&= S(\vec{q}_1)S(\vec{q}_2)S(-\vec{q}_1 - \vec{q}_2). &(2.41)
\end{aligned}$$

In (2.39) $\vec{\eta} = \vec{r}_1 + \vec{\xi}$ and $\vec{\zeta} = \vec{r}_2 + \vec{\xi}$ are substituted to allow the factorization into three independent integrals.

2.2.4 Distribution Functions

From the structure factors one can derive the so-called *distribution functions* from which one can in turn derive other important physical properties.

2.2.4.1 Pair Distribution Function

Another important set of functions describing matter are distribution functions. Assuming N point-like particles at the positions $\vec{R}_i$, $i \in [1, N]$, in a Volume V. The single-particle density is defined as [Cus87]

$$\nu^{(1)}(\vec{r}) = \sum_{i=1}^{N} \delta(\vec{r} - \vec{R}_i). \tag{2.42}$$

Then

$$\int_V \nu^{(1)}(\vec{r})\,\mathrm{d}^3r = N. \tag{2.43}$$

The two-particle density is defined as

$$\nu^{(2)}(\vec{r}_1, \vec{r}_2) = \sum_{i=1}^{N}\sum_{\substack{j=1\\ j\neq i}}^{N} \delta(\vec{r}_1 - \vec{R}_i)\delta(\vec{r}_2 - \vec{R}_j), \tag{2.44}$$

which is only non-zero if $\vec{r}_1$ and $\vec{r}_2$ are both at the position of lattice sites. Integration over $\vec{r}_2$ yields

$$\begin{aligned}\int_V \nu^{(2)}(\vec{r}_1,\vec{r}_2)\,\mathrm{d}^3r_2 &= \sum_{i=1}^{N}\delta(\vec{r}_1-\vec{R}_i)\sum_{\substack{j=1\\ j\neq i}}^{N}\int_V \delta(\vec{r}_2-\vec{R}_j/d^3r_2),\\ &= \sum_{i=1}^{N}\delta(\vec{r}_1-\vec{R}_i)(N-1) = \nu^{(1)}(\vec{r}_1)(N-1).\end{aligned} \tag{2.45}$$

Usually, the particles in a system are not fixed. Then the distribution function $\nu^{(i)}$ has to be replaced by the time or ensemble average denoted as $n^{(i)} = \langle \nu^{(i)}\rangle$ [Cus87]. Since averaging is a linear operation, all previous expressions for $\nu^{(i)}$ also hold for $n^{(i)}$.

If the particles in the system are interacting, which is usually the case, the probability for a particle occupying $\vec{r}_2$ will depend on that of $\vec{r}_1$ and hence $n^{(2)}(\vec{r}_1,\vec{r}_2) \neq n^{(1)}(\vec{r}_1)n^{(1)}(\vec{r}_2)$. Instead, one defines the pair-distribution function $g^{(2)}$ by

$$n^{(2)}(\vec{r}_1,\vec{r}_2) = n^{(1)}(\vec{r}_1)n^{(1)}(\vec{r}_2)g^{(2)}(\vec{r}_1,\vec{r}_2). \tag{2.46}$$

Since for $|\vec{r}_1-\vec{r}_2|\to\infty$ all interactions are vanishing, one can expect that

$$g^{(2)}(|\vec{r}_1-\vec{r}_2|\to\infty)\to 1. \tag{2.47}$$

If the system is homogeneous, one can write $n^{(1)}(\vec{r}) = n^{(2)}(\vec{r}) = N/V =: n_0$ and equation (2.46) becomes

$$n^{(2)}(\vec{r}_1,\vec{r}_2) = n_0^2 g^{(2)}(\vec{r}_1,\vec{r}_2). \tag{2.48}$$

Let now the origin be at the position of particle 1 and define $\vec{r} = \vec{r}_2-\vec{r}_1$, then [Cus87]

$$n_0\int_V g^{(2)}(\vec{r})\,\mathrm{d}^3r = N-1. \tag{2.49}$$

This leads to the interpretation that $g^{(2)}$ gives the probability of finding a particle between the distances $\vec{r}+\mathrm{d}\vec{r}$ and $\vec{r}$ from another particle at the origin.

Disordered materials are usually isotropic. Consequently, one can replace $g^{(2)}(\vec{r})$ by $g^{(2)}(|\vec{r}|)$. Usually the subscript is neglected in the notation. Examples of pair distribution functions for crystalline and amorphous solids are shown in figure 2.1.

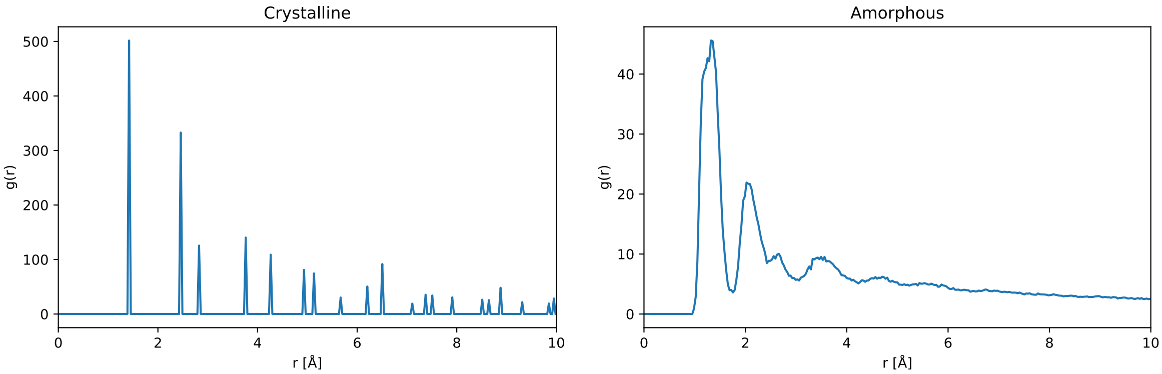

Figure 2.1: Comparison of the pair distribution functions of crystalline and amorphous specimens.

2.2.4.2 Triple Distribution Function

Let $n^{(3)}(\vec{r}_1,\vec{r}_2,\vec{r}_3)$ be defined analogously. Then the triplet distribution function $g^{(3)}(\vec{r}_1,\vec{r}_2,\vec{r}_3)$ can be defined by

$$n^{(3)}(\vec{r}_1,\vec{r}_2,\vec{r}_3) = n^{(1)}(\vec{r}_1)n^{(1)}(\vec{r}_2)n^{(1)}(\vec{r}_3)g^{(3)}(\vec{r}_1,\vec{r}_2,\vec{r}_3). \tag{2.50}$$

By choosing $\vec{r}_3$ as the origin the triplet distribution can be written as $g^{(3)}(\vec{r}_1,\vec{r}_2)$ and since amorphous media are usually isotropic, the distributed function only depends on the particle distances and the angle in-between. It can then be rewritten as $g^{(3)}(r_1,r_2,\vartheta)$. Using this function, the distribution of bond angles can be determined using [Hak95]

$$f(\vartheta) = C\int_0^{r_{\max}}\int_0^{r_{\max}} g^{(3)}(r_1,r_2,\vartheta)r_1^2r_2^2\,\mathrm{d}r_1\mathrm{d}r_2. \tag{2.51}$$

where C is a normalization constant and $r_{\max}$ is the maximal distance between two neighbouring atoms. For thin specimens the isotropy is replaced by rotational symmetry.

2.2.4.3 Relation to the Structure Factor

To relate the structure factor to the distribution function in the case of the two particle distributions one writes the auto-correlation by using $s(\vec{r}) = \sum_j \delta(\vec{r}-\vec{R}_j)$ and eq. (2.15)

$$\begin{aligned} s_2(\vec{r}) &= \frac{1}{N}\int_V \sum_{i,j=1}^{N} \delta(\vec{r}+\vec{r}\,'-\vec{R}_i)\delta(\vec{r}\,'-\vec{R}_j)\,\mathrm{d}^3r' = \frac{1}{N}\sum_{i,j=1}^{N}\delta(\vec{r}-(\vec{R}_i-\vec{R}_j)),\\ &= \frac{1}{N}\sum_{i=1}^{N}\delta(\vec{r}) + \frac{1}{N}\sum_{\substack{i,j=1\\ i\neq j}}^{N}\delta(\vec{r}-(\vec{R}_i-\vec{R}_j)), \end{aligned}$$

$$= \delta(\vec{r}) + n_0 g^{(2)}(\vec{r}). \tag{2.52}$$

In the first line, only the definitions of S and $S^{(2)}$, respective their Fourier transforms, were inserted and the integration was performed to remove one delta function. In the second line, the summations over $i = j$ and $i \neq j$ were separated and finally, in the last line, the definition of $g^{(2)}$ was used.
By Fourier transforming, one gets

$$\begin{aligned}\hat{S}^{(2)}(\vec{q}) &= \int (\delta(\vec{r}) + n_0 g^{(2)}(\vec{r}))\mathrm{e}^{\mathrm{i}\vec{q}\cdot\vec{r}}\,\mathrm{d}^3r \\ &= 1 + n_0 \int g^{(2)}(\vec{r})\mathrm{e}^{\mathrm{i}\vec{q}\cdot\vec{r}}\,\mathrm{d}^3r, \\ &= 1 + n_0 \int_0^\infty g^{(2)}(r)\frac{\sin qr}{qr}4\pi r^2\,\mathrm{d}r,\end{aligned} \tag{2.53}$$

where in the last line spherical coordinates were introduced. Hence $S^{(2)} - 1$ and $n_0 g^{(2)}$ are Fourier transform pairs.
Analogously, one calculates for the triplet structure factor starting from the triplet correlation as defined in eq. (2.36)

$$\begin{aligned}s_3(\vec{r}_1, \vec{r}_2) &= \frac{1}{N}\int \sum_{i,j,k=1}^{N} \delta(\vec{\xi} + \vec{r}_1 - \vec{R}_i)\delta(\vec{\xi} + \vec{r}_2 - \vec{R}_j)\delta(\vec{\xi} - \vec{R}_k)\,\mathrm{d}^3\xi, \\ &= \frac{1}{N}\sum_{i,j,k=1}^{N} \delta(\vec{r}_1 - (\vec{R}_i - \vec{R}_k))\delta(\vec{r}_2 - (\vec{R}_j - \vec{R}_k)).\end{aligned}$$

The sum is now separated into sums with $i = j, k$; $j = k, i$; $k = i, j$ and one sum with $i \neq j$, $i \neq k$ and $j \neq k$. Since the addend with $i = j = k$ is now appearing three times it has to be subtracted twice. Then one gets

$$\begin{aligned}s_3(\vec{r}_1, \vec{r}_2) = &\underbrace{\frac{1}{N}\sum_{i,j=1}^{N} \delta(\vec{r}_1)\delta(\vec{r}_2 - (\vec{R}_j - \vec{R}_i))}_{i=k} + \underbrace{\frac{1}{N}\sum_{i,j=1}^{N} \delta(\vec{r}_2)\delta(\vec{r}_1 - (\vec{R}_i - \vec{R}_j))}_{j=k} \\ &+ \underbrace{\frac{1}{N}\sum_{i,k=1}^{N} \delta(\vec{r}_1 - (\vec{R}_i - \vec{R}_k))\delta(\vec{r}_2 - (\vec{R}_i - \vec{R}_k))}_{i=j}\end{aligned}$$

$$-\frac{2}{N}\underbrace{\sum_{i=1}^{N}\delta(\vec{r}_1)\delta(\vec{r}_2)}_{i=j=k}+\frac{1}{N}\sum_{\substack{i,j,k=1\\ i\neq j,\ i\neq k,\ j\neq k}}^{N}\delta(\vec{r}_1-(\vec{R}_i-\vec{R}_k))\delta(\vec{r}_2-(\vec{R}_j-\vec{R}_k)). \tag{2.54}$$

The last term equals $n_0^2 g^{(3)}(\vec{r}_1,\vec{r}_2)$. By Fourier transforming one finds

$$\begin{aligned}\hat{S}^{(3)}(\vec{q}_1,\vec{q}_2) = {} & \hat{S}^{(2)}(\vec{q}_1)+\hat{S}^{(2)}(\vec{q}_2)+\hat{S}^{(2)}(\vec{q}_1+\vec{q}_2)-2\\ & + n_0^2\int\int g^{(3)}(\vec{r}_1,\vec{r}_2)\mathrm{e}^{\mathrm{i}(\vec{q}_1\cdot\vec{r}_1+\vec{q}_2\cdot\vec{r}_2)}\,\mathrm{d}^3r_1\mathrm{d}^3r_2.\end{aligned} \tag{2.55}$$

Consequently, the three particle structure factor consists of the two particle structure factors at $\vec{q}_1$, $\vec{q}_2$ and $\vec{q}_3$ and the Fourier transform of the three particle distribution function.

Chapter 3

Electron Microscopy

To determine the structure of amorphous specimens we used *transmission electron microscope* (TEM) images. In this chapter, the basic design of a TEM is presented and it will be shown that for *weak phase objects* the image contrast in reciprocal space is proportional to the structure factor. This will be used throughout this thesis to obtain the three particle structure factor. In section 3.3, a short description of the *multislice algorithm* will be given which will be used to simulated TEM images.

3.1 Description of the Electron Microscope

In principle electron microscopes work similar to light microscopes. A schematic design is shown in figure 3.1. While the resolution in light microscopes is limited by the wavelengths of visible light one can in principle achieve much smaller wavelengths with electrons by accelerating them. The electron source consists usually of a cathode that generates the electrons which are then accelerated through some high voltage [Koh].

The lenses consist of coils whose magnetic field is focussing the electron beam. The condenser lens determines the illuminated area of the specimen and the objective lens creates the intermediate image of the specimen. The intermediate image is then enlarged by the projector lens.

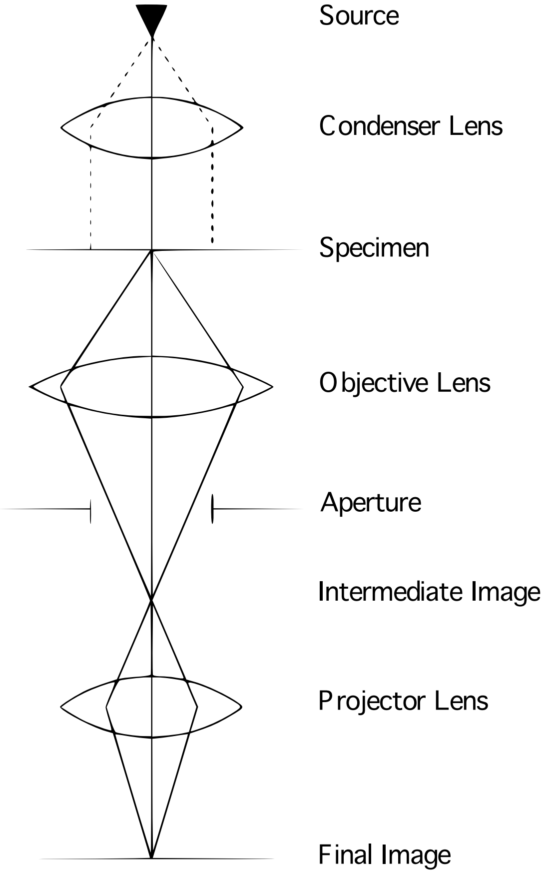

Figure 3.1: Schematic image of a transmission electron microscopy. Adapted from [Koh].

3.2 Phase Contrast Imaging

The specimen can be described by a specimen function $f(\vec{r})$. Each point is mapped by the microscope to a region in the image[1] [WC09]

$$g(\vec{r}) = \int f(\vec{r}')h(\vec{r}-\vec{r}')\, \mathrm{d}^2 r = f(\vec{r}) * h(\vec{r}). \tag{3.1}$$

Since the function h describes how a point in the specimen spreads onto a disc in the image it is called *point spread function*. In Fourier space this convolution simplifies to a simple product

$$\mathcal{G}(\vec{q}) = \mathcal{F}(\vec{q})\mathcal{H}(\vec{q}). \tag{3.2}$$

$\mathcal{H}$ is also called *contrast transfer function*. For small deviation from the optical axis, it can be factored in effects from the apertures, the damping of the wave and the aberration of the lens which can respectively be described by an *aperture function* $\mathcal{A}(\vec{q})$, an *envelope function* $\mathcal{E}(\vec{q})$ and an *aberration function* $\mathcal{B}(\vec{q})$. The aperture function cuts off all values with a spatial frequency above a threshold depending on the radius of the aperture. The envelope function has the same effect but stems from the lenses. Since those effects should be spherically symmetric, both functions actually depend only on $q = |\vec{q}|$. The aberration function is usually expressed as $\mathcal{B}(\vec{q}) = \exp(\mathrm{i}\chi(\vec{q}))$ with [Kir10]

$$\chi(\vec{q}) = \pi \Delta f \lambda q^2 + \frac{1}{2}\pi C_s \lambda^3 q^4 + \frac{1}{3}\pi C_5 \lambda^5 q^6. \tag{3.3}$$

Δf is the defocus and C_s and C_5 is the third and fifth order spherical aberration, respectively [Kir10]. For aberration corrected microscopes C_s is variable and one can find optimal values for Δf and C_s to minimize the influence of the C_5 term [CKT06].

The specimen can be modelled as $f(x,y) = A(x,y)\exp(-\mathrm{i}\phi_t(x,y))$. It will be assumed that $A(x,y) = 1$, i.e. that the specimen acts only on the phase of the incoming electrons and that the specimen thickness t is thin enough that it is sufficient to consider its projected potential

$$V_t(x,y) = \int_0^t V(x,y,z)\, \mathrm{d}z. \tag{3.4}$$

---

[1] The $*$ denotes the convolution.

The incoming electrons with energy E have a wavelength in the vacuum of

$$\lambda = \frac{h}{\sqrt{\frac{E^2}{c^2} - m^2c^4}}. \tag{3.5}$$

m is the mass of the electron, h is Planck's constant and c is the speed of light in the vacuum. Inside the specimen this wavelength is altered to

$$\lambda' = \frac{h}{\sqrt{\frac{(E+V(x,y,z))^2}{c^2} - m^2c^4}}. \tag{3.6}$$

This corresponds to a phase change $\mathrm{d}\phi$ when passing a length $\mathrm{d}z$ inside the specimen of

$$\begin{aligned}
\mathrm{d}\phi &= 2\pi\frac{\mathrm{d}z}{\lambda'} - 2\pi\frac{\mathrm{d}z}{\lambda} && (3.7)\\
&= 2\pi\frac{\mathrm{d}z}{\lambda}\left(\sqrt{\frac{\frac{(E+V(x,y,z))^2}{c^2} - m^2c^2}{\frac{E^2}{c^2} - m^2c^2}} - 1\right) && (3.8)\\
&\approx 2\pi\frac{\mathrm{d}z}{\lambda}\frac{EV(x,y,z)}{E^2 - m^2c^4} && (3.9)\\
&= \frac{2\pi}{\lambda}\frac{E}{E^2 - m^2c^4}V(x,y,z)\mathrm{d}z && (3.10)\\
&= \sigma V(x,y,z)\mathrm{d}z && (3.11)
\end{aligned}$$

where in equation (3.9) the square root was Taylor expanded up to first order and in the last line the interaction constant $\sigma = \frac{\pi}{\lambda}\frac{E}{E^2-m^2c^4}$ was introduced. The total phase shift can then be written as

$$\phi_t = \sigma\int_0^t V(x,y,z)\,\mathrm{d}z = \sigma V_t(x,y) \tag{3.12}$$

and hence the specimen function is

$$f(x,y) = \exp(-\mathrm{i}\sigma V_t(x,y)). \tag{3.13}$$

In the so-called *weak phase object approximation* (WPOA) one assumes that for very thin specimens $\sigma V_t(x,y) \ll 1$ and therefore

$$f(x,y) = 1 - \mathrm{i}\sigma V_t(x,y). \tag{3.14}$$

In this approximation, the amplitude of the transmitted wave function depends linearly on the projected potential [HGJ79]

$$\psi(x,y) = (1 - \mathrm{i}\sigma V_t(x,y)) * h(x,y) = 1 * h(x,y) - \mathrm{i}\sigma V_t(x,y) * h(x,y). \tag{3.15}$$

The first term can best be evaluated in Fourier space

$$\begin{aligned} \delta(\vec{q})\mathcal{H}(\vec{q}) &= \delta(\vec{q})\mathcal{A}(\vec{q})\mathcal{E}(\vec{q})\exp(\mathrm{i}\chi(\vec{q})) && (3.16)\\ &= \delta(\vec{q})\mathcal{A}(\vec{0})\mathcal{E}(\vec{0}) && (3.17)\\ &= \delta(\vec{q}) && (3.18) \end{aligned}$$

In the last line it was used that the aberration function and the envelope function behave like unity below their cut-off value. For the second term in (3.15), the point spread function is split into its real and imaginary part, $h(x,y) = c(x,y) + \mathrm{i}s(x,y)$, leading to

$$\psi(x,y) = 1 + \sigma V_t(x,y) * s(x,y) - \mathrm{i}\sigma V_t(x,y) * c(x,y). \tag{3.19}$$

The intensity is then given as

$$I(x,y) = |\psi(x,y)|^2 = 1 + 2\sigma V_t(x,y) * s(x,y) \tag{3.20}$$

where the terms quadratic in σV_t were neglected. The image *contrast* is then defined as [Hak95]

$$C(x,y) = \frac{I(x,y)}{\langle I \rangle} - 1 = 2\sigma V_t(x,y) * s(x,y) \tag{3.21}$$

where $\langle I \rangle = \int I(x,y)\,\mathrm{d}x\mathrm{d}y = 1$ is the average image density. In order to incorporate the individual atom positions $\vec{r}_i$ the potential is expressed as a convolution of single-particle potentials $\phi(r)$ with the structure function

$$S(\vec{r}) = \sum_{i=1}^{N} \delta(\vec{r} - \vec{r}_i), \tag{3.22}$$

resulting in the contrast

$$C(\vec{r}) = 2\sigma\phi(r) * s(\vec{r}) * S(\vec{r}). \tag{3.23}$$

In Fourier space this leads to

$$\boxed{C(\vec{q}) = 2\lambda f_B(q) L(q) S(\vec{q})} \tag{3.24}$$

with the *atomic form factor* f_B, the *one particle structure factor* $S(\vec{q})$ and the *phase contrast transfer function*

$$L(q) = \mathcal{A}(\vec{q})\mathcal{E}(\vec{q}) \sin(\chi(\vec{q})). \tag{3.25}$$

So the Fourier transform of the contrast factorises into separate contributions from the atomic properties of the specimen, the properties of the electron microscope and the lattice structure.

3.3 Multislice Simulations

The multislice algorithm is a method to enable the simulation of TEM images of specimens with arbitrary thickness [Koh]. It does so by splitting the specimen into slices that are thin enough to be treated as simple transmission functions

$$T_n(\vec{\rho}_n) = \exp\left(-\frac{\mathrm{i}}{\hbar v}\int_{(n-1)\Delta z}^{n\Delta z} V(\vec{\rho}_n, z)\right), \tag{3.26}$$

where $\vec{\rho}_n = (x_n, y_n)$ is the planar coordinate on the n-th slice. The transmission is then described by

$$\psi'_n(\vec{\rho}_n) = T_n(\vec{\rho}_n)\psi_n(\vec{\rho}_n) \tag{3.27}$$

and the propagation to the next slice by

$$\psi_{n+1}(\vec{\rho}_{n+1}) = \frac{\exp(\mathrm{i}k\Delta z)}{\mathrm{i}\lambda\Delta z}\int \psi'_n(\vec{\rho}_n)\exp\left(\mathrm{i}\frac{k}{2\Delta z}(\vec{\rho}_{n+1} - \vec{\rho}_n)^2\right)\,\mathrm{d}^2\rho_n. \tag{3.28}$$

The wavefunction after the specimen is then obtained by iteratively applying the transmission and the propagation to the incoming wave function. This is shown schematically in figure 3.2

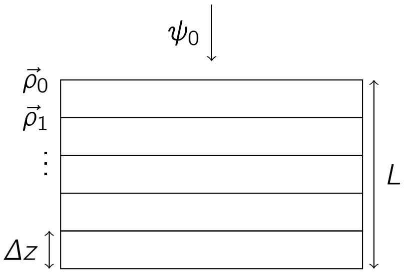

Figure 3.2: The basic idea of the multislice algorithm. A specimen with thickness L is split into slices with much smaller thickness Δz.

In this thesis all multislice simulations are performed with the TEMSIM program from [Kir10].

Chapter 4

Models of Amorphous Solids

4.1 Random Close Packing

The simplest structural model of an amorphous substance is that of an irregular packing of hard spheres [Zim79; Sta15]. This is also a good model for liquids [Zim79].
Random close packings are not a well-defined structure and there are many possible algorithms for creating them [Ber83; BM91; NK92; TTD00].

4.1.1 Implementation

The implementation used for this thesis is an adapted version of the program presented in [BM91]. The idea is to start from an ensemble of particles that are randomly distributed in a box with periodic boundary positions. In each iteration largest overlap between two particles is eliminated by moving those particles apart.
The program starts from an box of volume $V = L^3$ with N particles. For each particle, two diameters are defined. An inner and a outer one that approach each other during the simulation. The inner diameter d_{in}^n after iteration n is defined as the minimal actual distance between any two particles in the system,

$$d_{\text{in}}^n = \min r_{ij}^n, \qquad i, j = 1, \dots, N, \qquad i \neq j, \tag{4.1}$$

where $r_{ij}^n = |\vec{r}_i^{\,n} - \vec{r}_j^{\,n}|$ is the distance between the particles i and j after the n-th iteration. On average, the inner diameter increases with every iteration.
The outer diameter is initially defined as

$$d_{\text{out}}^0 = 2L\sqrt[3]{\frac{3\eta}{4\pi N}}, \tag{4.2}$$

which yields a nominal packing density η. After each iteration the outer diameter is reduced by a given contraction rate τ which results in[1]

$$d_{\text{out}}^{n+1} = \left(\frac{1}{2}\right)^{\delta} \frac{d_{\text{out}}^{n}}{N\tau} \tag{4.3}$$

$$\delta = \lfloor -\log\left(d_{\text{out}}^{n} - d_{\text{in}}^{n}\right) \rfloor \tag{4.4}$$

The outer spheres can intersect. In each iteration the largest overlap is eliminated by moving the closest particles according to

$$\vec{r}_i^{\,n+1} = \vec{r}_i^{\,n} + \frac{1}{2}\left(d_{\text{out}}^{n+1} - r_{ij}^{n}\right)\frac{\vec{r}_{ij}^{\,n}}{r_{ij}^{n}}, \tag{4.5a}$$

$$\vec{r}_j^{\,n+1} = \vec{r}_j^{\,n} - \frac{1}{2}\left(d_{\text{out}}^{n+1} - r_{ij}^{n}\right)\frac{\vec{r}_{ij}^{\,n}}{r_{ij}^{n}}. \tag{4.5b}$$

Their new distance is then $r_{ij}^{n+1} = d_{\text{out}}^{n+1}$. An example for the so-created random close packing is shown in fig. 4.1a.

The implementation maintains an array of all particles storing their position in the box, the index of their closest neighbour particle and the distance to it. After each iteration the algorithm has to find new closest neighbour particles for i and j by searching all other particles. Then for all other particles it has to be checked if i or j were their closest neighbours. If that is true, a new closest neighbour has to found by searching all particles. If that is false it has only to be checked if i or j became the new closest neighbour. The complexity of this algorithm scales linearly with the number of particles N. The adaption to two dimensions is straight-forward.

After the simulation was run, one can achieve a next neighbour distance a by rescaling the simulated box by a factor a/d_{in}^{n}. Fig. 4.1b shows the radial distribution function of a random close packing with a closest distance $d = 1$. One finds $g(r) = 0$ for all $r < 1$ since the particles are modelled as hard balls that cannot penetrate each other. For $r = 1$, there is a large peak. For $r = 2$ and $r = 3$, there are also peaks, but they are an order of magnitude smaller. For even larger r, there is no structure visible.

---

[1] The brackets in $\lfloor x \rfloor$ denote the floor-function which returns the largest integer smaller than x.

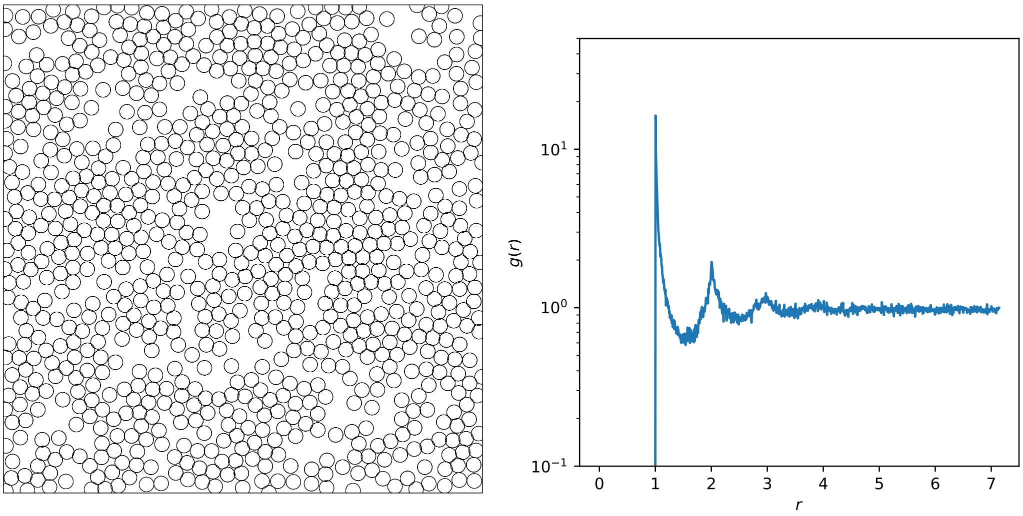

(a) Example for a random close packing in two dimensions

(b) The radial distribution function

Figure 4.1: An example random close packing and its radial distribution function. The particle next neighbour distance was chosen to be $d = 1$ in arbitrary units.

4.2 Random Plates

In [Eus84] it is argued that thin carbon films can be modelled as an ensemble of parallel, equidistant plates of crystalline carbon that are randomly distributed just like the random close packings in the previous section. One such plate is shown in figure 4.2. For the simulation a random close packing is simulated as in section 4.1, which is then rescaled to the radius of the desired plate size. In the last step, the spheres from the RCP are replaced with the atoms of the plate with the plate being rotated by a different random angle for each ball.

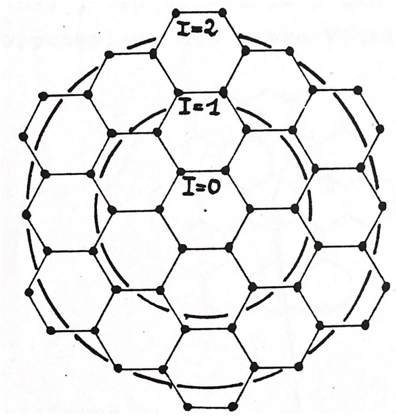

Figure 4.2: One crystalline plate. Taken from [Eus84].

4.3 Continuous Random Networks

The idea of a continuous random network (CRN) was first proposed by W. H. Zachariasen [Zac32] in 1932.

4.3.1 The WWW algorithm

One way to systematically generate CRNs is the Wejchert - Weaire - Wooten (WWW) algorithm [WWW85]. In the original version, one starts from an ideal crystal and repeatedly introduces bond switches and relaxes the newly build bonds. The produced state is called *Sillium*. It is defined as follows [WWW90]

1. Each atom is bound to four neighbour atoms.
2. The energy of the system is described by the Keating potential (4.6).
3. The only degree of freedom consists of bond transpositions.
4. Periodic boundary conditions are employed.
5. Monte Carlo rules are employed to carry out the structural rearrangements.

The steps of the algorithm will be described in more detail below. The general approach is to thermalize a periodic honeycomb lattice at some temperature above the glass temperature. For $\alpha/\beta = 0.285$ the glass temperature is $1\,\mathrm{eV}/\mathrm{k_B}$ [WW87]. This so-produced random state is cooled down to produce amorphous silicon.

4.3.1.1 Bond Transpositions

The network is stored as a so-called adjacency-list graph [Cor+09], i.e. as an array of particles where for each particle its position and the indices of its next neighbours are stored.

The bond transpositions are done in way that introduces minimal strain. This is achieved by ensuring that the bonds that are switched do not belong to the same ring [WW95]. First, one randomly picks 4 particles, $p_1, \dots, p_4$, that form a chain. Then one searches for all simple paths[2] from p_2 to p_3. For a two-dimensional network, this returns two rings and one can simply check if p_1 and p_4 belong to the same ring. If that is the case one generates a new random chain. Otherwise, one proceeds with the relaxation step below.

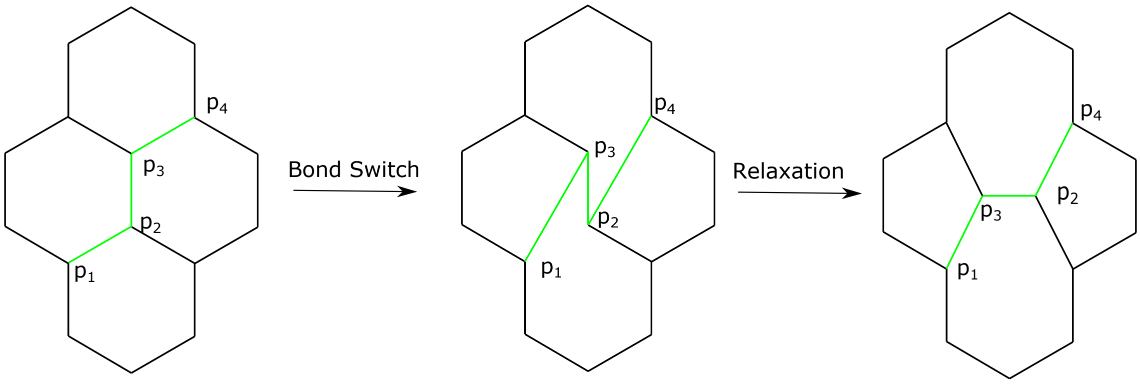

Figure 4.3: Visualization of one bond transposition. In this case, four rings consisting of six atoms each are replaced by two rings with five atoms and two rings with seven atoms.

4.3.1.2 Relaxation

The bonding of the atoms inside a CRN is described by the *Keating potential* [Kea66] as a sum of a bond-bending and a bond-stretching term. In the three-dimensional case this has the form [WW95].

$$E = \frac{3}{16}\frac{\alpha}{d^2}\sum_{\langle ab\rangle}\left(|\vec{r}^{ab}|^2 - d^2\right)^2 + \frac{3}{8}\frac{\beta}{d^2}\sum_{\langle abc\rangle}\left(\vec{r}^{ab}\cdot\vec{r}^{ac} + \frac{1}{3}d^2\right)^2. \tag{4.6}$$

The angled braces denote summation over nearest neighbours and $\vec{r}^{ab} = \vec{r}^{b} - \vec{r}^{a}$. For $r^{ab}, r^{ac} \approx d$, one can rewrite the term inside the second parentheses as $\vec{r}^{ab}\cdot\vec{r}^{ac} + d^2/3 \approx d^2(\cos\theta - \cos\theta_0)$ where θ denoted the angle between $\vec{r}^{ab}$ and $\vec{r}^{ac}$ and $\theta_0 = \arccos(-1/3) \approx 109.5°$ is the tetrahedral angle. From this, one can see that the energy is minimal if all bond lengths are d and all bond angles are θ_0.

In the WWW algorithm, the Keating potential plays a double role as it serves as the source of the particle displacements on one side, as shown below, and on the other side it appears in the Boltzmann factor $e^{\Delta E/T}$ guiding the annealing.

For a two-dimensional model of amorphous silica, one expects a deformed honeycomb lattice

---

[2] Paths in a graph are called *simple* if the do not contain cycles. To find these paths, an adaption from [HSS08]. was used

where the bond angle in the ideal case is $\theta_0 = 120°$ and hence $\cos\theta_0 = -1/2$. So for the 2d case once can write

$$E = \frac{3}{16}\frac{\alpha}{d^2}\sum_{\langle ab\rangle}\left(|\vec{r}^{ab}|^2 - d^2\right)^2 + \frac{3}{8}\frac{\beta}{d^2}\sum_{\langle abc\rangle}\left(\vec{r}^{ab}\cdot\vec{r}^{ac} + \frac{1}{2}d^2\right)^2 . \tag{4.7}$$

This energy can be rewritten as a sum of one particle energies $E = \sum_a \epsilon^a$ [Vin+01] where

$$\epsilon^a = \sum_{b=1}^{3}\left[\frac{3}{32}\frac{\alpha}{d^2}\left(|\vec{r}^{ab}|^2 - d^2\right)^2 + \sum_{c=b+1}^{3}\frac{3}{8}\frac{\beta}{d^2}\left(\vec{r}^{ab}\cdot\vec{r}^{ac} + \frac{1}{2}d^2\right)^2\right]. \tag{4.8}$$

After switching bonds, the atoms inside the cluster experience a force according to the Keating potential until they reach an energetic minimum. By expanding the force around a minimum, one finds[3]

$$(\vec{\nabla}\epsilon^a)(\vec{r}^a) = -(\operatorname{hess}\epsilon^a)(\vec{r}^a)\Delta\vec{r}^a \tag{4.9}$$

or for the i-th component

$$\frac{\partial\epsilon^a}{\partial x_i} = -\frac{\partial^2\epsilon^a}{\partial x_i\partial x_j}\Delta x_j . \tag{4.10}$$

Hence the atom at $\vec{r}^a$ has to be moved by $\Delta\vec{r}^a = -(\operatorname{hess}\epsilon^a)^{-1}(\vec{r}^a)(\vec{\nabla}\epsilon^a)(\vec{r}^a)$. This has to be done iteratively for each atom inside a given neighbourhood of the the bond switch until the system converges to equilibrium.

When inserting eq. (4.8) in eq. (4.9), the following derivatives are needed[4]

$$\begin{aligned}\frac{\partial\epsilon^a}{\partial x_i^a} &= \frac{\partial}{\partial x_i^a}\sum_{b=1}^{3}\left[\frac{3}{32}\frac{\alpha}{d^2}\left((x_k^{ab})^2 - d^2\right)^2 + \sum_{c=b+1}^{3}\frac{3}{8}\frac{\beta}{d^2}\left(x_k^{ab}x_k^{ac} + \frac{1}{2}d^2\right)^2\right],\\ &= -\sum_{b=1}^{3}\left[\frac{3}{8}\frac{\alpha}{d^2}\left((x_k^{ab})^2 - d^2\right)x_i^{ab} + \sum_{c=b+1}^{3}\frac{3}{4}\frac{\beta}{d^2}\left(x_k^{ab}x_k^{ac} + \frac{1}{2}d^2\right)\left(x_i^{ab} + x_i^{ac}\right)\right].\end{aligned} \tag{4.11}$$

$$\frac{\partial^2\epsilon^a}{\partial x_i^a\partial x_j^a} = -\frac{\partial}{\partial x_j^a}\sum_{b=1}^{3}\left[\frac{3}{8}\frac{\alpha}{d^2}\left((x_k^{ab})^2 - d^2\right)x_i^{ab} + \sum_{c=b+1}^{3}\frac{3}{4}\frac{\beta}{d^2}\left(x_k^{ab}x_k^{ac} + \frac{1}{2}d^2\right)\left(x_i^{ab} + x_i^{ac}\right)\right],$$

---

[3] hess denotes the Hessian matrix consisting of all second derivatives of a multidimensional function, i.e. $(\operatorname{hess} f)(x_1,\ldots,x_n) = (\partial^2 f/\partial x_i\partial x_j)_{i,j\in[1,n]}$.

[4] The upper indices (a, b, c) enumerate particles while the lower indices (i, j, k) enumerate Cartesian coordinates. Over doubly appearing Cartesian indices will be summed implicitly unless otherwise noticed.

$$
\begin{aligned}
= \sum_{b=1}^{3} \Bigg[& \frac{3}{8}\frac{\alpha}{d^2}\left(2x_i^{ab}x_j^{ab} + \left((x_k^{ab})^2 - d^2\right)\delta_{ij}\right) \\
& + \sum_{c=b+1}^{3} \frac{3}{4}\frac{\beta}{d^2}\left(\left(x_i^{ab}+x_i^{ac}\right)\left(x_j^{ab}+x_j^{ac}\right) + 2\left(x_k^{ab}x_k^{ac} + \frac{1}{2}d^2\right)\delta_{ij}\right)\Bigg]. \qquad (4.12)
\end{aligned}
$$

Let $\epsilon_{ij}^a = \partial^2\epsilon^a/\partial x_i^a \partial x_j^a$ and $D = \det(\operatorname{hess}\epsilon^a) = \epsilon_{11}^a\epsilon_{22}^a - (\epsilon_{12}^a)^2$, then the inverse Hessian matrix can be calculated as

$$
(\operatorname{hess}\epsilon^a)^{-1} = \begin{pmatrix} \epsilon_{11}^a & \epsilon_{12}^a \\ \epsilon_{12}^a & \epsilon_{22}^a \end{pmatrix}^{-1} = \frac{1}{D}\begin{pmatrix} \epsilon_{22}^a & -\epsilon_{12}^a \\ -\epsilon_{12}^a & \epsilon_{11}^a \end{pmatrix}. \qquad (4.13)
$$

4.4 Liquid Quenching

In [TSM16], the authors performed molecular dynamics (MD) simulations with different carbon interaction potentials to produce clusters of amorphous carbon. The simulation followed a specific temperature curve to achieve this. First the carbon was melted at 6000 K-8000 K which was followed by cooling the carbon to almost 0 K. In the end, the carbon was annealed at room temperature. The procedure is illustrated in figure 4.4. They were able to find some differences in the resulting materials in observables like the radial distribution function and ring statistics.

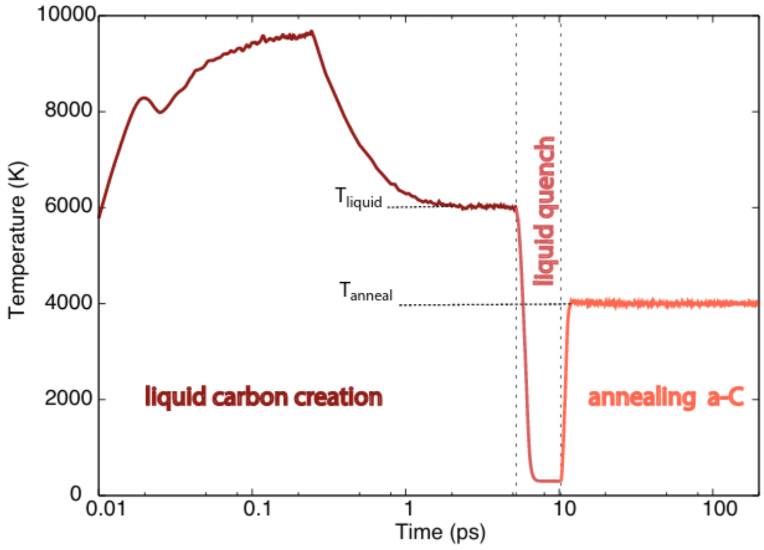

Figure 4.4: The evolution of the system temperature during the liquid quenching procedure. Taken from [TSM16].

4.5 Summary

The first three models presented in this chapter are all somewhat artificial. Random Close Packings represent an ideal amorphous solid [Sta15]. They lack any order apart from having a minimal possible particle distance. The Random Plates model extends this model by having small areas inside the specimen with high order. The size of the plates can be easily controlled.

The Continuous Random Networks are more realistic since they have a notion of atomic bonds. But the dynamic consisting only of bond switches and relaxations is rather artificial.

All three models have the advantage that they are easy to study and not computationally expensive.

The Liquid Quenching method is the most realistic. The algorithm follows a realistic mechanism to create an amorphous solid but the results depend highly on the inter-atomic potentials used.

Chapter 5

Results

In this chapter, various results for the three particle structure factor from experiments and also from simulations are presented. The first section shows how the three particle structure factor can be displayed graphically and uses then the results from chapter 3 to present a method for extracting information about the three particle structure factor from phase contrast images. The subsequent sections then present and discuss the findings for different specimens and structure models.

5.1 Representation

For weak phase objects, one can write the Fourier transform of the obtained image as (see eq. (3.24))

$$C(\vec{q}) = 2\lambda f_B(q)L(q)S(\vec{q}) \tag{5.1}$$

This can be used to obtain the structure factor S. The easiest way to do this is to assume that $2\lambda f_B(q)L(q) \approx const$ for all relevant q. This holds only for ideal imaging, i.e. when aberrations can be neglected and for very thin one-atomic specimens or multi-atomic specimens where one element dominates in the diffraction processes.
Another approach that was used in [Ham88] uses the fact that the expression $2\lambda f_B(q)L(q)$ is a real-valued function. Thus one can write

$$\frac{C(\vec{q})}{|C(\vec{q})|} = \frac{2\lambda f_B(q)L(q)S(\vec{q})}{|2\lambda f_B(q)L(q)S(\vec{q})|} = \frac{S(\vec{q})}{|S(\vec{q})|}, \tag{5.2}$$

since $|2\lambda f_B(q)L(q)| = 2\lambda f_B(q)L(q)$. This is only valid up to the first root of $L(q)$ and looses information about the magnitude of S but is nevertheless able to obtain some useful information.

Using that the expression $2\lambda f_B(q)L(q)$ is only depending on the modulus of $\vec{q}$, one can write the radial average of the image by using polar coordinates as

$$\begin{aligned} \langle|C|\rangle(q) &= \frac{1}{2\pi}\int_0^{2\pi} |C(q,\phi)|\,\mathrm{d}\phi \qquad (5.3)\\ &= \frac{1}{2\pi}2\lambda f_B(q)L(q)\int_0^{2\pi} |S(q,\phi)|\,\mathrm{d}\phi \qquad (5.4)\\ &= 2\lambda f_B(q)L(q)\langle|S|\rangle(q). \qquad (5.5)\end{aligned}$$

This can be used to define the quantity

$$\hat{S}(\vec{q}) = \frac{C(\vec{q})}{\langle|C|\rangle(q)} = \frac{S(\vec{q})}{\langle|S|\rangle(q)}, \qquad (5.6)$$

which is independent of $f_B(q)$ and $L(q)$ but has the same phase as S and, for fixed q, its maxima at the same angles ϕ. The maximum here is defined in terms of the modulus. On the right hand side we can find the definition of the structure factor (see eq. (2.11)). This can be used to obtain the two and three particle structure factor by using equations (2.13) and (2.34). The different normalization strategies are compared in figure 5.4.

5.1.1 Averaged three particle structure factor

Since $S^{(3)}$ has 4 degrees of freedom (see fig 5.1) one has to find a representation that condenses the information into less dimensions.

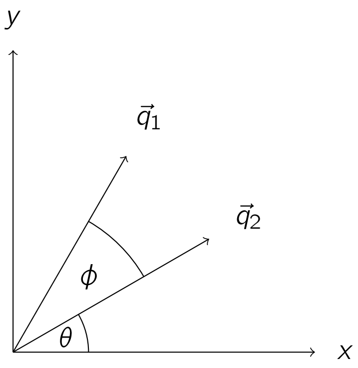

Figure 5.1: All 4 degrees of freedom of the three particle structure factor.

Assuming amorphous matter to be isotropic, we average over one spatial angle and considere $S^{(3)}$ as a function of now only three variables $q_1 = |\vec{q}_1|$, $q_2 = |\vec{q}_2|$ and $\phi = \sphericalangle(\vec{q}_1, \vec{q}_2)$. Then the number of degrees of freedom is reduced even more by confining our interest to $q_1 = q_2 =: q$ and varying only q and ϕ. This can be summarized as

$$\langle \hat{S}^{(3)} \rangle (q, \phi) = \frac{1}{A(q, \phi)} \int\limits_{\substack{|\vec{q}_1| = |\vec{q}_2| = q \\ \sphericalangle(\vec{q}_1, \vec{q}_2) = \phi}} \hat{S}(\vec{q}_1) \hat{S}(\vec{q}_2) \hat{S}(-\vec{q}_1 - \vec{q}_2) \mathrm{d}^2 q_1 \mathrm{d}^2 q_2 \tag{5.7}$$

$$\begin{aligned} &= \frac{1}{2\pi q^2} \int_0^{2\pi} \hat{S}(q\cos(\phi + \theta), q \sin(\phi + \theta)) \hat{S}(q \cos\theta, q \sin\theta) \\ &\quad \times \hat{S}(-q(\cos(\phi + \theta) + \cos\theta), -q(\sin(\phi + \theta) + \sin\theta)) \, \mathrm{d}\theta \end{aligned} \tag{5.8}$$

where $A(q, \phi) = 2\pi q^2$ is the area of the hypersurface defined by fixing q and ϕ. This will be proven in appendix A.

Since the pixels in an image have a finite width, one cannot resolve arbitrarily small distances. This corresponds to a maximal q_i in Fourier space

$$q_{i,\max} = \frac{\text{number of pixels}}{2 \times \text{width}}. \tag{5.9}$$

This means that a TEM image with 2048×2048 pixels of an area of $400\,\text{Å} \times 400\,\text{Å}$ has $q_{\max} = 2.56\,\text{Å}^{-1}$ in both directions. On the other hand the length of $\vec{q}_3$

$$q_3 = |\vec{q}_3| = |\vec{q}_1 + \vec{q}_2| = q\sqrt{2(1 + \cos\phi)} \in [0, 2q] \tag{5.10}$$

can become larger than the available reciprocal space. This will lead to some undefined areas in the resulting three particle structure factors. In the example above the three particle structure factor can only be completely obtained up to $q = 1.28\,\text{Å}^{-1}$. The contour lines for q_3 are shown in figure 5.2.

5.1.2 Comparison of normalization strategies

In figure 5.4, this procedure is applied to an amorphous silica specimen laying on top of a graphene substrate and to a gold nano-cluster on a carbon layer. In the first row, no normalization method was applied. The silica specimen shows two peaks for $q \approx 0.25\,\text{Å}^{-1}$ at around 60° and 120° which is reasonable for a specimen that forms hexagonal lattices in its crystalline state and has a silicon-silicon distance of $3\,\text{Å}$. For the carbon specimen there is a large area at $q \approx 0.2\,\text{Å}^{-1}$ and $\phi \approx 120°$. This is most likely due to the contrast transfer function which can be visible as rings in Fourier space. In the three particle structure factor, ring-like structures show at $q_3 = q$ which happens at an angle of $\phi = 120°$. Consequently, the high intensity area is in the right spot to be caused by the contrast transfer function.

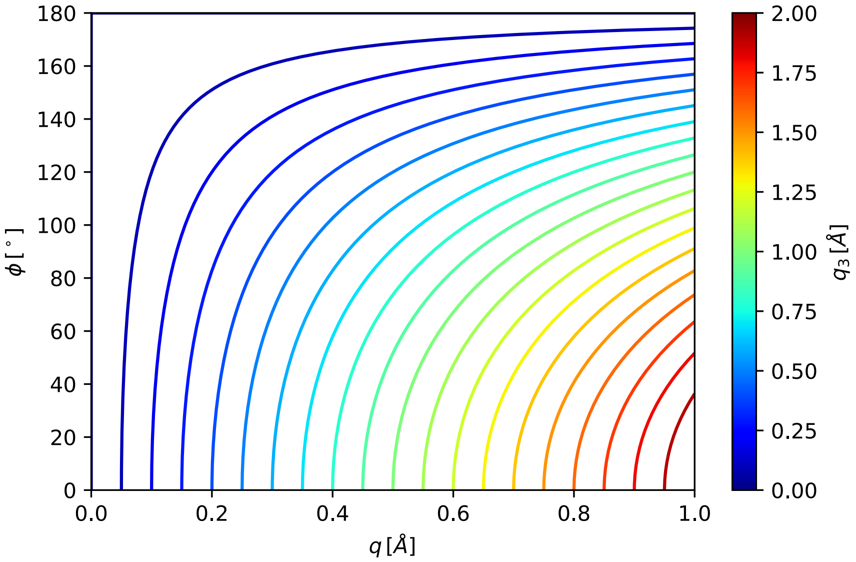

Figure 5.2: The contour lines of $q_3 = |\vec{q}_1 + \vec{q}_2|$ with $|\vec{q}_1| = |\vec{q}_2| = q$ and $\phi = \sphericalangle(\vec{q}_1, \vec{q}_2)$. In the lower right corner q_3 can become larger than the available reciprocal space in the image leading to undefined regions. Under some conditions these lines will also be visible in the three particle structure factor when the peaks are broad enough so that small variations of q and ϕ will not leave that peak.

This influence of the contrast transfer function is apparently not visible for silica. There is also a small peak but sharp peak at $q \approx 0.4\,\text{Å}^{-1}$ and $\phi \approx 120°$ stemming from the gold nano-cluster as will be shown in section 5.8.

In the second line the structure factors were normalized by their absolute values. The silica specimen shows the same two peaks for $q \approx 0.25\,\text{Å}^{-1}$ as in the image above. It also shows an additional cluster at $q \approx 0.45\,\text{Å}^{-1}$. For the carbon specimen the large peak disappeared since the influence of the contrast transfer function cancels out. The gold nano-cluster now shows additional peaks for $q \approx 0.4\,\text{Å}^{-1}$ at other angles. This hints at the possibility of the gold nano-cluster consisting of differently oriented crystals.

In the last line the structure factors are normalized by their radial averages. Apart from the three peaks that were already visible in the image of the silica specimen, the plot shows additional peaks at $0.55\,\text{Å}^{-1}$. The peaks at 60° and 120° are stronger but other peaks are also visible at intervals of 30°. This stems probably from the graphene substrate with its hexagonal structure. The small peaks in between hint at it consisting of two layers that are rotated by 30° with respect to each other. The carbon image shows more peaks for the gold cluster compared to the image that was normalized by the absolute value. There is also a small peak visible at 0.8 Å^{-1}. This comparison shows that, in general, one cannot neglect the contrast transfer function. It also indicates that the normalization by the radial average improves the signal-to-noise-ratio the most.

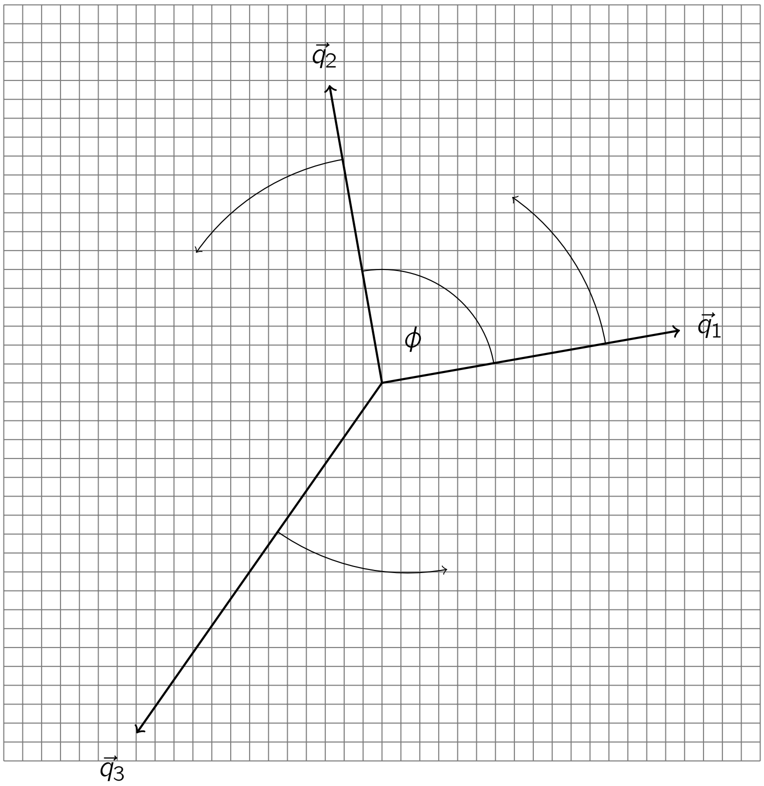

Figure 5.3: Representation of the averaging. The background lattice represents the pixels in Fourier transformed image. Given q and ϕ one gets a triple of reciprocal vectors $\vec{q}_1$, $\vec{q}_2$ and $\vec{q}_3$ that are rotated to get all positions where $\hat{S}$ is evaluated.

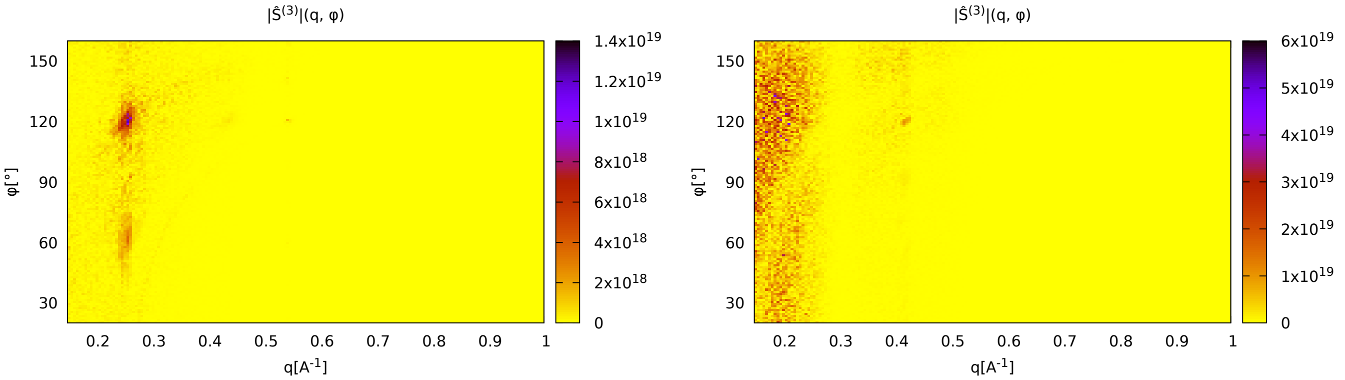

(a) Silica without normalization.

(b) Carbon without normalization.

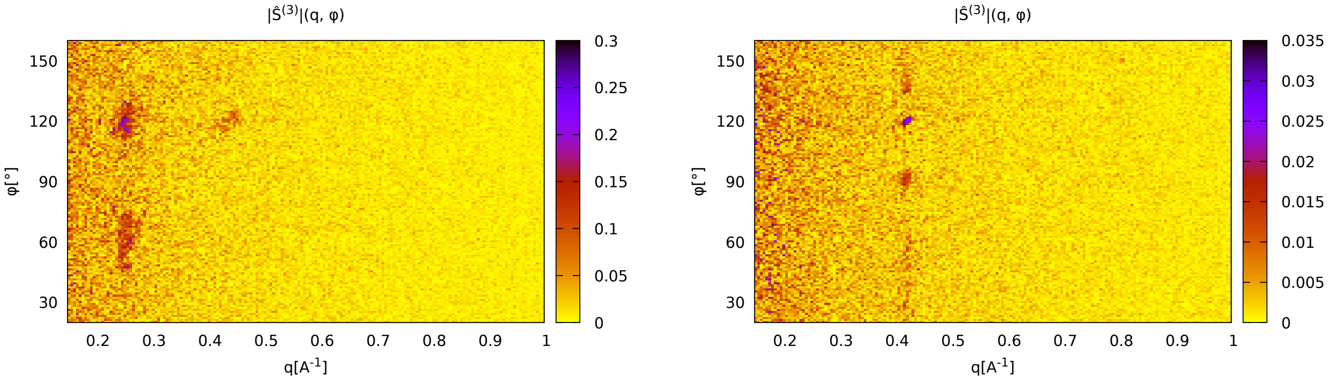

(c) Silica normalized by the absolute value.

(d) Carbon normalized by the absolute value.

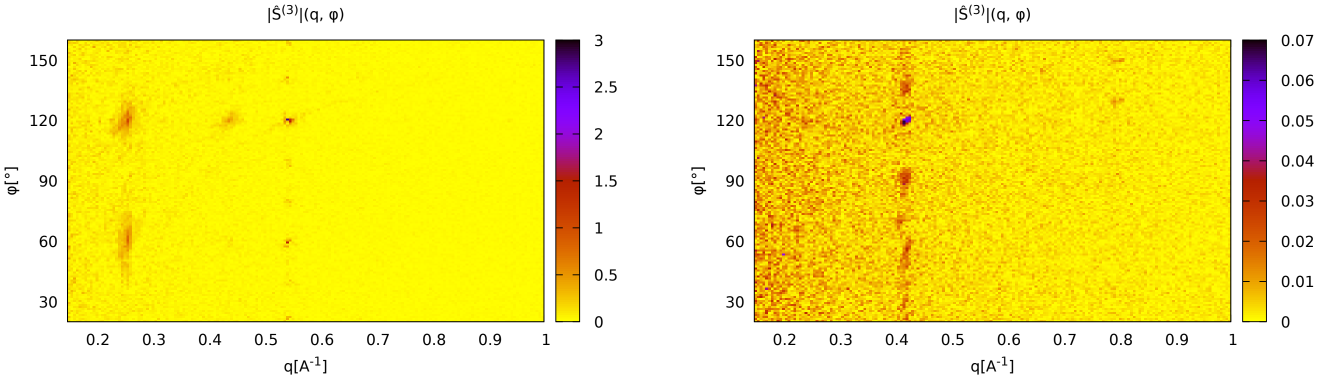

(e) Silica normalized by the average.

(f) Carbon normalized by the average.

Figure 5.4: Different normalization strategies compared for measurements of silica and carbon.

5.2 Three particle structure factor of a *n*-atomic group

In [Ham88] it was studied whether the three particle structure factor can be used to disambiguate different local structures by calculating S^3 for groups of 3 and 5 atoms with tetrahedral bond angle $\phi = 109.5°$. However it was not taken into account that it is not possible to obtain the structure factor when the phase contrast transfer function is not known or not equal to unity. The configurations are shown in fig. 5.5.

The calculation starts from the actual atom positions $\vec{r}_i$ and calculates the three particle structure factor directly without simulating a TEM image first. Since in an ideally amorphous object no orientation is special, one has to average over all possible orientations of the cluster which is achieved by rotating and integrating over all Euler angles [Fli14]. In the following this system is used to investigate the impact that the normalization has on the shape of the three particle structure factor.

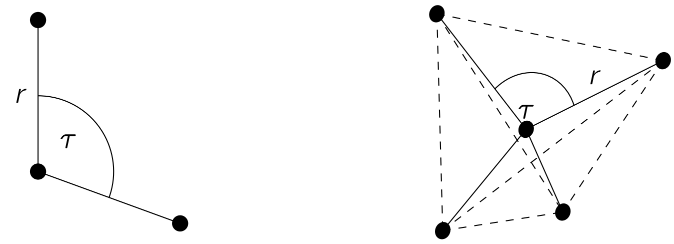

(a) 3 atoms with tetrahedral bond angle. **(b)** Tetrahedral

Figure 5.5: 2 local models of amorphous silicon with tetrahedral angle $\tau = 109.5°$. The dashed lines demonstrate how the atoms form a tetrahedral.

The results are shown in fig. 5.6 for the full structure factor and the normalized structure factor as defined in eq. (5.6). The normalized and non-normalized images look similar. However, the peaks seem to be more pronounced for the normalized images.

To simplify the comparison q was fixed at the value of the (111)-reflex of crystalline silicon, $q \approx 0.32\,\text{Å}^{-1}$. The result is shown in fig. 5.7. One sees that the qualitative features of the curves, such as the position of maxima and minima, are the same. However, the height and the shape of the peaks are slightly altered. This indicates that the proposed method should be able to obtain informations about the three particle structure factor.

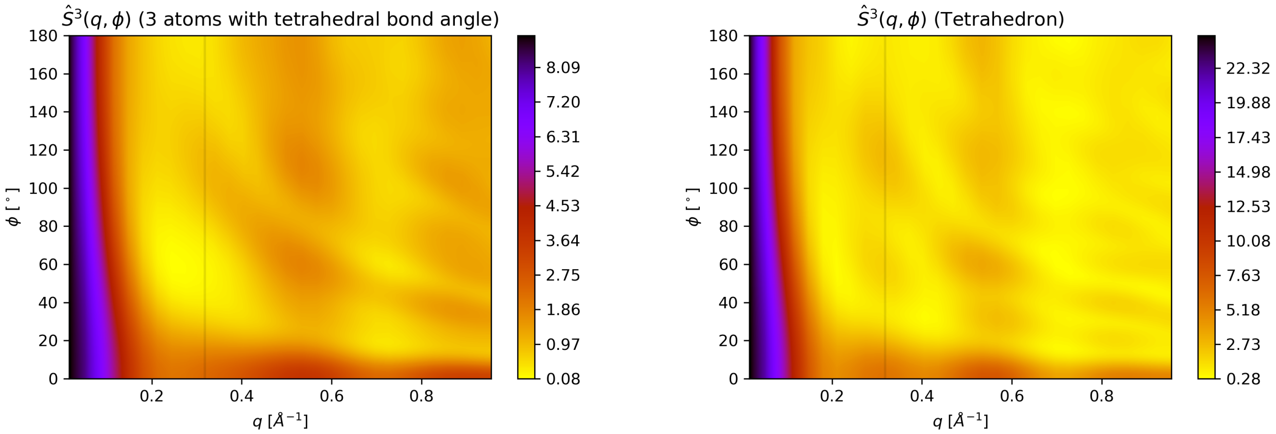

(a) Triangle structure without normalization

(b) Tetrahedron without normalization

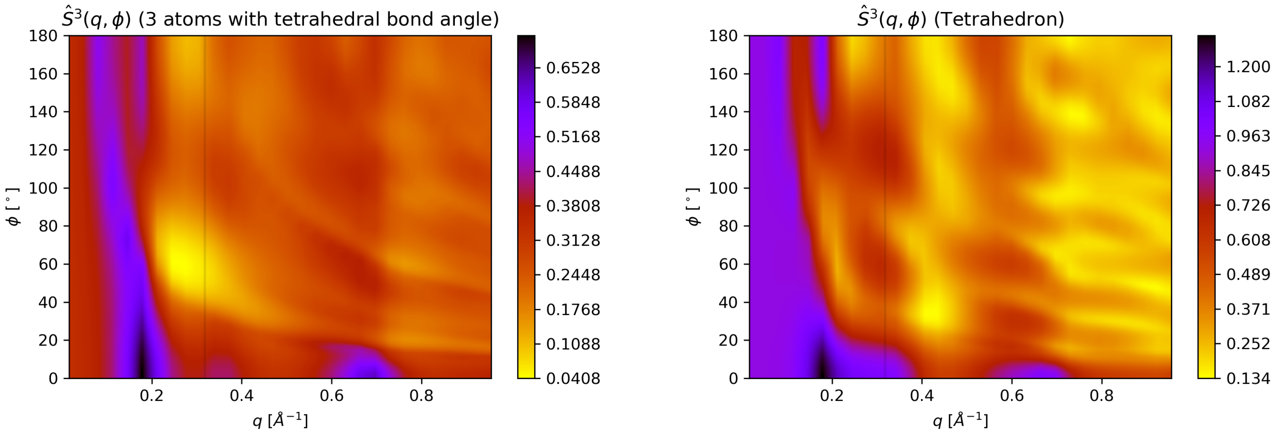

(c) Triangle normalized by the average

(d) Tetrahedron normalized by the average

Figure 5.6: Comparison of the impact of the normalization on the shape of the three particle structure factor. The gray vertical line at $q \approx 0.32\,\text{Å}^{-1}$ indicates the (111)-reflex of crystalline silicon shown as a line profile in figure 5.7.

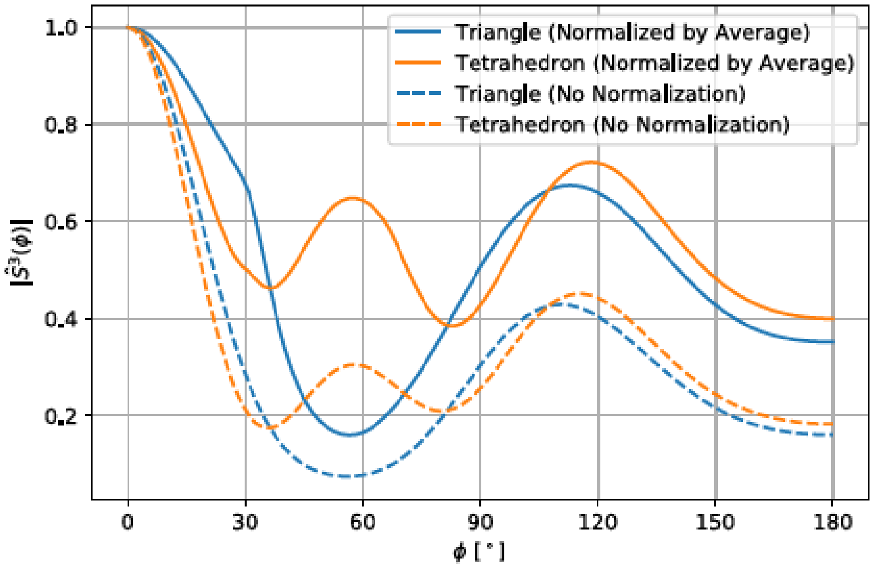

Figure 5.7: Line profiles through the three particle structure factors plotted in figure 5.6 at $q \approx 0.32\,\text{Å}^{-1}$. The three particle structure factors are normalized to $S^{(3)}(\phi = 0) = 1$ for better comparisons.

5.3 Ideal crystals

Since the proposed method is not able to obtain the full structure factor (see section 5.1) it is of interest to evaluate whether the information obtained from TEM images can be directly interpreted. In the following the three particle structure factors for various two-dimensional (hexagonal, cubic and penrose-tilling) structures are presented. For all models the atomic distance $d = 1.4\,\text{Å}$ of graphene was used. The parameters for the multislice simulation were also taken from graphene and otherwise ideal imaging was assumed since the purpose of this investigation is purely to determine the influence of the atomic structure and the influence of the microscope should be as small as possible.

5.3.1 Hexagonal

To investigate the impact of different lattice structures on the three particle structure factor, a crystalline graphene layer was simulated by placing carbon atoms in a hexagonal honeycomb lattice [NBN99] and running the multislice program from [Kir10] on it. The result is shown in figure 5.8. There are peaks at $q \approx 0.47\,\text{Å}^{-1}$ and $q \approx 0.81\,\text{Å}^{-1}$ that correspond to the distances $d_{100} = 2.13\,\text{Å}$ and $d_{110} = 1.23\,\text{Å}$, respectively. The peaks appear at the angles $\phi = 60°$ and $\phi = 120°$, as one would expect from a hexagonal lattice.

For simple hexagonal lattices the three particle structure factor is shown in figure 5.9.

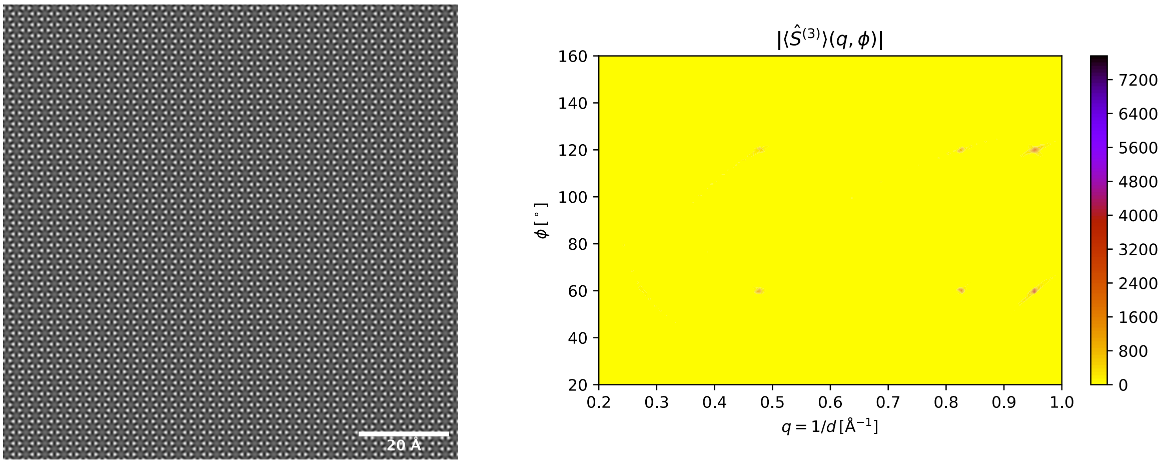

Figure 5.8: On the left a multislice simulation for a single sheet of graphene is shown. On the right is the corresponding three particle structure factor. 6 peaks are visible. Three of them are at 60° and 0.47 Å^{-1}, 0.81 Å^{-1} and 0.96 Å^{-1}. The other three peaks are at 120° and the same q-values.

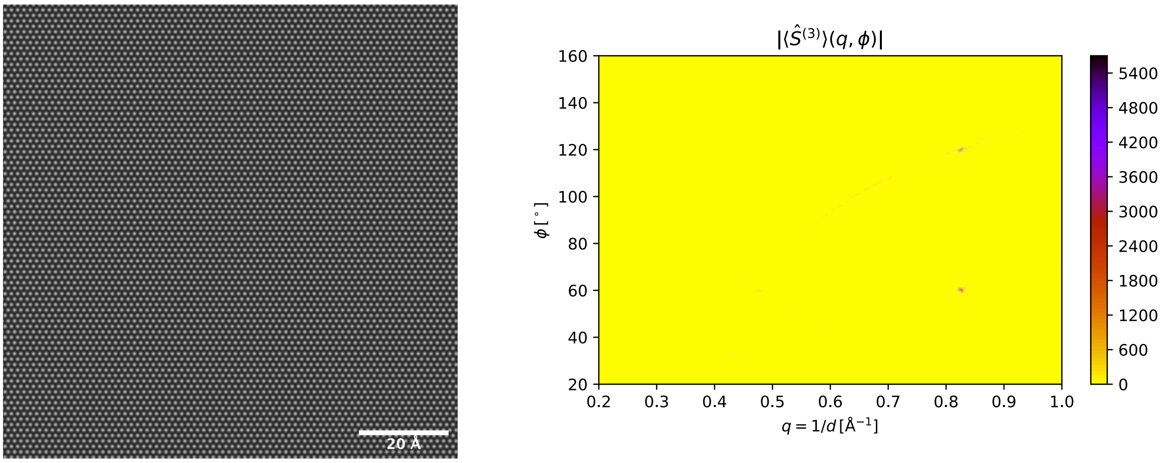

Figure 5.9: On the left, a multislice simulation for a hexagonal lattice is shown. On the right is the corresponding three particle structure factor. Two peaks are visible for $q = 0.81\,\text{Å}^{-1}$ at 60° and 120°.

Compared to the honeycomb lattice, this hexagonal lattice has fewer peaks since the number of possible distances is limited compared to the honeycomb case. As expected, the peaks appear at the angles $\phi = 60°$ and $\phi = 120°$.

5.3.2 Cubic

The three particle structure factor of a simple cubic lattice is shown in figure 5.10. It shows only a single peak at $q \approx 0.71\,\text{Å}^{-1}$ which is the inverse of the atomic distance. The peak appears at $\phi = 90°$ which is expected for a cubic lattice.

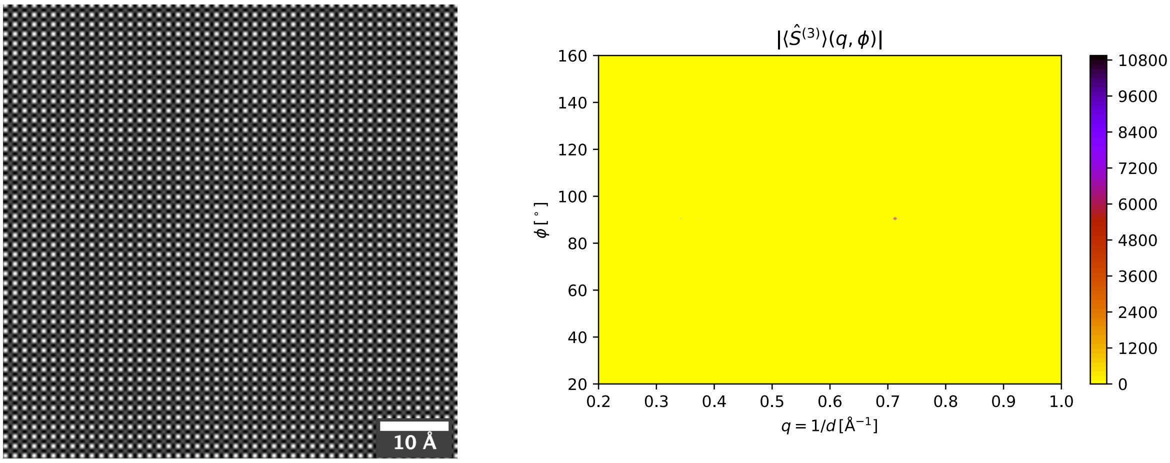

Figure 5.10: On the left, a multislice simulation for a copy crystal with next-neighbour distances of $d = 1.4\,\text{Å}$ is shown. On the right is the corresponding three particle structure factor. One Peak is visible at 90° and $0.71\,\text{Å}^{-1}$.

5.3.3 Quasicrystals

Quasicrystals are a special kind of crystal that is ordered but not periodic [Mac82]. They do not have any translational symmetry but due to their rotational symmetry show sharp peaks in diffraction patterns. One famous example is the Penrose tiling [Pen74]. In figure 5.11, a Penrose tiling is shown. A TEM image was simulated by placing atoms at the intersections of the Penrose tiling and using the multislice code from [Kir10] on it. This is shown in figure 5.12. The three particle structure factor in figure 5.13. It shows a large number of peaks. This stems from the fact that there is no translational symmetry. The peaks appear mostly at angles that are multiples of 36° hinting at a tenfold symmetry as is characteristic for quasicrystals.

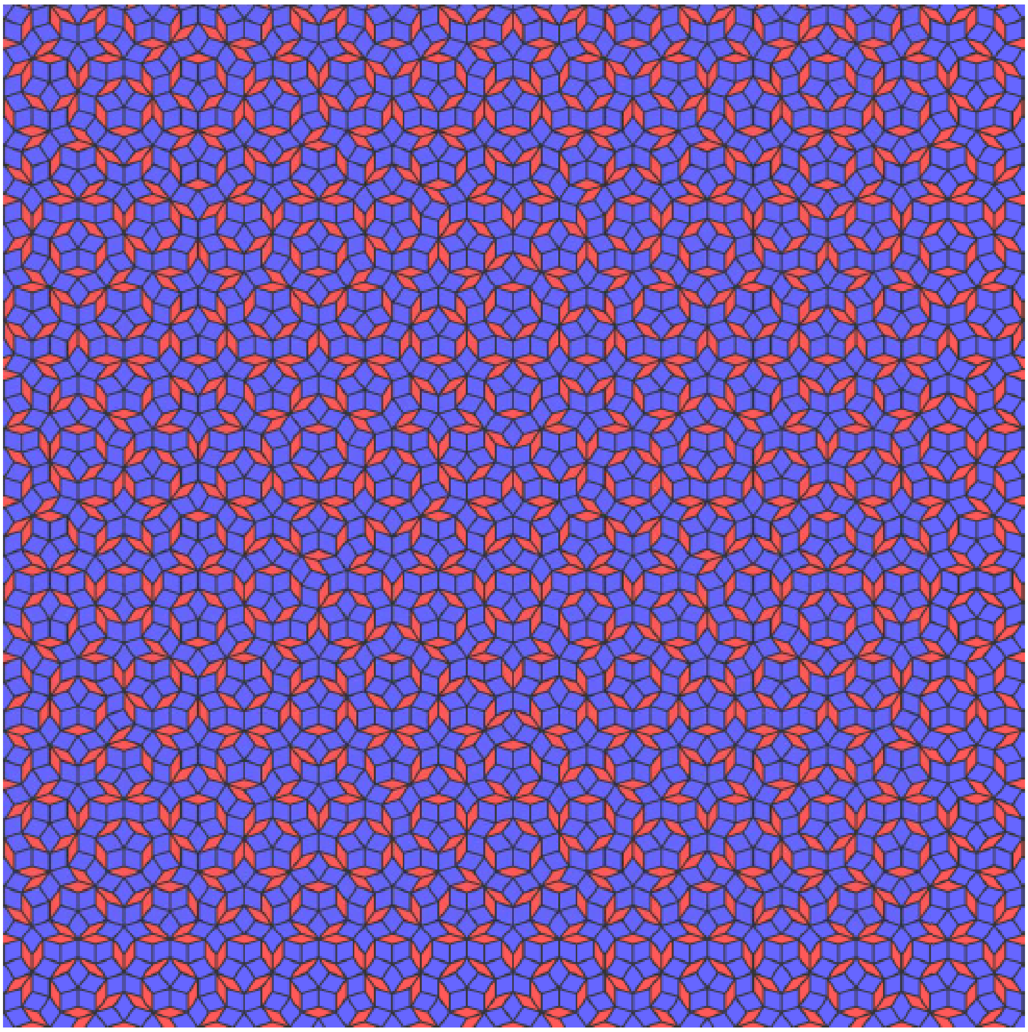

Figure 5.11: A Penrose tiling as generated by the code from [Pre11].

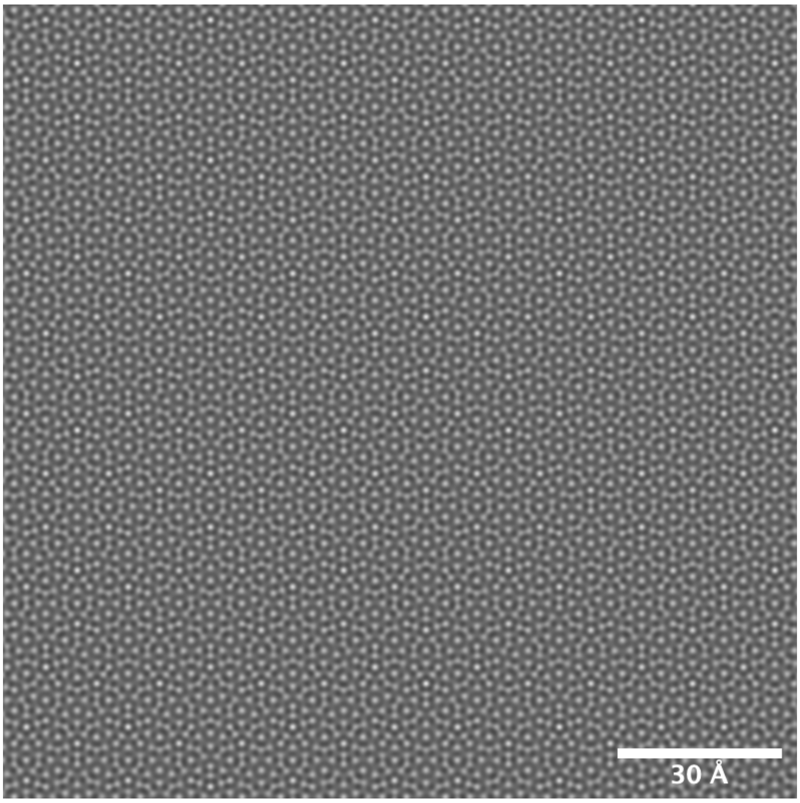

Figure 5.12: TEM image of a quasicrystal simulated using the multislice method.

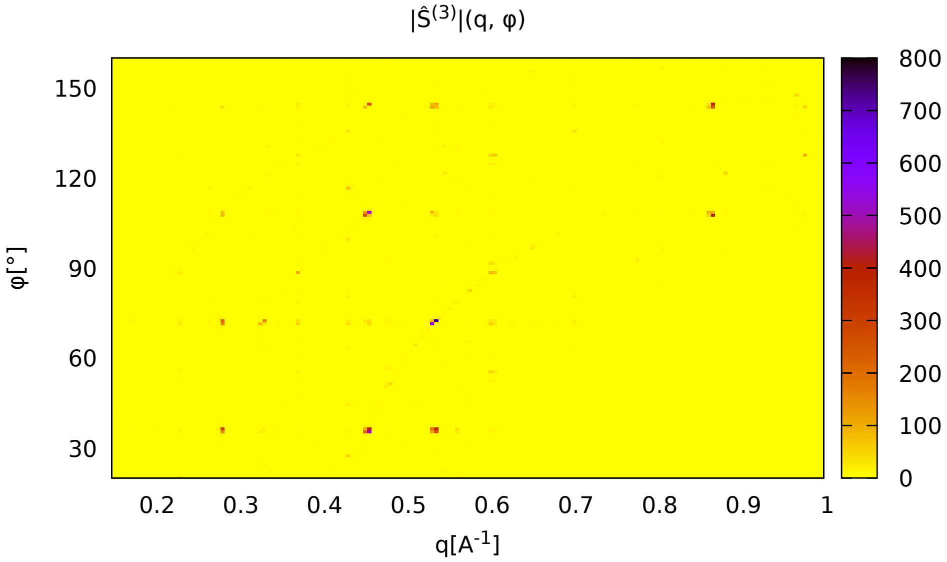

Figure 5.13: The three particle structure factor obtained from a simulated image of a Penrose tiling as an example of a quasicrystal.

5.4 Crystalline Plates

The plates model, as discussed in section 4.2, was simulated for plate sizes $l = 1$ to $l = 4$. One simulated example of the plates model is shown in figure 5.14. The three particle structure factors are shown in figure 5.15. The figures show that the three particle structure factor develops larger peaks when the crystalline areas are larger. Since the plates are partly stacked on top of each other there are also other bond angles and lengths present in the image leading to horizontal and vertical lines. The diagonal lines stem most likely from the contour lines of q_3, as discussed in section 5.1.1. In figure 5.15a there two weak peaks for $\phi = 120°$ at $q \approx 0.45\,\text{Å}^{-1}$ and $q \approx 0.8\,\text{Å}^{-1}$ and one peak at $\phi \approx 60°$ and $q \approx 0.45\,\text{Å}^{-1}$ which is much broader along the ϕ-axis. The position of the peaks matches those of crystalline carbon. As the plate site increases in the following images the peaks get more pronounced. There is also a sharp edge at $q \approx 0.6\,\text{Å}^{-1}$ for small angles and a small peak at $\phi \approx 150°$ and $q \approx 0.9\,\text{Å}^{-1}$ that are currently not interpretable. These are most likely artefacts resulting from the rather simple model.

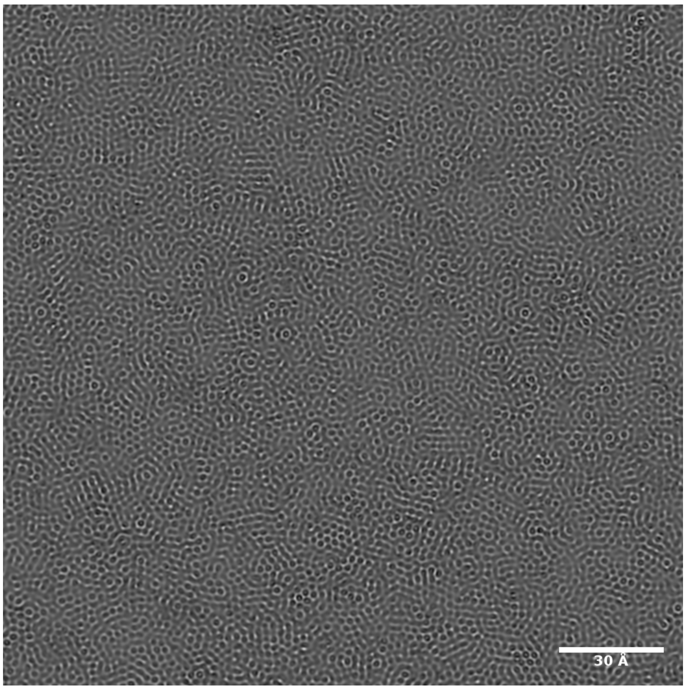

Figure 5.14: Simulated TEM image of the plates model with $l = 3$. The multislice simulation was performed with the code from [Kir10].

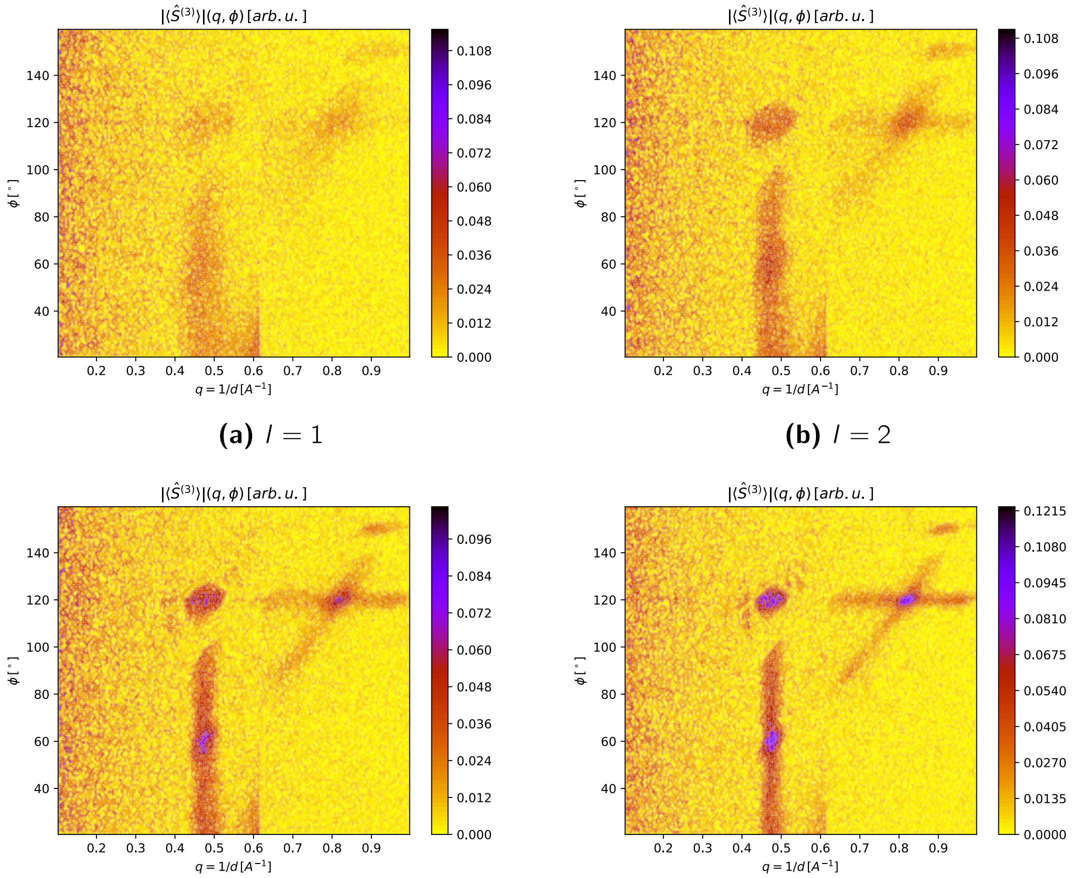

(a) $l = 1$

(b) $l = 2$

(c) $l = 3$

(d) $l = 4$

Figure 5.15: The three particle structure factor for different plate radii.

5.5 Amorphous Layers

In order to show the dependence of the $S^{(3)}$ signal-to-noise ratio on the thickness of the specimen, 20 layers of amorphous twodimensional carbon were simulated as CRNs. They were rotated by a random angle and then put on top of each other. This is shown in figure 5.16.

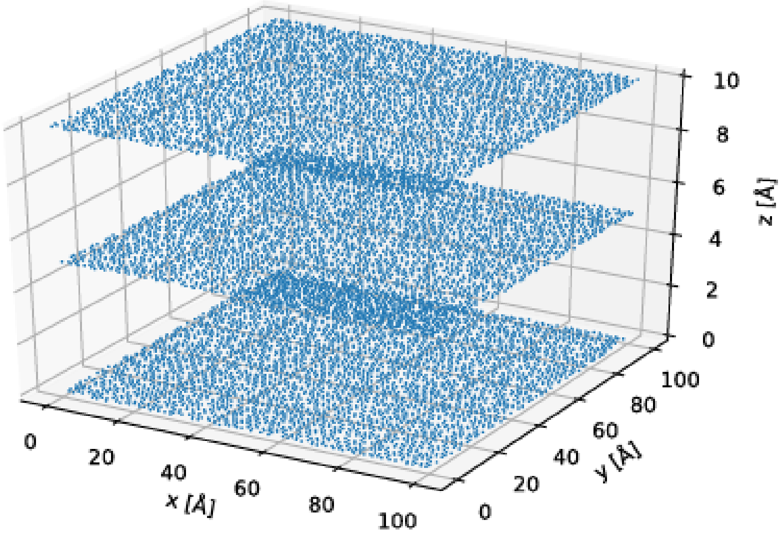

Figure 5.16: Different amorphous layers stacked on top of each other to model the influence of thickness. Here, three layers are shown.

The figures 5.17 to 5.24 show how the signal vanishes as the thickness increases even though each layer itself would produce the same $S^{(3)}$. For up to three layers most peaks are still visible. For six layers almost no structure is visible anymore. Comparing the result for 20 layers to figure 5.25 shows that the three particle structure factor becomes indistinguishable from white noise.

To quantify the decrease of the signal with the number of layers, the first layer was replaced by a crystalline graphene sheet. Figure 5.26 shows how after a few layers the height of the crystalline peaks shrinks by several orders of magnitude. Interestingly, the order of the peaks in terms of height changes as more amorphous layers are added. This height loss is not accompanied by a broadening of the peaks as figure 5.27 shows. However, it does not make a difference whether the crystalline layer is in the first or last position.

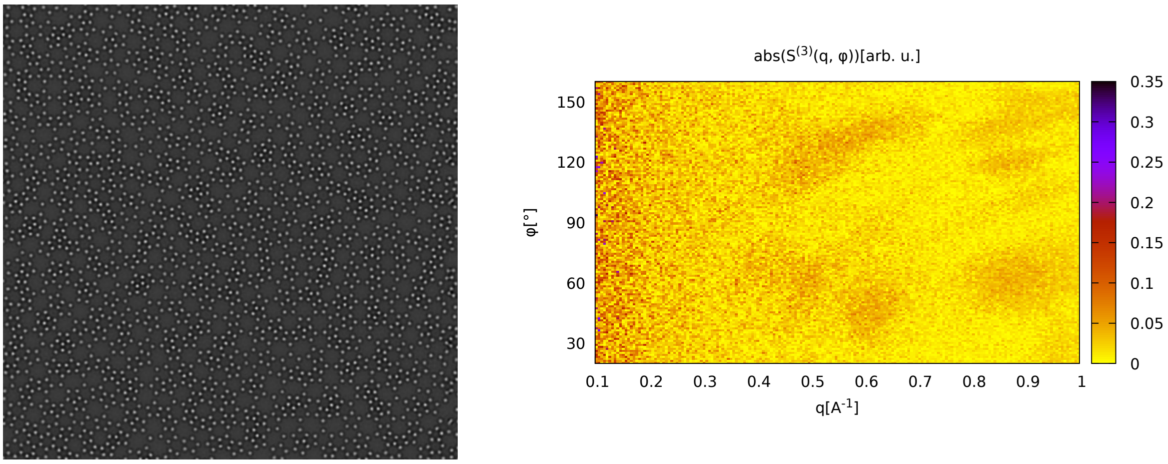

Figure 5.17: Multislice simulation of 1 layer of amorphous graphene.

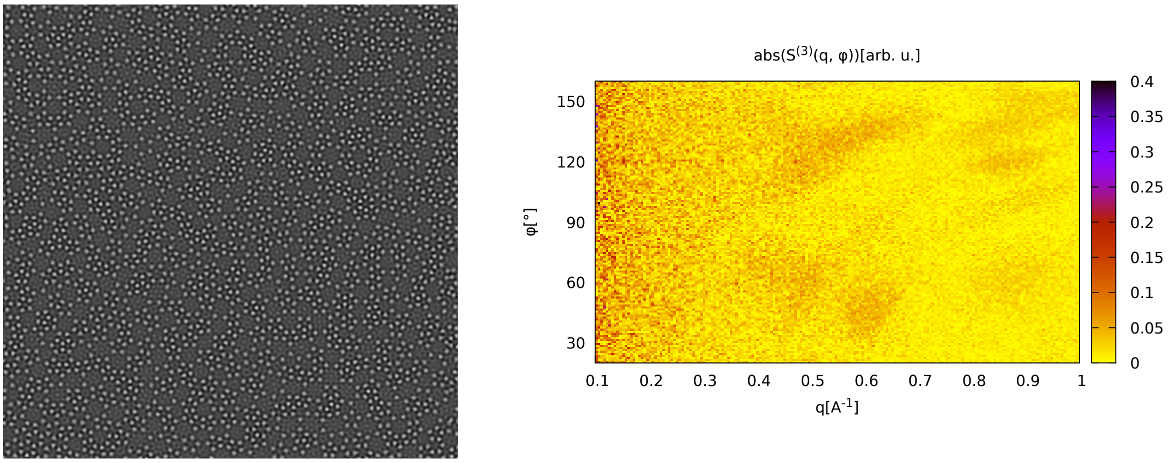

Figure 5.18: Multislice simulation of 2 layers of amorphous graphene.

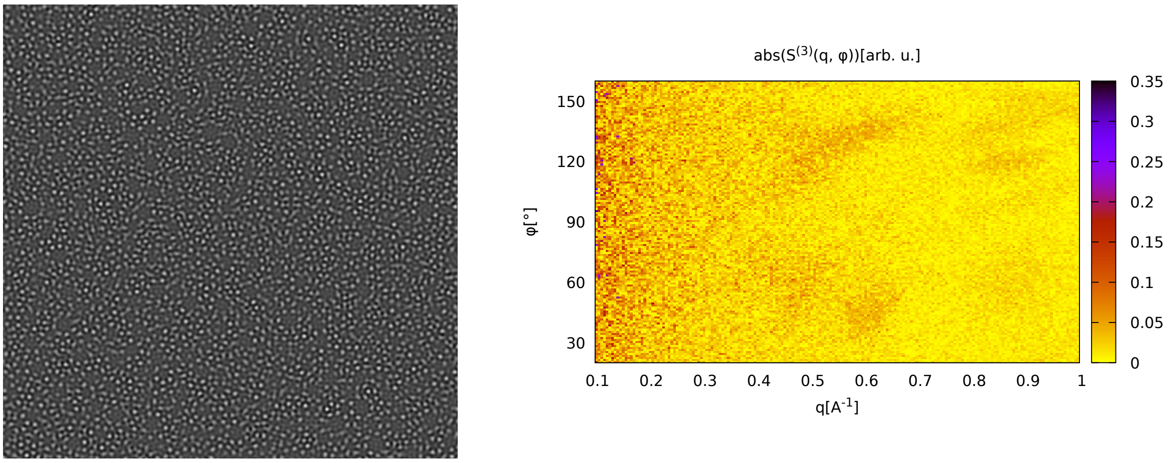

Figure 5.19: Multislice simulation of 3 layers of amorphous graphene.

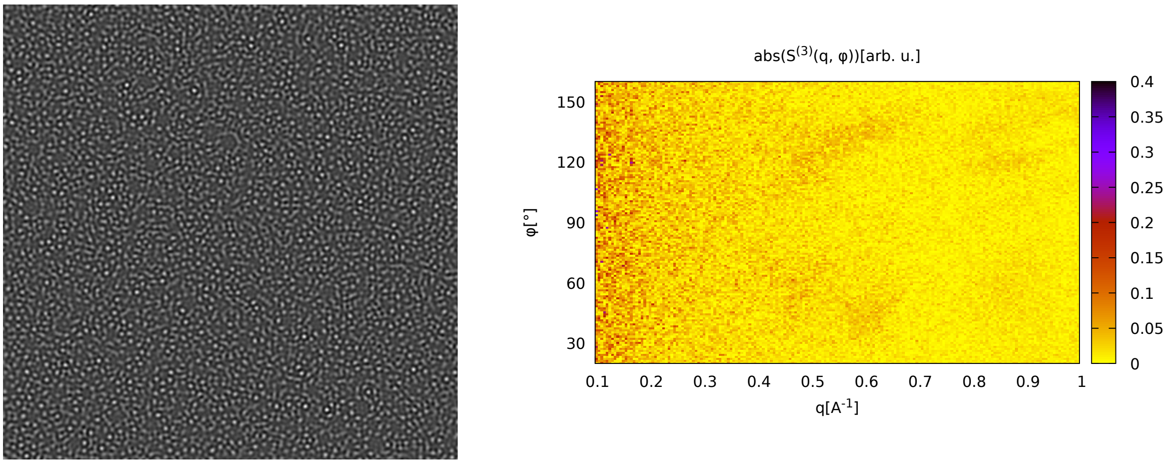

Figure 5.20: Multislice simulation of 4 layers of amorphous graphene.

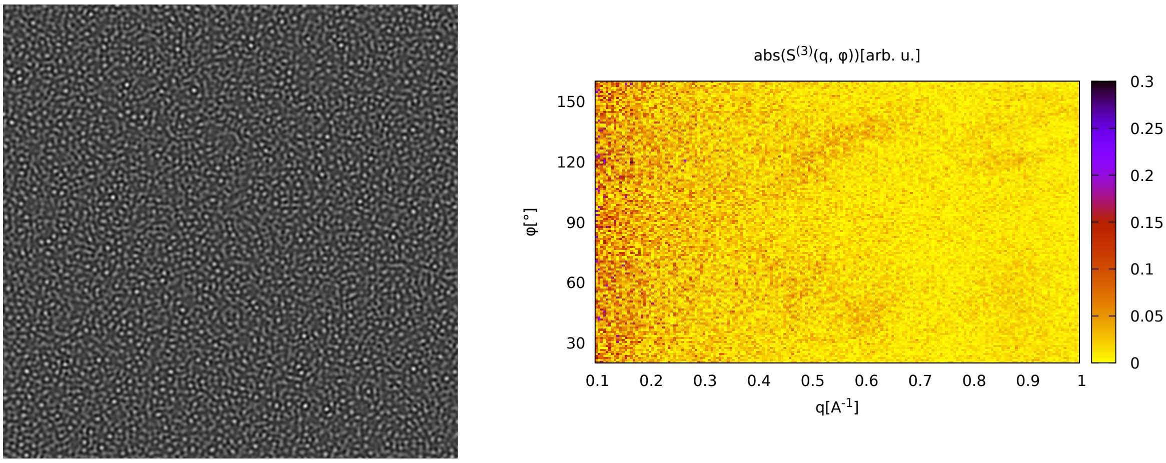

Figure 5.21: Multislice simulation of 5 layers of amorphous graphene.

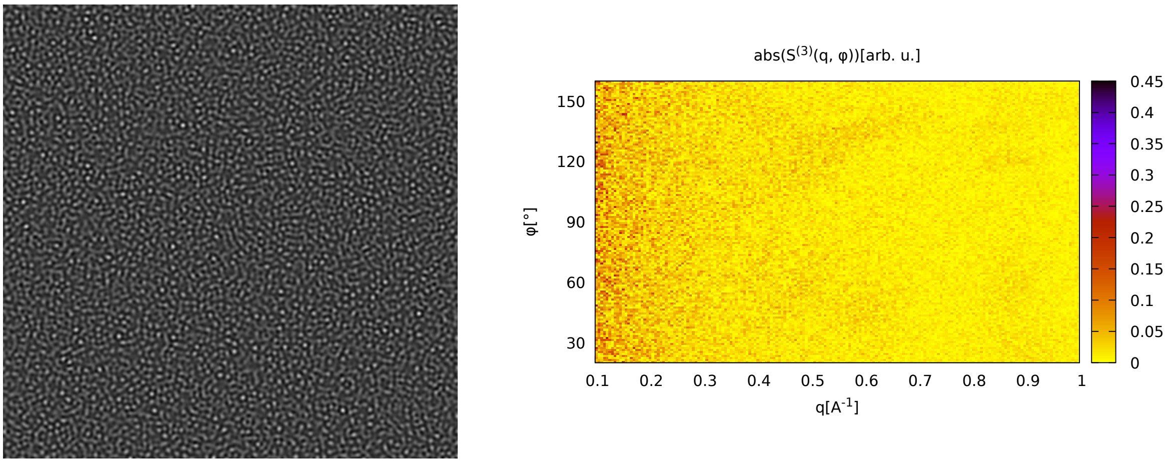

Figure 5.22: Multislice simulation of 6 layers of amorphous graphene.

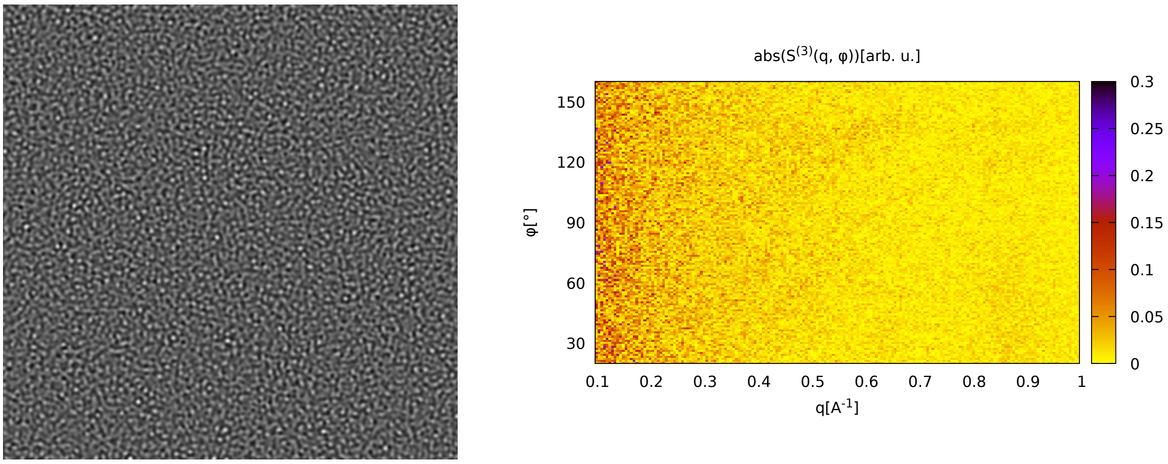

Figure 5.23: Multislice simulation of 10 layers of amorphous graphene.

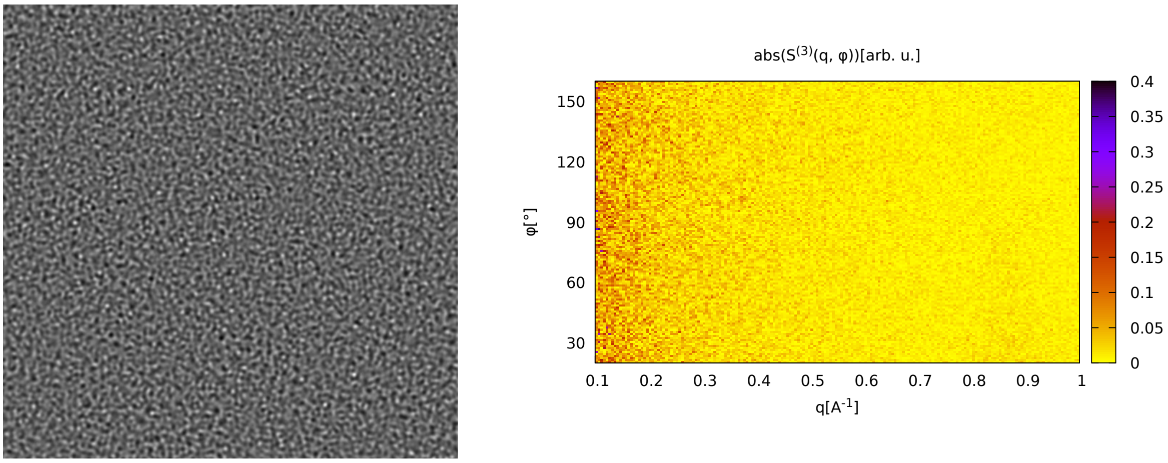

Figure 5.24: Multislice simulation of 20 layers of amorphous graphene.

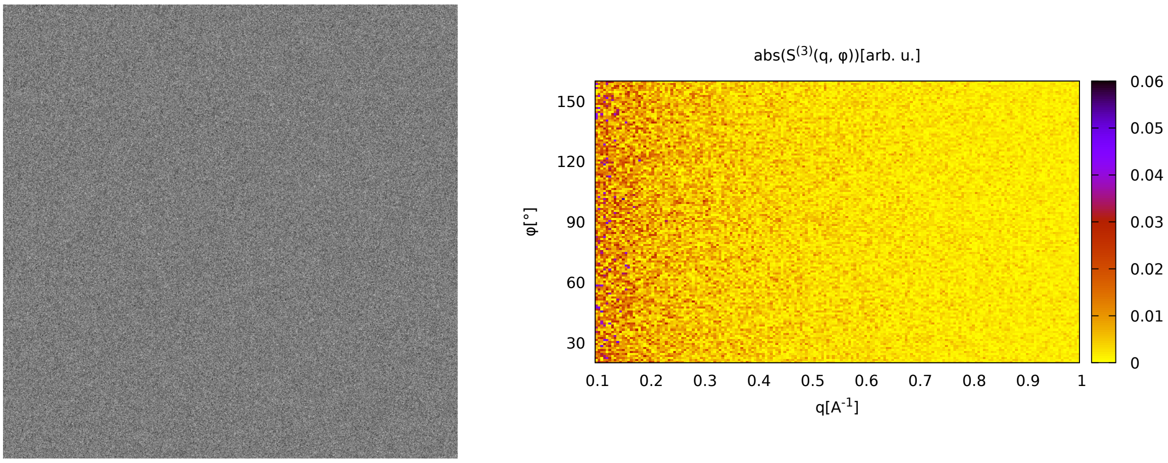

Figure 5.25: An image consisting of white noise and its three particle structure factor.

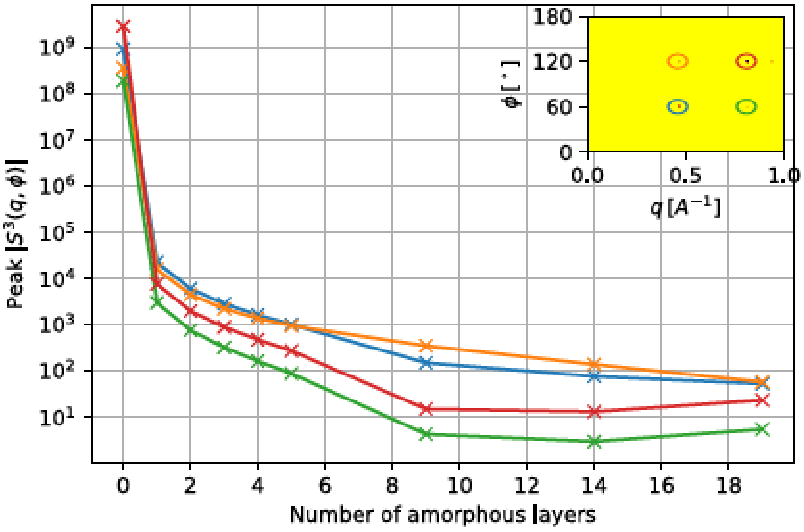

Figure 5.26: Dependence of the peak height of a crystalline graphene layer on the number of amorphous layers on top of it. Note that the y-axis is plottet logarithmically.

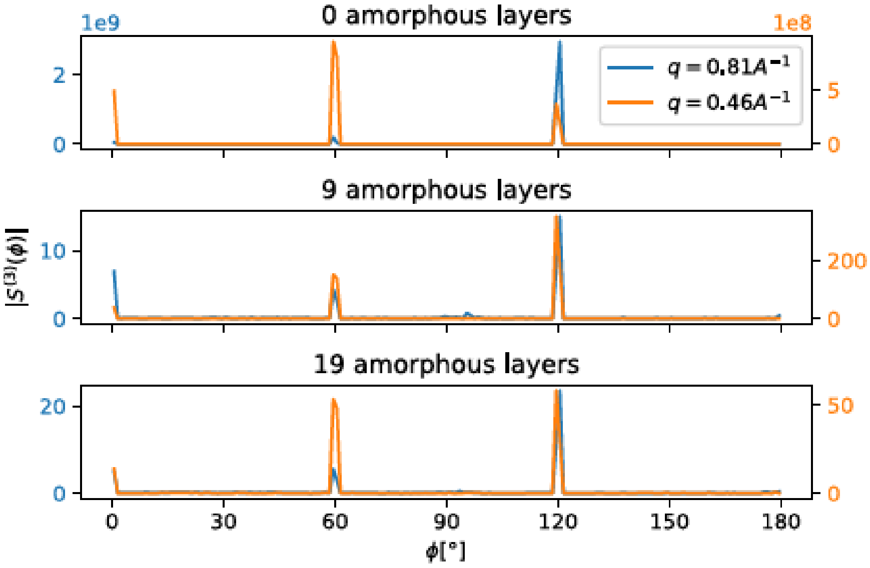

Figure 5.27: Dependence of the peak shapes of a crystalline graphene layer on the number of amorphous layers on top of it.

5.6 Interaction Potentials in Molecular Dynamics Simulations

In the following, the Liquid Quenching method (see section 4.4) was used with the Tersoff 1994 potential [Ter94], the second generation Reactive Empirical Bond-Order potential (REBO-II) [Bre+02] and the first generation Long-range Carbon Bond-Order potential (LCBOP-I) [LF03] to generate amorphous carbon. For the simulation, the software LAMMPS [Pli93] was used. In the following, the same densities $\rho = 1.5\,\text{g/cm}^3$ and $\rho = 3.0\,\text{g/cm}^3$ are used as in [TSM16].

In [TSM16] the resulting structures were directly compared by calculating observables like the ring statistics or the radial distribution function directly from the particle position. In the following those particle position will be used in multislice simulations to calculate the three particle structure factor as would be done in an experimental setting.

5.6.1 Pair distribution functions

Before comparing the three particle structure factors for the simulated structures, figures 5.28 and 5.29 show the radial distribution functions for those structures to highlight the information gained by using three particle structure factors. For $\rho = 1.5\,\text{g/cm}^3$ there is no qualitative difference between the structured. In contrast, for $\rho = 3.0\,\text{g/cm}^3$ the structure simulated with the REBO-II potential exhibits only three peaks while the other two structures show four peaks.

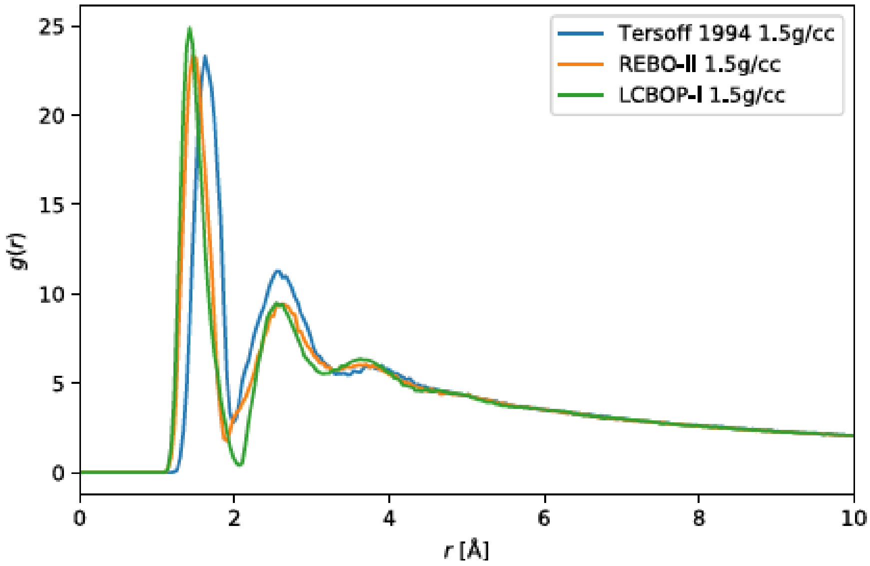

Figure 5.28: Comparison of the pair distribution functions for $\rho = 1.5\,\text{g/cm}^3$.

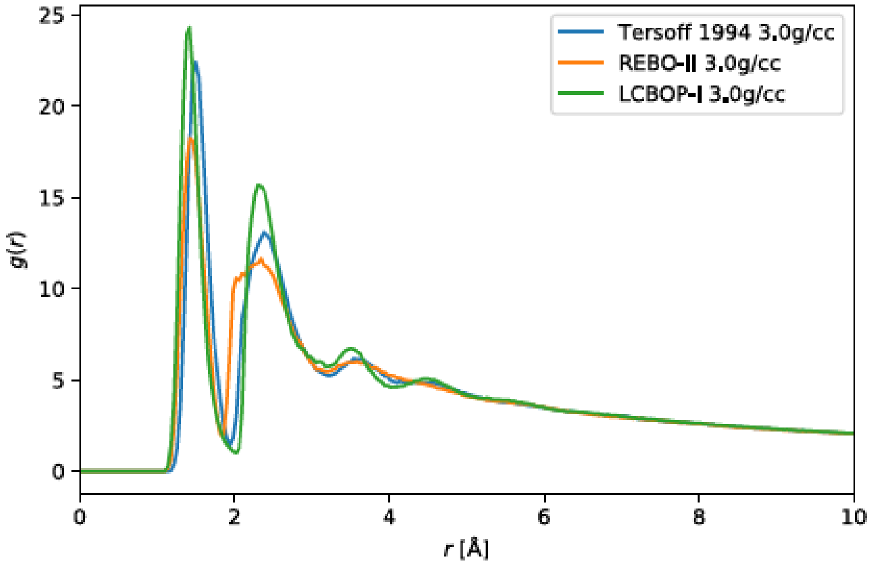

Figure 5.29: Comparison of the pair distribution functions for $\rho = 3.0\,\mathrm{g/cm^3}$.

5.6.2 Density $\rho = 1.5\,\mathrm{g/cm^3}$

For $\rho = 1.5\,\mathrm{g/cm^3}$, the results are shown in the figures 5.30-5.32. Judging from the the simulated TEM images, the Tersoff potential produces regularly spread out structures while the other two potentials tend to produce long chains of carbon atoms. This is also reflected in the three particle structure factor where the Tersoff potential produces peaks at the same places one would expect from hexagonal carbon while the other two potentials don't show any apparent structures. However, the radial distribution function in figure 5.28 was not able to show this qualitative difference between these structures.

5.6.3 Density $\rho = 3.0\,\mathrm{g/cm^3}$

For $\rho = 3.0\,\mathrm{g/cm^3}$ the results are shown in the figures 5.33-5.35. Looking at the simulated TEM images, there are no apparent differences regarding the structure of the specimens. However, the three particle structure factor for the Tersoff and for the LCBOP-I potential show a single peak at 90° hinting that these structures weren't able to diverge from the cubic initial condition. The REBO-II potential show one peak for $q \approx 0.55\,\text{Å}^{-1}$ and $\phi \approx 70°$ whose origin is not clear. These difference were not visible in the radial distribution functions in figure 5.29.

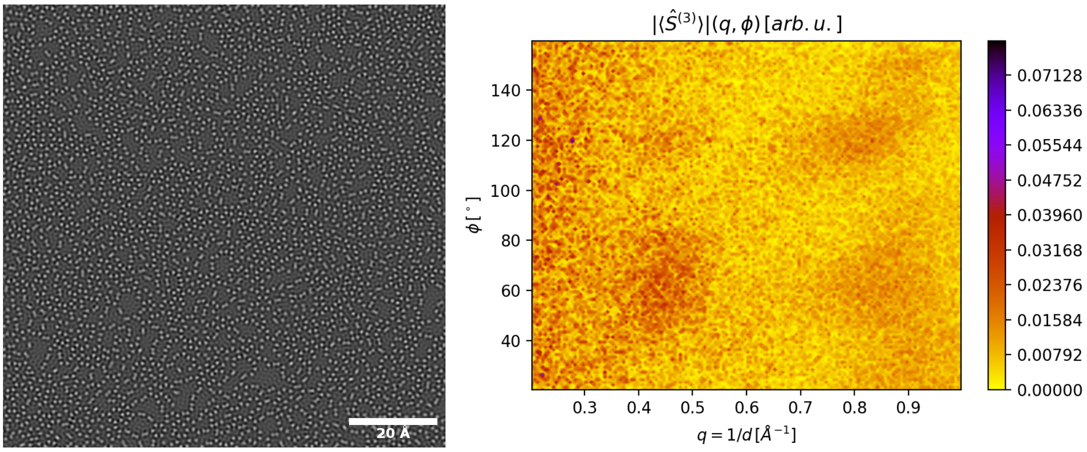

(a) **(b)**

Figure 5.30: In (a) a carbon layer is shown that was simulated using the liquid quenching method for the Tersoff potential with a density $\rho = 1.5\,\mathrm{g/cm^3}$. (b) shows the corresponding three particle structure factor.

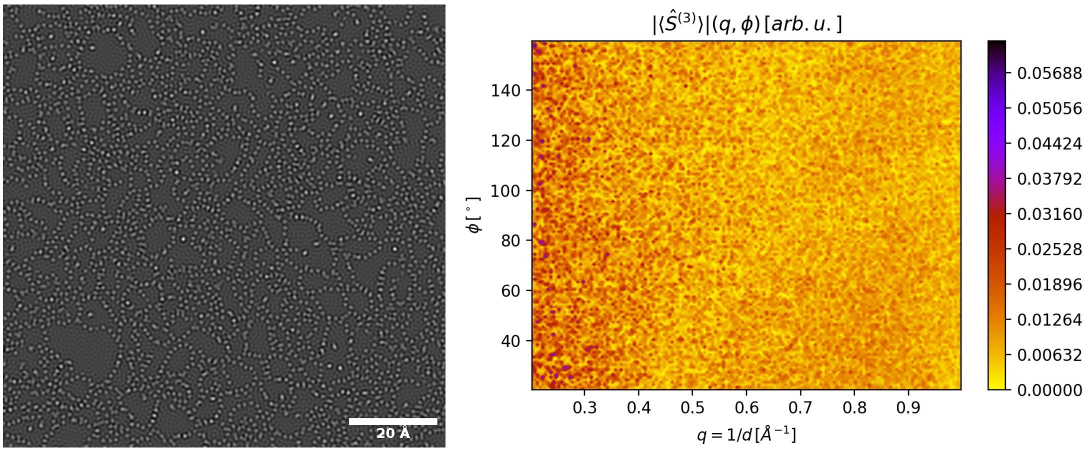

(a) **(b)**

Figure 5.31: In (a) a carbon layer is shown that was simulated using the liquid quenching method for the REBO-II potential with a density $\rho = 1.5\,\mathrm{g/cm^3}$. (b) shows the corresponding three particle structure factor.

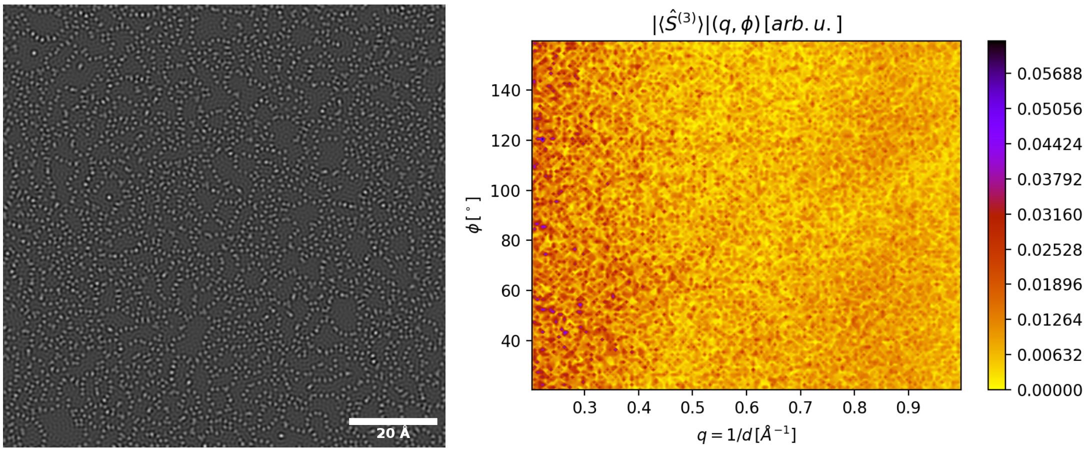

(a) **(b)**

Figure 5.32: In (a) a carbon layer is shown that was simulated using the liquid quenching method for the LCBOP-I potential with a density $\rho = 1.5\,\mathrm{g/cm^3}$. (b) shows the corresponding three particle structure factor.

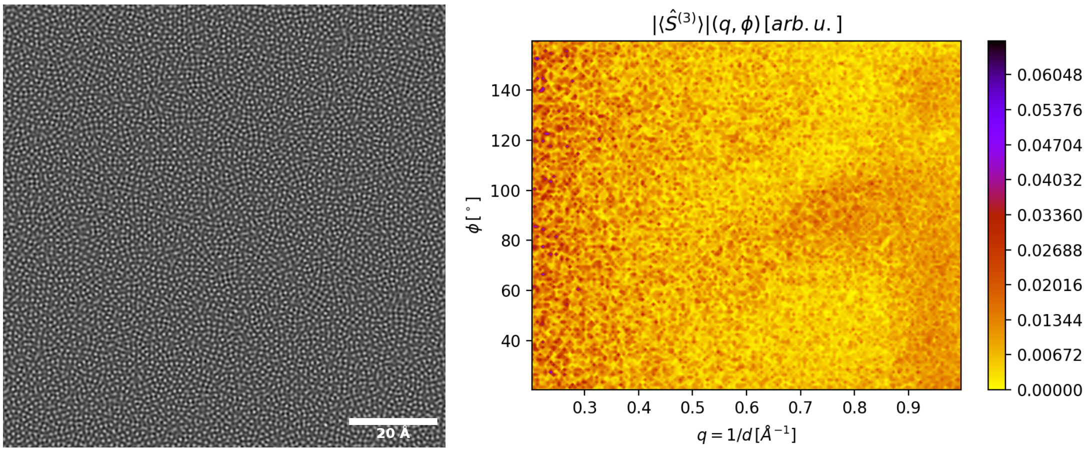

(a) **(b)**

Figure 5.33: In (a), a carbon layer is shown that was simulated using the liquid quenching method for the Tersoff potential with a density $\rho = 3.0\,\mathrm{g/cm^3}$. (b) shows the corresponding three particle structure factor.

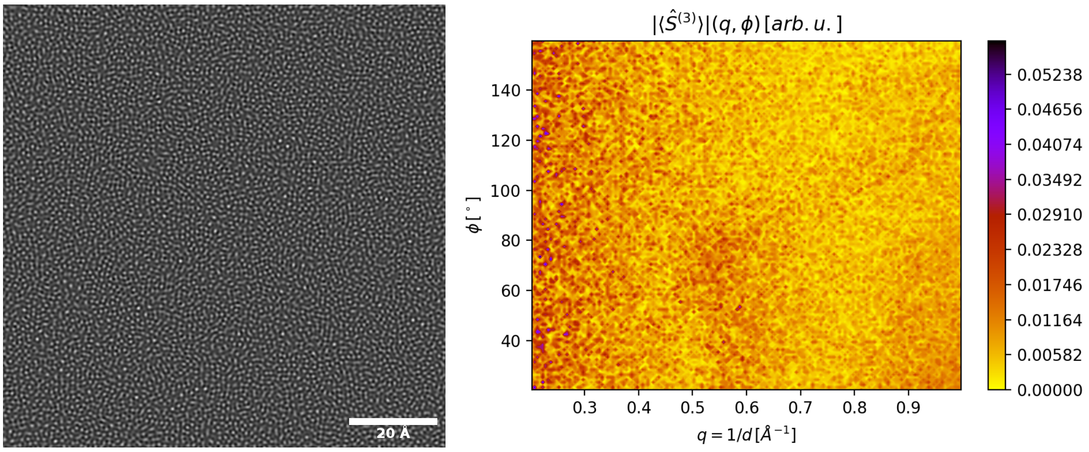

(a) **(b)**

Figure 5.34: In (a), a carbon layer is shown that was simulated using the liquid quenching method for the REBO-II potential with a density $\rho = 3.0\,\mathrm{g/cm^3}$. (b) shows the corresponding three particle structure factor.

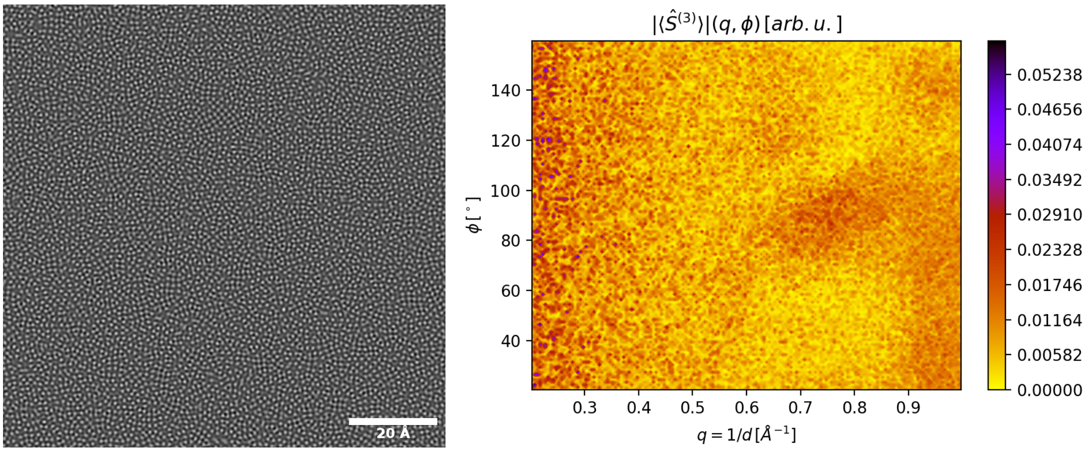

(a) **(b)**

Figure 5.35: In (a) a carbon layer is shown that was simulated using the liquid quenching method for the LCBOP-I potential with a density $\rho = 3.0\,\mathrm{g/cm^3}$. (b) shows the corresponding three particle structure factor.

5.6.4 Dependence on thickness

For the Tersoff potential, the simulation was repeated with larger thicknesses. For $\rho = 1.5\,\mathrm{g/cm^3}$, the results are shown in figure 5.36 and for $\rho = 3.0\,\mathrm{g/cm^3}$ in figure 5.37. For both densities the structures that are visible at $\Delta z = 4\,\text{Å}$ disappear at higher thickness.

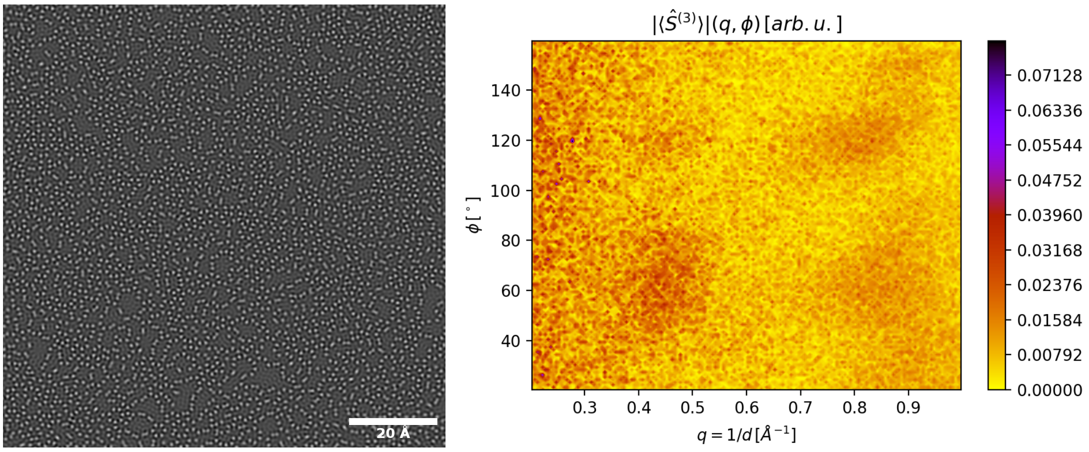

(a) $\Delta z = 4\,\text{Å}$ **(b)** $\Delta z = 4\,\text{Å}$

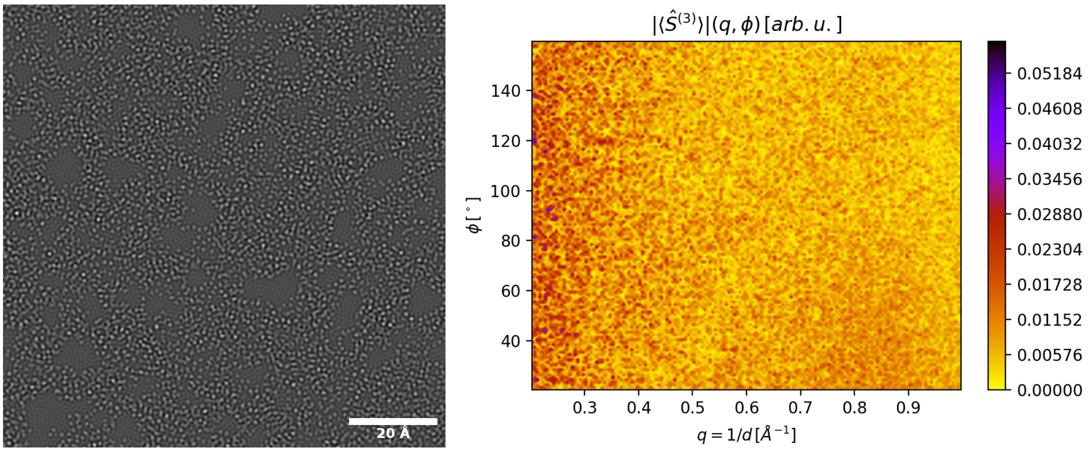

(c) $\Delta z = 10\,\text{Å}$ **(d)** $\Delta z = 10\,\text{Å}$

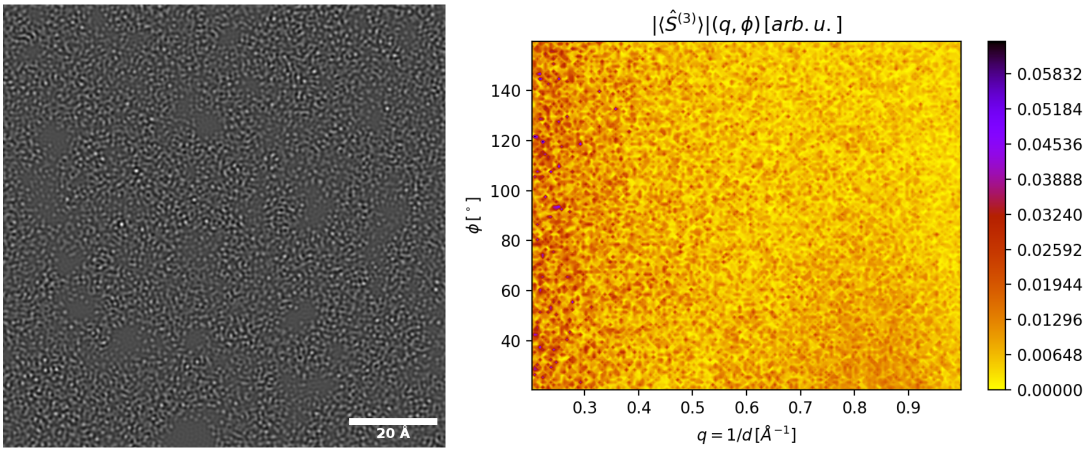

(e) $\Delta z = 20\,\text{Å}$ **(f)** $\Delta z = 20\,\text{Å}$

Figure 5.36: Carbon specimens were simulated with different thickness and with a density $\rho = 1.5\,\text{g/cm}^3$.

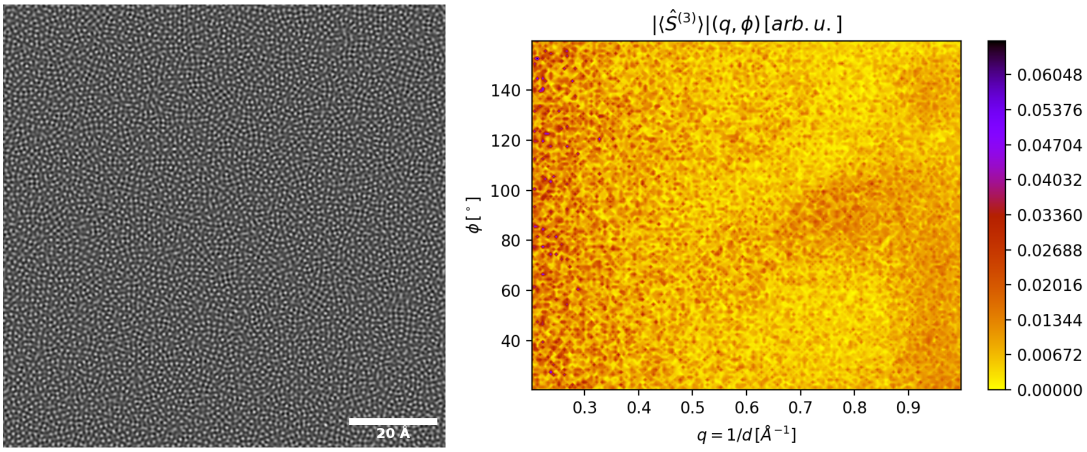

(a) $\Delta z = 4\,Å$ **(b)** $\Delta z = 4\,Å$

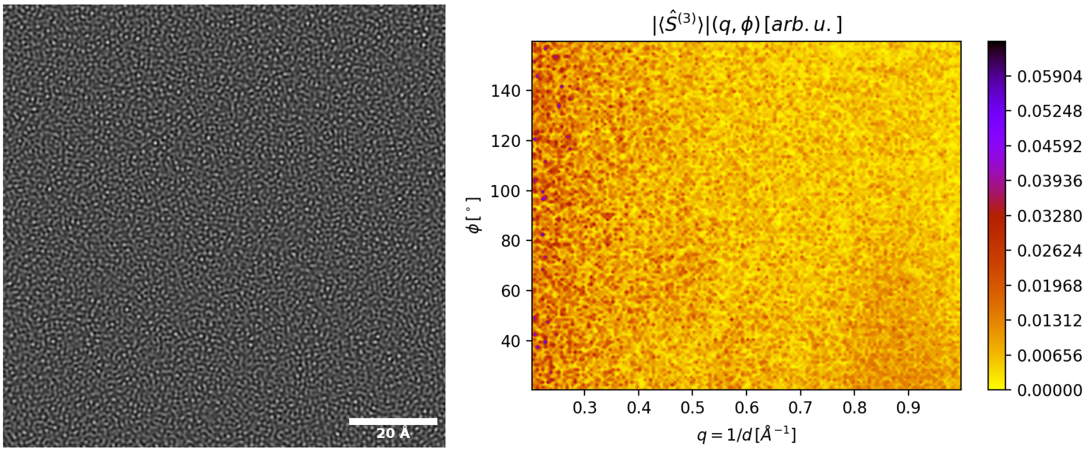

(c) $\Delta z = 10\,Å$ **(d)** $\Delta z = 10\,Å$

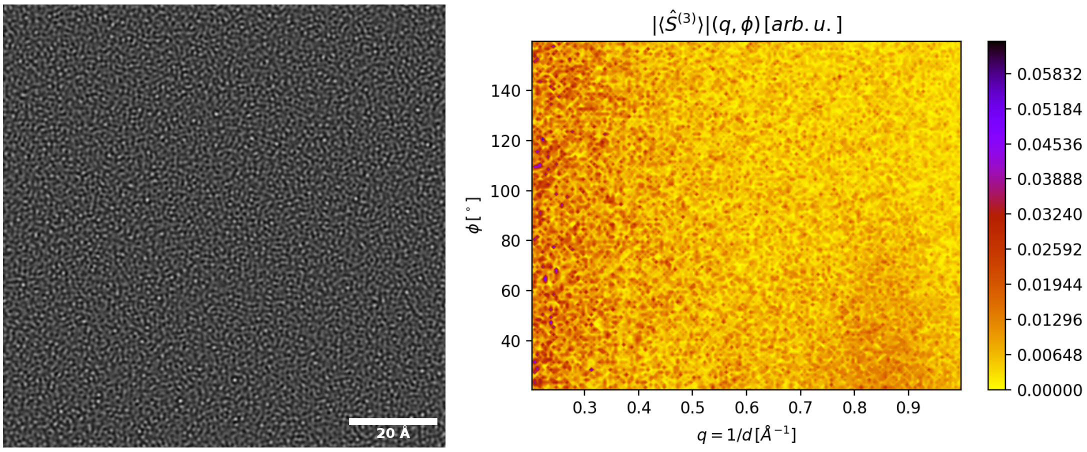

(e) $\Delta z = 20\,Å$ **(f)** $\Delta z = 20\,Å$

Figure 5.37: Carbon specimens were simulated with different thickness and with a density $\rho = 3.0\,\mathrm{g/cm^3}$.

5.7 Amorphous Silica

Figure 5.38 shows the three particle structure factor of two-dimensional amorphous silica that was placed on top of a graphene subtrate. The first peak at $q \approx 0.25\,\text{Å}^{-1}$ is broader and represents the atomic distances in the specimen. One finds that the three particle structure factor has a non-vanishing modulus for q between $0.2\,\text{Å}^{-1}$ and $0.3\,\text{Å}^{-1}$, just as in $S^{(2)}$. For crystalline silica one would expect sharp peaks at 60° and 120° due to its 6-fold symmetry. For amorphous silica, we found the peaks to also be present at those angles. However they are smeared out.

The peaks at $q \approx 0.5\,\text{Å}^{-1}$ are sharper and due to the graphene substrate [Kum+10]. This can be verified by analysing subimages. Figure 5.39 shows the three particle structure factors for the areas inside the boxes in figure 5.38. The yellow box consists only of the graphene substrate hence. The peaks are only at $q \approx 0.5\,\text{Å}^{-1}$ for 60° and 120°. The red box also leads to peaks only at $q \approx 0.5\,\text{Å}^{-1}$ but here there are multiple peaks with 60° distance between them. This stems most likely from this area consisting of a graphene bilayer where the layers are rotated with respect to each other. The blue box shows the same silica peaks that were also present in the whole image but also the graphene peaks even though the substrate is not visible inside the box.

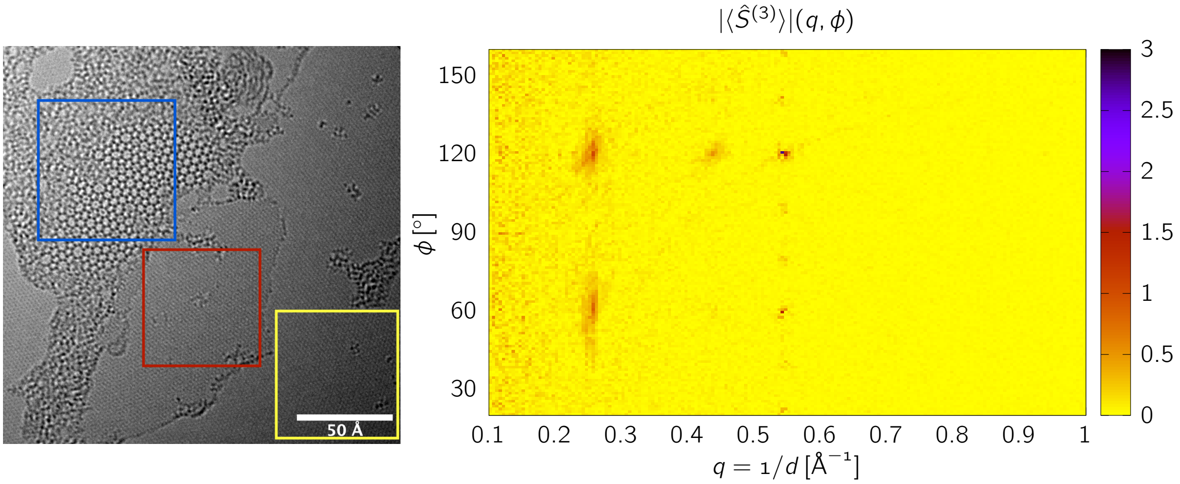

Figure 5.38: Three particle structure factor for amorphous silica. Image data taken from [Hua+12]. The areas in the coloured squares are analysed separately below.

Other images of amorphous silica with their three particle structure factors are shown in appendix B.

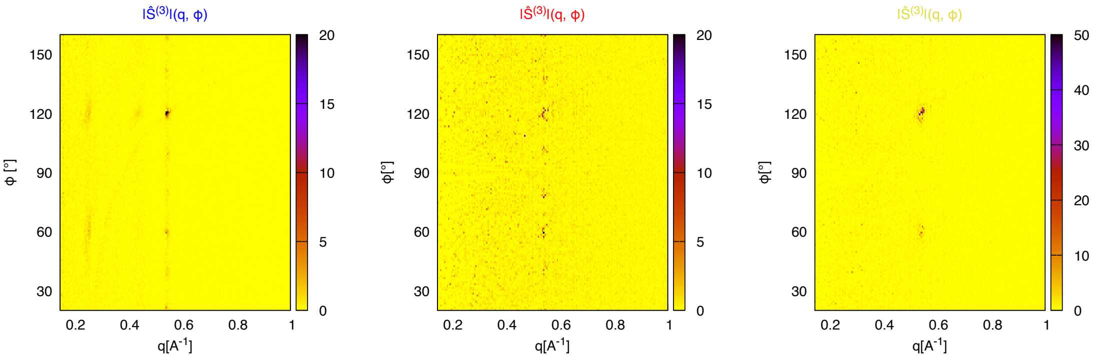

Figure 5.39: The three particle structure factors for the different subimages in figure 5.38. The left image corresponds to the blue box, the middle to the red and the right image to the yellow box.

5.8 Amorphous Carbon

In figure 5.40, the three particle structure factor for a specimen consisting of amorphous carbon with a gold nanocluster placed upon it is shown. The three particle structure shows a strong peak at $q \approx 0.42\,\text{Å}^{-1}$ and $\phi = 120°$ and some weaker peaks at some other angles for the same reciprocal lattice vector. By performing an isolated analysis of an area consisting solely of carbon and an area that consists mostly of the gold nanocluster, one can conclude that for this particular example no meaningful structural information can be obtained from the three particle structure factor. This is shown in figure 5.41.

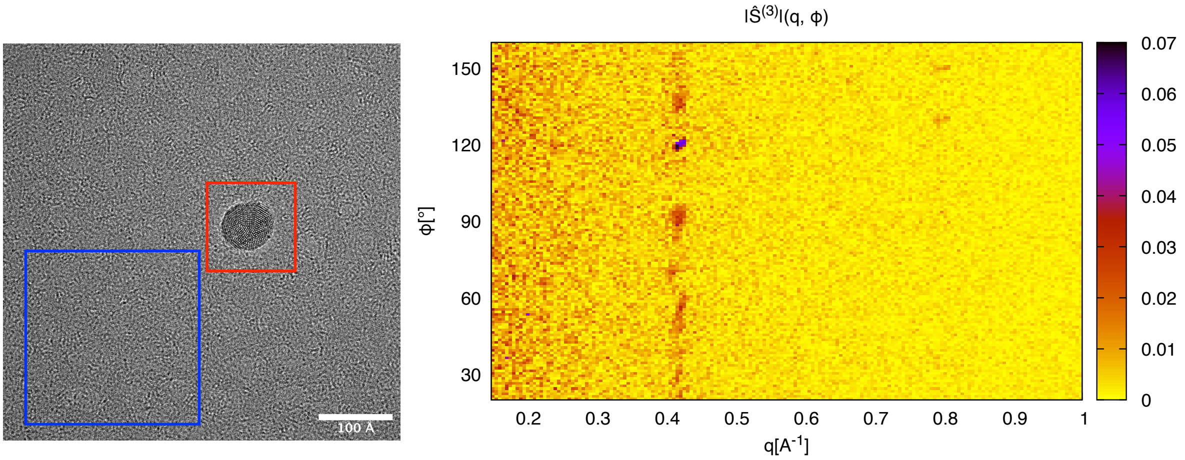

Figure 5.40: An image of amorphous carbon with a gold nanocluster placed on top of it and the resulting three particle structure factor. The areas in the boxes are analyzed separately below.

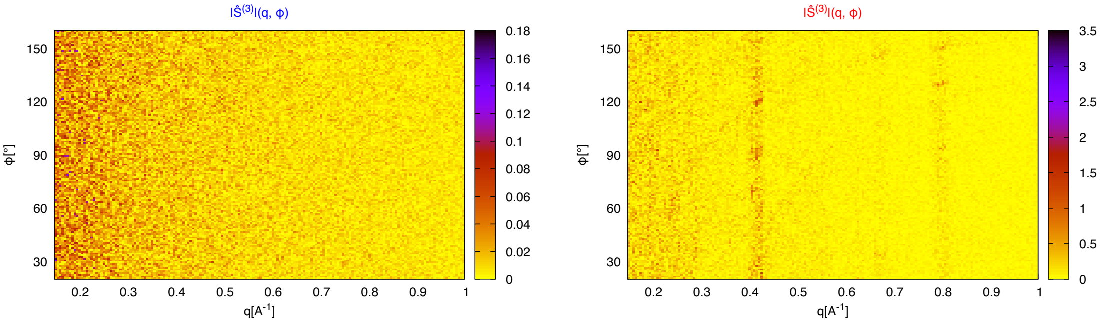

Figure 5.41: The left image shows the three particle structure factor for the blue box in figure 5.40. The right image shows the three particle structure factor for the red box.

By comparison with section 5.5 it follows that the carbon specimen was likely too thick for the three particle structure factor to show any structure.

Chapter 6

Conclusion

For the first time we were able to extract the three particle structure factor from a TEM image of amorphous silica. We also introduced a new normalization technique which improves the signal-to-noise ratio and makes more features visible in the three particle structure factor.

For a specimen of amorphous carbon, no meaningful information about the three particle structure of carbon could be extracted. Only the gold nanocluster that was placed on top of it showed a relevant signal. Simulations with variable thickness show that this method is very sensitive to the thickness of specimen. To obtain meaningful results the specimen thickness has to remain below some thickness threshold.

In MD simulations it was shown that the three particle structure factor obtained from TEM images is able to show differences in structures that are indistinguishable from the pair distribution functions. This demonstrates that the three particle structure factor contains additional informations that cannot be obtained from the pair distributions alone.

From the investigations in this thesis it is apparent that the three particle structure factor can play a role in the classification of amorphous materials.

In recent years amorphous 2d materials have gained increasing interest [Zha+19; YHL20]. Examples are amorphous boron nitrite which can be used for ultrathin electronic devices [Yan+15] and amorphous molybdenum disulfide which can be used for lithium ion batteries [Son+19]. Since for thin specimens the three particle structure factor can be determined most easily, those materials present themselves as ideal candidates for the determination of the three particle structure factor.

Future work could provide more insight into the relation of the shape of three particle structure factor and physical properties of the specimen.

Appendix A

Normalization factor of the averaged three particle structure factor

In the following it will be shown that the normalziation factor in eq. (5.8) following from the conditions $|\vec{q}_1| = |\vec{q}_2| = q$ and $\sphericalangle(\vec{q}_1, \vec{q}_2) = \phi$ is given by $A(q, \phi) = 2\pi q^2$. The vectors $\vec{q}_1$ and $\vec{q}_2$ are represented in the polar-like coordinates defined in figure 5.1 with the parametrizations

$$\vec{q}_1 = q_1 \begin{pmatrix} \cos(\phi + \theta) \\ \sin(\phi + \theta) \end{pmatrix}, \tag{A.1}$$

$$\vec{q}_2 = q_2 \begin{pmatrix} \cos\theta \\ \sin\theta \end{pmatrix}. \tag{A.2}$$

The Jacobian of this transformation is

$$J = \begin{pmatrix} \cos(\phi+\theta) & 0 & -q_1 \sin(\phi+\theta) & -q_1 \sin(\phi+\theta) \\ \sin(\phi+\theta) & 0 & q_1 \cos(\phi+\theta) & q_1 \cos(\phi+\theta) \\ 0 & \cos\theta & 0 & -q_2 \sin\theta \\ 0 & \sin\theta & 0 & q_2 \cos\theta \end{pmatrix} \tag{A.3}$$

and its determinant is given by

$$\det J = \det \begin{pmatrix} \cos(\phi+\theta) & 0 & -q_1 \sin(\phi+\theta) & -q_1 \sin(\phi+\theta) \\ \sin(\phi+\theta) & 0 & q_1 \cos(\phi+\theta) & q_1 \cos(\phi+\theta) \\ 0 & \cos\theta & 0 & -q_2 \sin\theta \\ 0 & \sin\theta & 0 & q_2 \cos\theta \end{pmatrix}, \tag{A.4}$$

$$= -\det \begin{pmatrix} \cos(\phi+\theta) & -q_1 \sin(\phi+\theta) & 0 & -q_1 \sin(\phi+\theta) \\ \sin(\phi+\theta) & q_1 \cos(\phi+\theta) & 0 & q_1 \cos(\phi+\theta) \\ 0 & 0 & \cos\theta & -q_2 \sin\theta \\ 0 & 0 & \sin\theta & q_2 \cos\theta \end{pmatrix}, \tag{A.5}$$

$$= -\det \begin{pmatrix} \cos(\phi+\theta) & -q_1 \sin(\phi+\theta) \\ \sin(\phi+\theta) & q_1 \cos(\phi+\theta) \end{pmatrix} \det \begin{pmatrix} \cos\theta & -q_2 \sin\theta \\ \sin\theta & q_2 \cos\theta \end{pmatrix}, \tag{A.6}$$

$$= -q_1 q_2. \tag{A.7}$$

The area of the hypersurface is then given by

$$A(q,\phi) = \int\limits_{\substack{|\vec{q}_1|=|\vec{q}_2|=q \\ \sphericalangle(\vec{q}_1,\vec{q}_2)=\phi}} \mathrm{d}^2q_1 \mathrm{d}^2q_2 = \int_0^{2\pi} |\det J| \mathrm{d}\theta = \int_0^{2\pi} q^2 \mathrm{d}\theta = 2\pi q^2. \tag{A.8}$$

Appendix B

Amorphous Silica

In the following the three particle structure factor will be obtained for additional images of amorphous silica. In every image amorphous silica is shown on top of a graphene substrate. This is analogous to section 5.7.

Figure B.1 shows the same three peaks from the amorphous silica as figure 5.38. At $q \approx 0.5\,\text{Å}^{-1}$, there are only two peaks at 60° and 120°. This is due to the graphene subtrate consistring of a true monolayer and not a bilayer like in figure B.1. The white area in the bottom right corner stems from the fact that q_3 can exceed the reciprocal space of the image as was discussed in section 5.1.1.

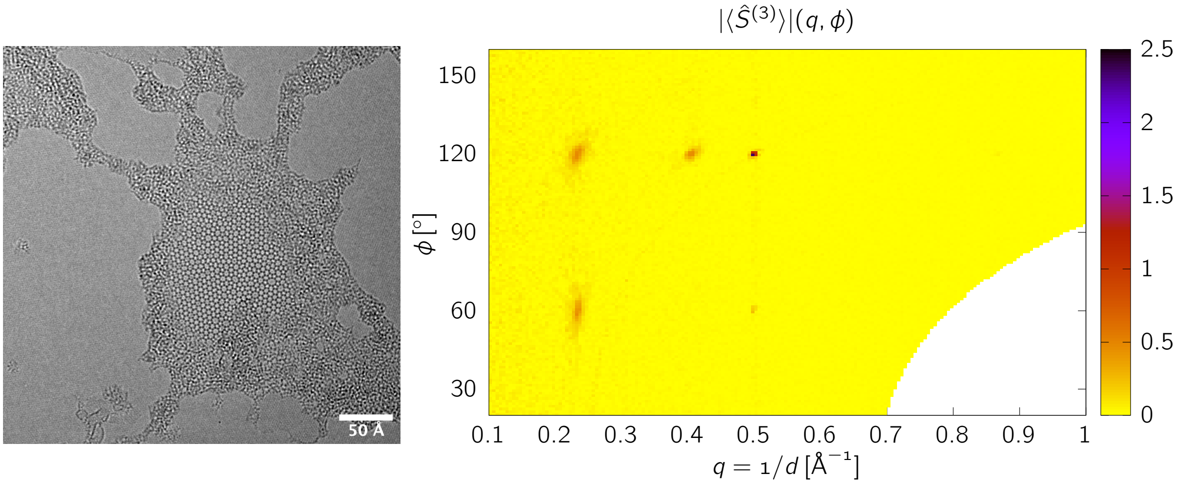

Figure B.1: Three particle structure factor for amorphous silica. Image data taken from [Hua+12].

In figure B.2 only the two graphene peaks are visible. Only when reducing the q range to values up to $0.5\,\text{Å}^{-1}$ the silica peaks become visible since they are almost two magnitudes smaller. This is shown in figure B.3.

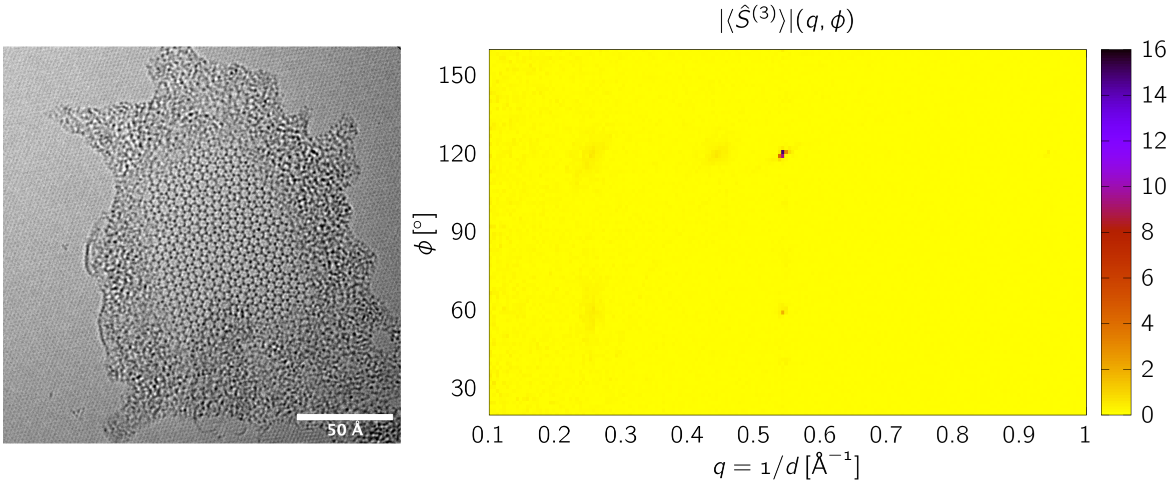

Figure B.2: Three particle structure factor for amorphous silica. Image data taken from [Hua+12].

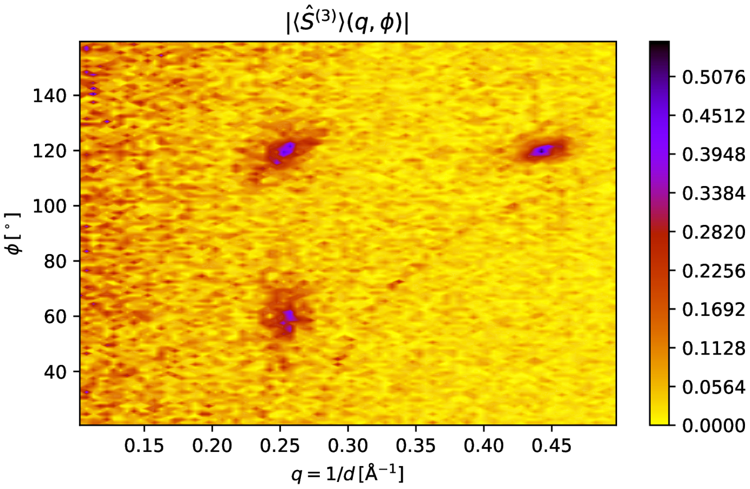

Figure B.3: Same image as figure B.2 but with the q-axis reduced to [0.1 Å^{-1}, 0.5 Å^{-1}].

In figure B.4 again two graphene peaks are visible. Additionally, there are only two silica peaks. Only when reducing the q range to values up to 0.5 Å^{-1} the third silica peak becomes visible. This is shown in figure B.5.

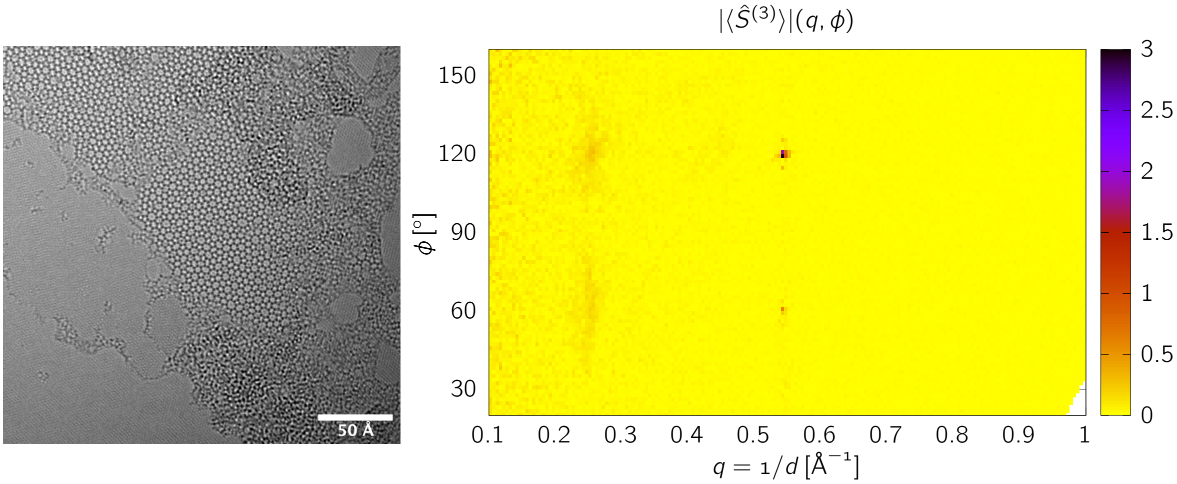

Figure B.4: Three particle structure factor for amorphous silica. Image data taken from [Hua+12].

In figure B.6 two graphene peaks and three silica peaks are visible. Since the silica peaks are almost invisible they are also shown in figure B.7 with a reduced q range.

In figure B.8 there are additional peaks for the graphene substrate which are likely stemming from an additional graphene layer that is rotated to the other layer.

In figure B.9 two graphene peaks and three silica peaks are clearly visible.

When comparing all images, the height as well as the width of the peaks varies with the image. This could stem from the specimens having a differing amount of order or from the specimens consisting of a different amount of silica.

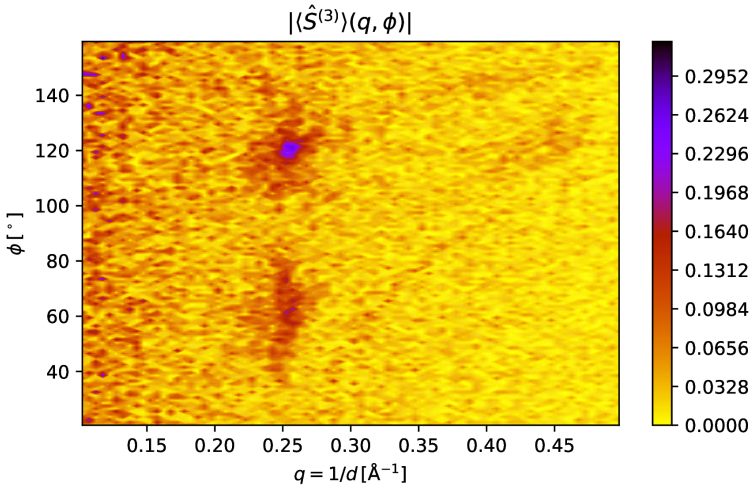

Figure B.5: Same image as figure B.4 but with the q-axis reduced to $[0.1\,\text{Å}^{-1}, 0.5\,\text{Å}^{-1}]$.

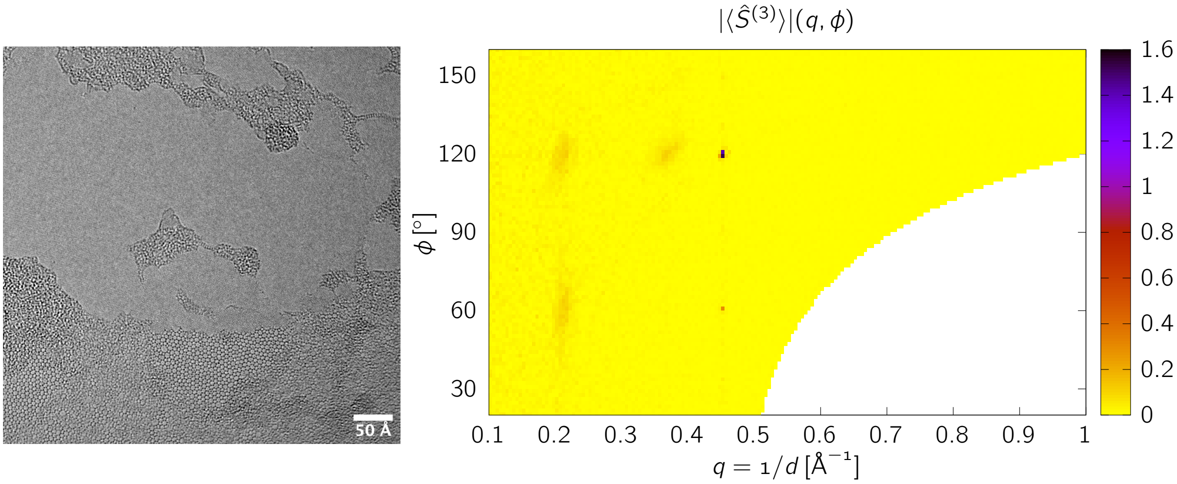

Figure B.6: Three particle structure factor for amorphous silica. Image data taken from [Hua+12].

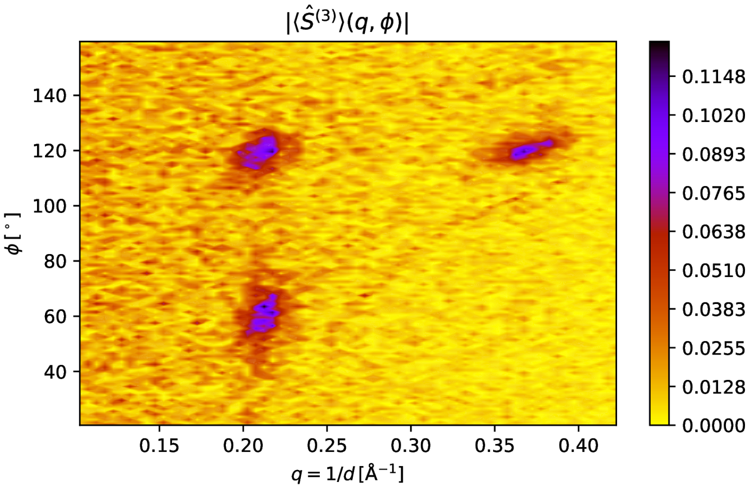

Figure B.7: Same image as figure B.6 but with the q-axis reduced to [0.1 Å^{-1}, 0.5 Å^{-1}].

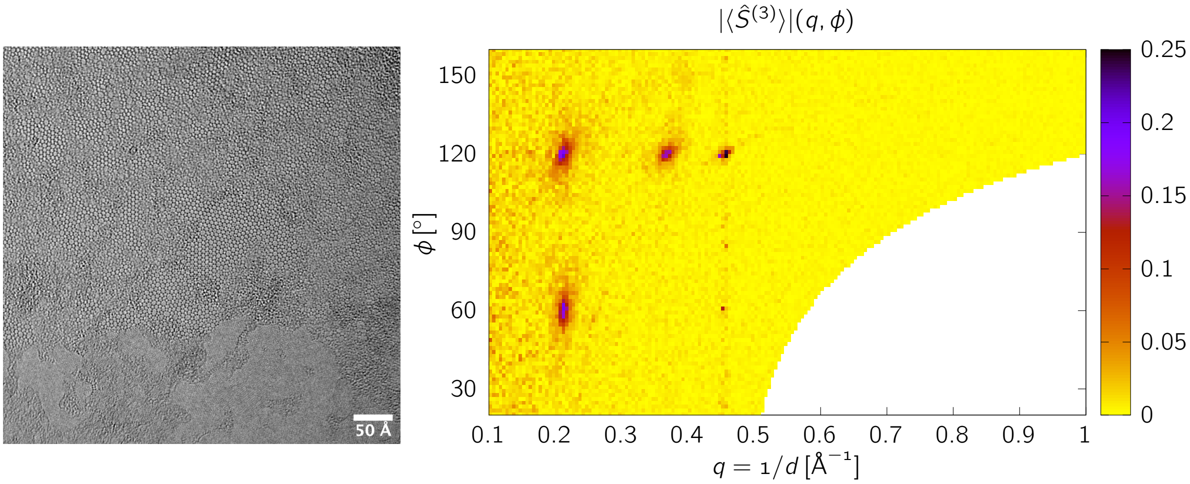

Figure B.8: Three particle structure factor for amorphous silica. Image data taken from [Hua+12].

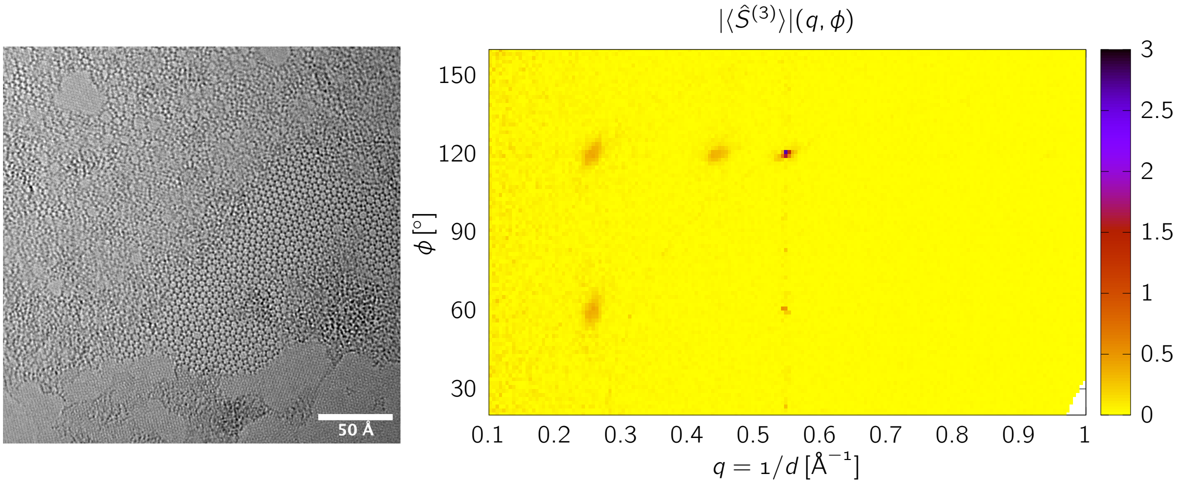

Figure B.9: Three particle structure factor for amorphous silica. Image data taken from [Hua+12].

Appendix C

Implementation

In this appendix, some non-trivial aspects of computing the three particle structure factor will be discussed.

C.1 Discretization

The structure factor is obtained by calculating the Fourier transform of the measured intensities[1],

$$I_{ij} = \mathcal{F}[I]_{ij}, \;\; i \in [0, N), \;\; j \in [0, M), \tag{C.1}$$

where N and M are the number of pixels along the x and y axis. The three particle structure factor is then defined as

$$\hat{S}^{(3)}_{ijkl} = \hat{S}_{ij}\hat{S}_{kl}\hat{S}_{-i-k,-j-l}. \tag{C.2}$$

Since Fourier transforms are periodic, one can evaluate the last factor in (C.2) by taking $S^{(1)}_{-i-k,-j-l} = S^{(1)}_{N-i-k,M-j-l}$.
Since $S^{(3)}_{ijkl}$ consists of $N^2 \cdot M^2$ different values, which is 10^{12} for one megapixel image size and quadratically increasing, it is not advisable to calculate all values beforehand. Instead we have constructed a function object[2] that stores a reference to the structure factor and calculates the values when needed.

---

[1] In this chapter the discretized version of all functions will be used. Hence

$$I_{ij} := I(\Delta q_x \cdot i, \Delta q_y \cdot j),$$

where $\Delta q_i = 1/L_i$ is the inverse dimension of the image.

[2] http://en.cppreference.com/w/cpp/concept/FunctionObject

C.2 Normalization

To obtain the denominator in eq. (5.6), one has to take the average over all values of I that have the same $|\vec{q}|$. Rather than searching for all i, j that correspond to a given $|\vec{q}|$, a different approach was taken.

Two histograms are constructed. The histograms have a fill method taking the q-value and the fill weight. One for summing the values of I for each q bin and one for counting the number of these values. The basic idea is shown in the pseudo code shown in procedure 1. The method q(ix, iy) returns the length of the reciprocal lattice vector corresponding to the pixel at (ix,iy). This approach can also easily be performed in parallel on multiple CPU cores by constructing the histograms for each thread and afterwards collecting all histograms into one[3]. This approach was inspired by [Hak95].

Procedure 1 Calculation of the radially averaged intensity.

```
for all ix do
    for all iy do
        values.fill(q(ix, iy), |I(ix, iy)|)
        counts.fill(q(ix, iy), 1)
    end for
end for
for all bin do
    I_averaged[bin] = values[bin] / counts[bin]
end for
```

C.3 Three Particle Structure Factor

The calculation of the averaged three particle structure factor follows the same ideas as described above. Instead of iterating over all $\vec{q}_1$ and then searching for all $\vec{q}_2$ with the same length, one iterates linearly over the image and fills two histograms. For $\vec{q}_2$, one can reduce the iteration space to the region where $q_{2,x}, q_{2,y} \leq |\vec{q}_1|$ to reduce the number of unused iterations. This can also be made parallel by using reduction.

---

[3] This is also known as a *reduction*.

Procedure 2 Calculation of the averaged three particle structure factor.

```
for all ix in [-N/2, N/2) do
    for all iy in [-M/2, M/2) do
        for all jx in [-jxmax, jxmax) do
            for all jy in [-jymax, jymax) do
                if q(ix, iy) = q(jx,jy) then
                    values.fill(q(ix, iy), phi(ix,iy,jx,jy), $\hat{S}$3(ix,iy,jx,jy))
                    counts.fill(q(ix, iy), phi(ix,iy,jx,jy), 1)
                end if
            end for
        end for
    end for
end for
for all qbin do
    for all phibin do
        $\hat{S}$3_averaged(qbin, phibin) = values(qbin, phibin) / counts(qbin,phibin)
    end for
end for
```

Bibliography

[AM11] Jens Als-Nielsen and Des McMorrow. *Elements of modern X-ray physics*. John Wiley & Sons, 2011.

[BM91] Monika Bargieł and Jacek Mościński. “C-language program for the irregular close packing of hard spheres”. In: *Computer Physics Communications* 64.1 (1991), pp. 183–192.

[Ber83] James G Berryman. “Random close packing of hard spheres and disks”. In: *Physical Review A* 27.2 (1983), p. 1053.

[BB11] Ludovic Berthier and Giulio Biroli. “Theoretical perspective on the glass transition and amorphous materials”. In: *Rev. Mod. Phys.* 83 (2 June 2011), pp. 587–645.

[Bre+02] Donald W Brenner et al. “A second-generation reactive empirical bond order (REBO) potential energy expression for hydrocarbons”. In: *Journal of Physics: Condensed Matter* 14.4 (2002), p. 783.

[CKT06] Lan-Yun Chang, Angus I Kirkland and John M Titchmarsh. “On the importance of fifth-order spherical aberration for a fully corrected electron microscope”. In: *Ultramicroscopy* 106.4-5 (2006), pp. 301–306.

[Cor+09] Thomas H Cormen et al. *Introduction to algorithms*. MIT press, 2009.

[Cus87] N. Cusack. *The Physics of Structurally Disordered Matter: An Introduction*. Hilger, 1987.

[Czy13] G. Czycholl. *Theoretische Festkörperphysik: Von den klassischen Modellen zu modernen Forschungsthemen*. Springer-Lehrbuch. Springer Berlin Heidelberg, 2013.

[Eus84] Roland Eusemann. “Statistik des Rauschens in elektronenmikroskopischen Aufnahmen”. PhD thesis. Technische Hochschule Darmstadt, 1984.

[Fli14] Torsten Fließbach. *Mechanik: Lehrbuch zur Theoretischen Physik I*. Vol. 1. Springer-Verlag, 2014.

[Gup96] Prabhat K Gupta. "Non-crystalline solids: glasses and amorphous solids". In: *Journal of Non-Crystalline Solids* 195.1-2 (1996), pp. 158–164.

[HSS08] Aric A. Hagberg, Daniel A. Schult and Pieter J. Swart. "Exploring Network Structure, Dynamics, and Function using NetworkX". In: *Proceedings of the 7th Python in Science Conference*. Ed. by Gaël Varoquaux, Travis Vaught and Jarrod Millman. Pasadena, CA USA, 2008, pp. 11–15.

[Hak95] Ansgar Haking. "Bestimmung des Drei-Teilchen-Strukturfaktors amorpher Stoffe aus hochaufgelösten elektronenmikroskopischen Aufnahmen". Diploma thesis. WWU Münster, 1995.

[Ham88] Michael Hammel. "Bestimmung der Abbildungsparameter und der Korrelationsfunktion dritter Ordnung amorpher Objekte aus elektronenmikroskopischen Phasenkontrastaufnahmen". Diploma thesis. TH Darmstadt, 1988.

[HGJ79] John Hren, Joseph I. Goldstein and David C. Joy. *Introduction to analytical electron microscopy*. Springer Science & Business Media, 1979.

[Hua+12] Pinshane Y. Huang et al. "Direct Imaging of a Two-Dimensional Silica Glass on Graphene". In: *Nano Letters* 12.2 (2012), pp. 1081–1086.

[Kea66] P. N. Keating. "Effect of Invariance Requirements on the Elastic Strain Energy of Crystals with Application to the Diamond Structure". In: *Phys. Rev.* 145 (2 1966), pp. 637–645.

[Kir10] J. Kirkland. *Advanced Computing in Electron Microscopy*. SpringerLink: Springer e-Books. Springer US, 2010.

[Kit05] Charles Kittel. *Introduction to Solid State Physics. New York, John Wiley&Sons*. 2005.

[Koh] Helmut Kohl. "Hochauflösende Elektronenmikroskopie". Lecture Notes.

[Kum+10] Shishir Kumar et al. "Gas phase controlled deposition of high quality large-area graphene films". In: *Chem. Commun.* 46 (9 2010), pp. 1422–1424.

[Loh88] Adolf W Lohmann. "Pattern recognition based on the triple correlation". In: *Optik* 78.3 (1988), pp. 117–120.

[LF03] JH Los and A Fasolino. "Intrinsic long-range bond-order potential for carbon: Performance in Monte Carlo simulations of graphitization". In: *Physical Review B* 68.2 (2003), p. 024107.

[Mac82] Alan L Mackay. "Crystallography and the Penrose pattern". In: *Physica A: Statistical Mechanics and its Applications* 114.1-3 (1982), pp. 609–613.

[NBN99] Mark EJ Newman, Gerard T Barkema and MEJ Newman. *Monte Carlo methods in statistical physics*. Vol. 13. Clarendon Press Oxford, 1999.

[NK92] G.T. Nolan and P.E. Kavanagh. "Computer simulation of random packing of hard spheres". In: *Powder Technology* 72.2 (1992), pp. 149–155.

[Pen74] Roger Penrose. "The role of aesthetics in pure and applied mathematical research". In: *Bull. Inst. Math. Appl.* 10 (1974), pp. 266–271.

[Pli93] Steve Plimpton. *Fast parallel algorithms for short-range molecular dynamics*. Tech. rep. Sandia National Labs., Albuquerque, NM (United States), 1993.

[Pre11] Jeff Preshing. *Penrose Tiling Explained*. 31 Aug. 2011. url: https://preshing.com/20110831/penrose-tiling-explained/ (visited on 17/07/2020).

[Son+19] Ming Song et al. "Atomic-layer-deposited amorphous MoS2 for durable and flexible Li–O2 batteries". In: *Small Methods* (2019), p. 1900274.

[Sta15] Zbigniew H Stachurski. *Fundamentals of amorphous solids: structure and properties*. John Wiley & Sons, 2015.

[Ter94] J Tersoff. "Chemical order in amorphous silicon carbide". In: *Physical Review B* 49.23 (1994), p. 16349.

[TSM16] Carla de Tomas, Irene Suarez-Martinez and Nigel A Marks. "Graphitization of amorphous carbons: A comparative study of interatomic potentials". In: *Carbon* 109 (2016), pp. 681–693.

[TTD00] Salvatore Torquato, Thomas M Truskett and Pablo G Debenedetti. "Is random close packing of spheres well defined?" In: *Physical review letters* 84.10 (2000), p. 2064.

[Var13] Arun K Varshneya. *Fundamentals of inorganic glasses*. Elsevier, 2013.

[Vin+01] RLC Vink et al. "Device-size atomistic models of amorphous silicon". In: *Physical Review B* 64.24 (2001), p. 245214.

[WWW90] J Wejchert, D Weaire and F Wooten. "Topological disorder in sillium: A statistical approach". In: *Journal of non-crystalline solids* 122.3 (1990), pp. 241–261.

[WC09] David B Williams and C Barry Carter. *Transmission electron microscopy: a textbook for materials science*. Springer, 2009.

[WW87] F Wooten and D Weaire. "Modeling tetrahedrally bonded random networks by computer". In: *Solid State Physics* 40 (1987), pp. 1–42.

[WWW85] F Wooten, K Winer and D Weaire. "Computer generation of structural models of amorphous Si and Ge". In: *Physical review letters* 54.13 (1985), p. 1392.

[WW95] F. Wooten and D. Weaire. "Chapter 15 Structural models of tetrahedrally bonded amorphous materials". In: *Adaption of simulated annealing to chemical optimization problems*. Ed. by John H. Kalivas. Vol. 15. Data Handling in Science and Technology. Elsevier, 1995, pp. 329–349.

[YHL20] Zhibin Yang, Jianhua Hao and Shu Ping Lau. "Synthesis, properties, and applications of 2D amorphous inorganic materials". In: *Journal of Applied Physics* 127.22 (2020), p. 220901.

[Yan+15] Zhibin Yang et al. "Field-effect transistors based on amorphous black phosphorus ultrathin films by pulsed laser deposition". In: *Advanced Materials* 27.25 (2015), pp. 3748–3754.

[Zac32] W. H. Zachariasen. "The Atomic Arrangement in Glass". In: *Journal of the American Chemical Society* 54.10 (1932), pp. 3841–3851.

[Zha+19] Hewei Zhao et al. "Two-dimensional amorphous nanomaterials: synthesis and applications". In: *2D Materials* 6.3 (2019), p. 032002.

[Zim79] J.M. Ziman. *Models of Disorder: The Theoretical Physics of Homogeneously Disordered Systems*. Cambridge University Press, 1979.

Danksagung

Viele Personen haben zum Gelingen dieser Arbeit beigetragen. Ich möchte mich dafür bedanken bei:

- Herrn Prof. Dr. Helmut Kohl für das Thema und dafür, dass er für Fragen jederzeit bereitstand
- Herrn Dr. Stephan Majert für die fachlichen Diskussionen und die gemeinsame Zeit im Büro
- Herrn Markus Silder, dafür dass er sich immer um alles gekümmert hat
- Herrn Julian Sickel, Herrn Marcel Asbach und Allen, die in den letzten fünf Jahren in der Arbeitsgruppe waren für die fachlichen Diskussionen und die Ablenkungen zwischendurch
- Frau Prof. Dr. Ute Kaiser für das Bereitstellen der Silica-Messdaten
- Herrn Dr. Martin Peterlechner für die Messungen am Themis
- Meinen Freunden Johannes, Patrick, Ricarda, Tobi, Matze, Basti und Bernhard für die gemeinsame Zeit schon seit beginn des Studiums
- meiner Freundin Elisa, die mich in der Zeit immer unterstützt hat
- meinem Bruder, meinen Großeltern und meinen Eltern, ohne die ich nie dahin gekommen wäre, diese Arbeit zu schreiben